Direct Simulation Monte Carlo Method for Cold Atom Dynamics: Boltzmann Equation in the Quantum Collision Regime

Andrew Christopher James Wade
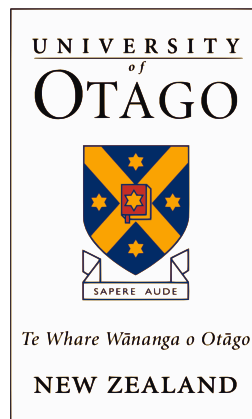
a thesis submitted for the degree of

Master of Science

at the University of Otago, Dunedin,

New Zealand.

July 27, 2012

Abstract

In this thesis we develop a direct simulation Monte Carlo (DSMC) method for simulating highly nonequilibrium dynamics of nondegenerate ultra cold gases. We show that our method can simulate the high-energy collision of two thermal clouds in the regime observed in experiments [Thomas *et al.* Phys. Rev. Lett. **93**, 173201 (2004)], which requires the inclusion of beyond s-wave scattering. We also consider the long-time dynamics of this system, demonstrating that this would be a practical experimental scenario for testing the Boltzmann equation and studying rethermalization. A quantum DSMC algorithm is also discussed.

Acknowledgements

There are many whom I wish to thank for the opportunities they have given me, be it directly, or for the unconscious support of a friend. Here are a few...

First of all my supervisor and friend Assoc. Prof. Blair Blakie for the freedom, accessibility, insight and morale boosts in those painful Masters moments. For the privileges of conferences, summer courses, group meetings, and finally, for the general academic advice and continuing support.

My collaborators and substitute supervisors when Blair had had enough and left the country periodically: Danny Baillie, Dr. Ashton Bradley, Dr. Niels Kjaergaard, and Dr. Eite Tiesinga. Danny for being my coding guru and his intense critiquing, such as noting "should be good/sweet as" is not the best scientific terminology for an article. Ashton for entertaining many of my "fruitful" discussions. Niels for his physics and fishing advice.

My friends for the good times, and my colleagues whom share the same pains.

My family, who are always with me.

Finally, my beloved Line.

Abbreviations and Notation

Here, we give tables of the notation and the abbreviations used in this thesis. We do not include commonly used notation, e.g., $\mathbf{r}$ as the position vector or T as temperature, and notation that is not used in more than one section. The reference gives the page in which they are first introduced.

Table 1: *Abbreviations.*

Abbreviation	Description	Reference
BE	Boltzmann equation.	1
ZNG	Zaremba-Nikuni-Griffin.	1
DSMC	Direct simulation Monte Carlo.	2
LATS	Locally adaptive time step.	3
LAC	Locally adaptive cell.	3
Kn	Knudsen number.	13
NNC	Nearest neighbor collision.	15
TASC	Transient adaptive subcell.	21
LSD	Locally sampled density.	79
FFT	Fast Fourier Transform.	85

Table 2: *Notation.*

Notation	Description	Reference
T_{coll}	Collision energy.	2
v_{r}	Magnitude of the relative velocity.	2
$f \equiv f(\mathbf{p}, \mathbf{r}, t)$	Semiclassically phase-space distribution function.	7
$n(\mathbf{r}, t)$	Position space density.	7
$U(\mathbf{r}, t)$	Potential.	7
a_{sc}	s-wave scattering length.	8
$\frac{d\sigma}{d\Omega}$	Differential cross section.	8
$\mathbf{P}$	Total momentum.	8
$\mathbf{p}_{\mathrm{r}}$	Relative momentum.	8
$f_{\mathrm{sc}}(\theta)$	Scattering function.	10
δ_l	Phase shift associated with partial wave l.	10
θ	Centre-of-mass scattering angle.	10
$\sigma(v_{\mathrm{r}})$	Total collision energy dependent cross-section.	11
α	Ratio of physical atoms to test particles.	14
$\mathcal{N}_{\mathrm{P}}$	Number of physical atoms.	14
$\mathcal{N}_{\mathrm{T}}$	Number of test particles.	14
Δt	Simulation time step.	14
N_c	Number of test particles within cell c.	18

Table 3: *Notation: continued.*

Notation	Description	Reference
N_{th}	Test particle threshold for the LAC subdivision.	18
ΔV_c	Volume of cell c.	20
P_{ij}	Collision probability for a pair of test particles i and j.	20
M_c	Number of tested collisions in cell c.	20
Λ	Collision rescaling factor.	21
$\tilde{P}_{ij}$	Rescaled collision probability.	21
$\tilde{M}_c$	Rescaled number of tested collisions.	21
n_c	Average density of cell c.	21
τ_c^{coll}	Mean-collision time of cell c.	27
τ_c^{max}	Max collision time of cell c.	27
τ_c^{tr}	Mean transit time of cell c.	27
Δx	Master cell width.	27
Δx_c	x (y or z) width of cell c.	27
ω_x	Trap frequency in the x (y or z) direction.	33
$f_{\text{eq}}\left(\mathbf{p}, \mathbf{r}\right)$	Maxwell-Boltzmann equilibrium distribution function.	39
$\mathcal{N}_{\text{P}}^i$	Number of physical atoms in cloud i.	39
ξ_{xy}^i and ξ_z^i	Fitted standard deviations of cloud i.	39
R	Total collision rate.	41
p_0	Momentum offset.	41
σ_0	Constant (velocity independent) total cross section.	41
γ	Bin parameter.	42
$\mathcal{N}_{\text{sc}}$	Number of scattered atoms from a cloud.	45
$P\left(\theta\right)$	Angular scattering probability.	57
$P_{\text{expt}}\left(\theta_i\right)$	Angular scattering probability for the experiment.	60
$P_{\text{sim}}\left(\theta_i\right)$	Angular scattering probability for the DSMC simulation.	60
σ_{eff}	Effective total cross section.	79

Contents

Contents

Chapter 1

Introduction

Within ultra-cold-atom research, there are a range of problems requiring the understanding of the dynamics of a normal gas. For example, studies of collective modes of Bose [1] and Fermi [2] gases (also see Refs. [3, 4]), spin waves [5, 6], hydrodynamic expansion of a Bose gas near the critical temperature [7], and more recently, the dynamics and thermalization of a nearly degenerate gas of polar molecules [8]. These are all regimes in which the Boltzmann equation (BE) is thought to provide an accurate description. In many of these cases, the system is only weakly disturbed from equilibrium, and some approximate solution can be provided using a relaxation approximation for the collision integral and some form of linearization [9], scaling [10, 11], or variational [12] ansatz. For more strongly dynamical situations, these approaches are insufficient, however, the direct solution of the BE for the six-dimensional distribution function is generally considered intractable and is normally tackled using some form of stochastic particle simulation. Some applications of such calculations include the work of Wu and co-workers [13, 14, 15] on evaporative cooling and expansion dynamics, Jackson and co-workers [16, 17, 18, 19, 20] on bosonic collective-mode dynamics (coupled to a superfluid by the Zaremba-Nikuni-Griffin (ZNG) formalism [21]), the work of Urban and Schuck [22], Urban [23, 24], and Lepers *et al.* [25] in formulating fermion dynamics (see also Refs. [26, 27, 28, 29]), and Barletta *et al.* [30] and Barletta [31] in describing sympathetically cooled molecular gases.

Here, we develop an algorithm for simulating the BE that is significantly more accurate and efficient than these previous methods and is applicable to more extreme regimes of dynamics. Indeed, our main motivation was to develop a theory capable of describing the ultra-cold-atom collider developed by the Otago group [32, 33, 34]. In those experiments (nonquantum degenerate), clouds of bosonic atoms at a temperature of ~ 200 nK were accelerated and were collided at an energy of ~ 200 μK (see Fig. 1.1). Several features of
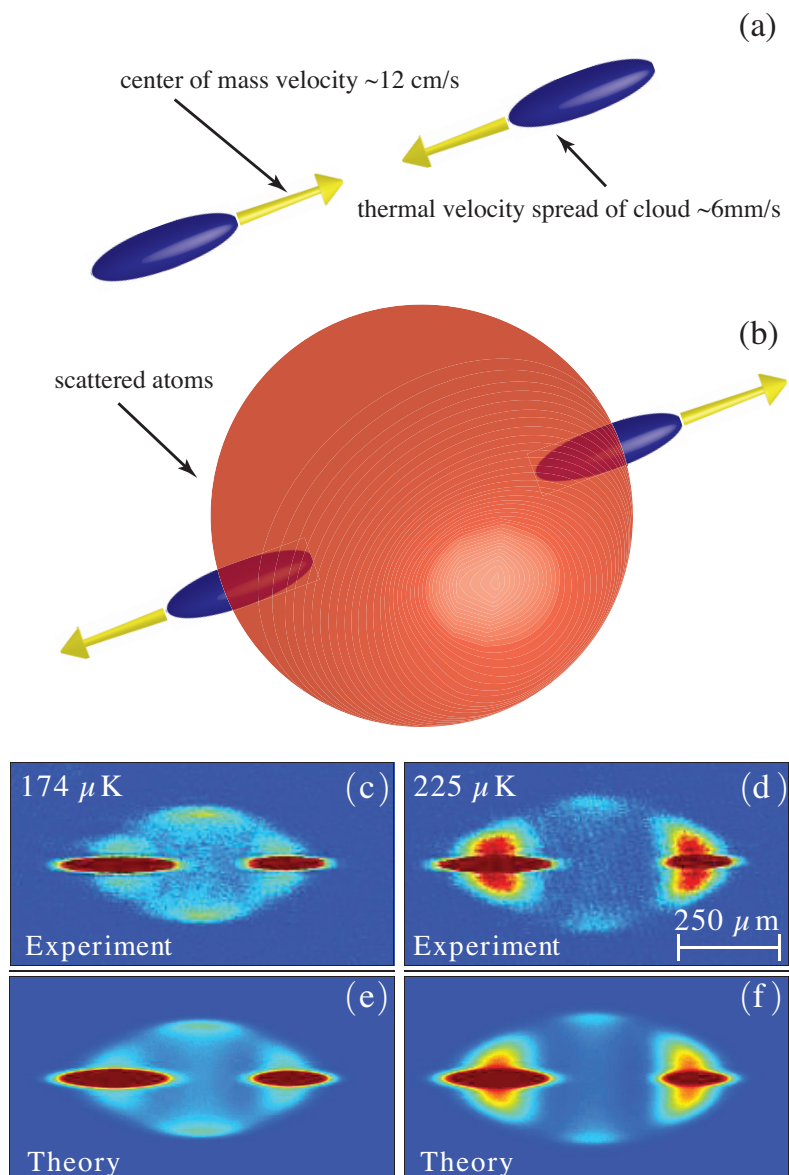
Figure 1.1: Ultra-cold-atom collider: (a) schematic of the precollision arrangement of two clouds at ~ 200 nK approaching at a collision energy of $\sim 200\,\mu$K; (b) schematic of a postcollision system. (c) and (d) experimental images, presented by Thomas *et al.* [32], of post scattering density for two collision energies spanning the *d*-wave shape resonance. (e) and (f) show our theoretical calculations matching the experimental results using the direct simulation Monte Carlo (DSMC) method developed in this thesis. Following the terminology established in experiments, we characterize the collider kinetic energy in temperature units by the parameter $T_{\text{coll}} \equiv \mu v_{\text{r}}^2 / 2k_{\text{B}}$, where $\mu = m/2$ is the reduced mass, and v_r is the magnitude of the relative velocity.

these experiments make the numerical simulation difficult:

(i) The system is far from equilibrium and accesses a large volume of phase space. A good representation of each cloud before the collision requires nano-Kelvin energy resolution, however, during the collision, atoms are scattered over states on the collision sphere with an energy spread on the order of a milli-Kelvin.

(ii) The collision energies are sufficiently large that an appreciable amount of higher-order (i.e. beyond s-wave) scattering occurs. In particular, in experiments p-wave scattering [34] and a d-wave [32] shape resonance have been explored (see Fig. 1.2).

The algorithm we develop is suitable for this regime, and, as shown in Figs. 1.1(c)-1.1(f), it can provide a quantitative model for the experimental data in Ref. [32]. Feature (i) discussed above presents a great challenge, and using the traditional Boltzmann techniques employed to date in ultra-cold-atom research, this would require super computer resources. We show how to make use of an adaptive algorithm (that adapts both the spatial grid and the times steps to place resources where needed) to accurately simulate an ultra-cold-atom collider on commodity personal computer hardware.

We note that, in addition to collider experiments, a capable BE solver would allow theoretical studies in a range of areas of emerging interest, such as the turbulence and flow instabilities in the normal phase of a quantum gas. Here, we will focus mostly on the classical regime where the phase-space density is small compared to unity such that the many-body effects of Bose-stimulated or Pauli-blocked scatterings are negligible. However, the systems we consider will be in the *quantum collision regime*, whereby the thermal de Broglie wavelength is larger than the typical range of the interatomic potential. Notably, in this regime, the scattering is wave like, and quantum statistics on the two-body level gives rise to profound effects in the individual collision processes, even though many-body quantum statistics is unimportant.

All of the Boltzmann simulations appearing in the ultra-cold-atom literature have been based on DSMC-like methods, typically employing the algorithm described in Bird's 1994 monograph [35]. However, a challenging feature of ultracold gases is that the local properties (e.g., the density) can vary by orders of magnitude across the system, and no single global choice of parameters for the DSMC can provide a good description across this entire range. For this reason, we introduce the use of two locally adaptive schemes to allow the system to refine the description and to allocate more computational resources to regions of high density. These schemes are as follows: locally adaptive time steps (LATSs) and locally adaptive cells (LACs). We discuss these, as well as the overall DSMC method, in Chapter 3.
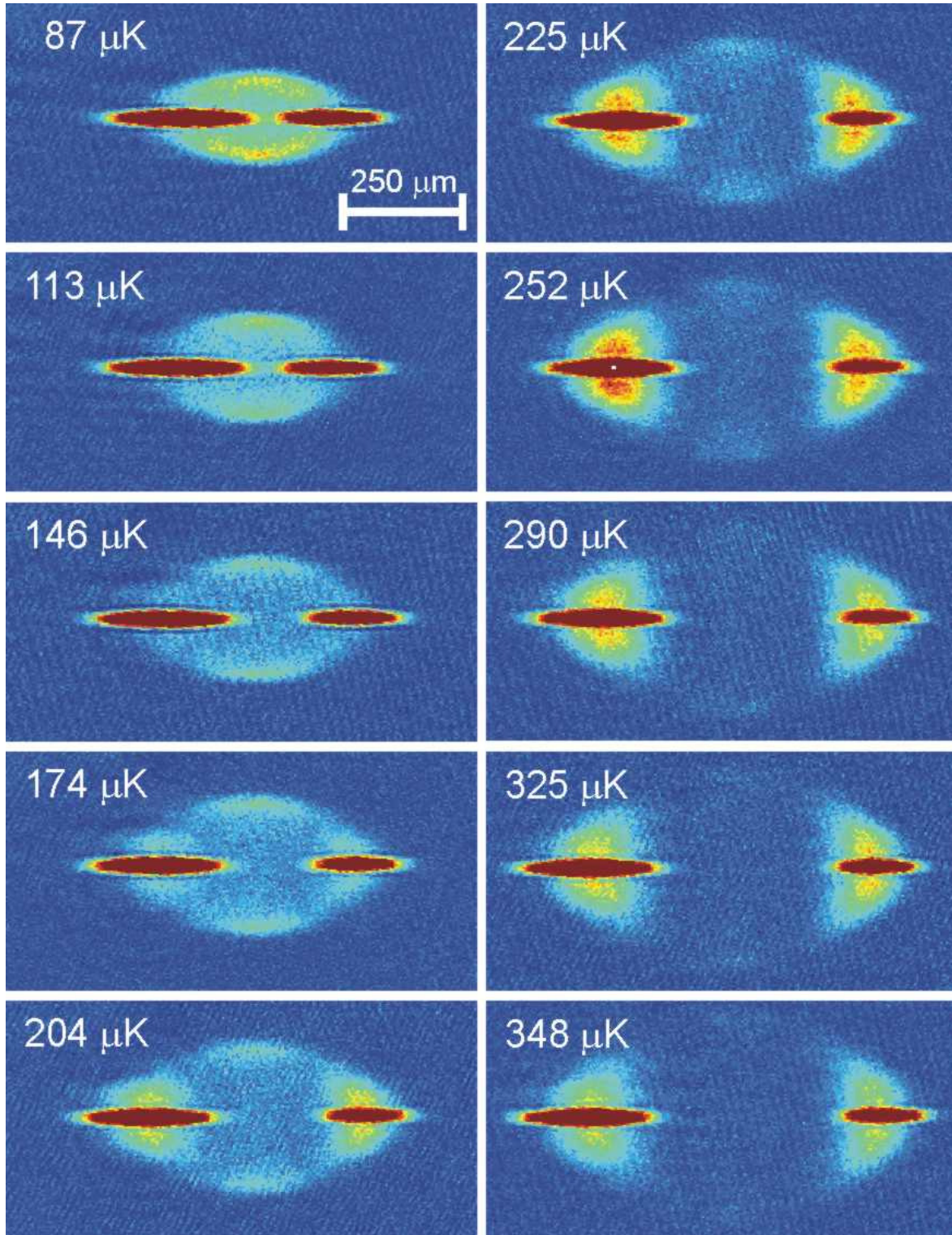
Figure 1.2: The experimental results of Thomas *et al.* Ref. [32], which shows as T_{coll} increases, the collisions are initially *s*-wave dominated ($T_{\text{coll}} = 87\,\mu\text{K}$), then, interference between the *s*- and *d*-waves occurs, as a *d*-wave shape resonance is reached.

In Chapter 4, we establish how to solve the problem of the ultra-cold-atom collider, and we validate our algorithm using a variety of tests to demonstrate its applicability and performance. Then, we apply it to the regime of the ultra-cold-atom collider experiments [32]. Following this, in Chapter 5, we perform a quantitative study of the ultra-cold-atom collider. Finally, in Chapter 6, we discuss extending the DSMC algorithm to include quantum many-body statistics.

The work of Chapters 3 and 4 has been published in Physical Review A [36], and, for the work of Chapter 5, there is a paper in preparation.

Chapter 2

Background Theory

Here, we describe the Boltzmann equation and the quantum Boltzmann equation, as well as, the partial-wave description of the differential cross section. Useful references for the BE are the books by Huang [37] and Kardar [38], and for the quantum BE and partial-wave description, the book by Pethick and Smith [39].

2.1 The Classical and Quantum Boltzmann Equations

The quantum BE appears in many fields, and has been labelled with many names, for example, the Boltzmann-Uehling-Uhlenbeck, Vlasov-Uehling-Uhlenbeck, Boltzmann-Nordheim, and Landau-Vlasov equation. Here, we choose to refer to this equation, as the quantum Boltzmann equation.

The system of interest is a dilute gas of identical atoms, and is described semiclassically by the phase-space distribution function $f \equiv f(\mathbf{p}, \mathbf{r}, t)$, where $f(\mathbf{p}, \mathbf{r}, t) \, d^3 p \, d^3 x$ is the mean number of atoms in the phase-space volume $\mathbf{p} \rightarrow \mathbf{p} + (dp_x, dp_z, dp_z)$ and $\mathbf{r} \rightarrow \mathbf{r} + (dx, dy, dz)$. The quantum BE gives the evolution of the distribution function [39]

$$\left[\frac{\partial}{\partial t} + \frac{\mathbf{p}}{m} \cdot \nabla_{\mathbf{r}} - \nabla_{\mathbf{r}} U(\mathbf{r}, t) \cdot \nabla_{\mathbf{p}} \right] f = I[f], \tag{2.1}$$

where the position-space density of the atoms $n(\mathbf{r}, t)$ is given by

$$n(\mathbf{r}, t) = \int \frac{d^3 p}{h^3} f(\mathbf{p}, \mathbf{r}, t). \tag{2.2}$$

The left-hand side of Eq. (2.1) describes the evolution of atoms under the potential $U(\mathbf{r}, t)$. In general, $U(\mathbf{r}, t)$ may contain a mean-field term, e.g.,

$$U_{\mathrm{MF}}(\mathbf{r}, t) = 2gn(\mathbf{r}, t), \tag{2.3}$$

where $g = 4\pi\hbar^2 a_{\mathrm{sc}}/m$, with a_{sc} as the *s*-wave scattering length, which discussed further in the next section. However, for our analysis presented here, we only consider the case where $U(\mathbf{r}, t)$ is an external trapping potential.

The collision integral $I[f]$, accounts for the collisions between atoms, and is given by

$$I[f] = \frac{1}{m} \int \frac{d^3 p_1}{h^3} \int d\Omega \frac{d\sigma}{d\Omega} |\mathbf{p}_1 - \mathbf{p}| [\underbrace{f' f_1' (1 \pm f)(1 \pm f_1)}_{\text{Incoming}} - \underbrace{f f_1 (1 \pm f')(1 \pm f_1')}_{\text{Outgoing}}],$$

(2.4)

where $\frac{d\sigma}{d\Omega}$ is the differential cross section, and $f_1 \equiv f(\mathbf{p}_1, \mathbf{r}, t)$, $f' \equiv f(\mathbf{p}', \mathbf{r}, t)$, etc.

When considering the flow of atoms through phase space due to collisions, $I[f]$ has a simple interpretation. The outgoing term in Eq. (2.4) containing $f f_1$ describes binary collisions of point-like atoms, where the atoms are initially at the phase-space points $(\mathbf{p}, \mathbf{r})$ and $(\mathbf{p}_1, \mathbf{r})$, and have final states $(\mathbf{p}', \mathbf{r})$ and $(\mathbf{p}_1', \mathbf{r})$. During such a collision, total and relative momenta

$$\mathbf{P} = \frac{\mathbf{p} + \mathbf{p}_1}{2}, \qquad \mathbf{P}' = \frac{\mathbf{p}' + \mathbf{p}_1'}{2},$$

(2.5a)

$$\mathbf{p}_{\mathrm{r}} = \mathbf{p}_1 - \mathbf{p}, \qquad \mathbf{p}_{\mathrm{r}}' = \mathbf{p}_1' - \mathbf{p}',$$

(2.5b)

respectively, are constrained by

$$\mathbf{P} = \mathbf{P}',$$

(2.6a)

$$|\mathbf{p}_{\mathrm{r}}| = |\mathbf{p}_{\mathrm{r}}'|,$$

(2.6b)

to ensure conservation of momentum and energy (a geometrical representation of the collision can be seen in Fig. 2.1). The atomic interactions we wish to describe are contained in the differential cross section, which describes the angular distribution for scattering events between pairs of atoms as a function of their relative speed, and Ω is the solid angle formed by the incoming and outgoing relative momenta.

The incoming term of Eq. (2.4) describes the opposite process where atoms scatter from $(\mathbf{p}', \mathbf{r})$ and $(\mathbf{p}_1', \mathbf{r})$ to $(\mathbf{p}, \mathbf{r})$ and $(\mathbf{p}_1, \mathbf{r})$. The quantum statistics of the atoms is included by the $(1 \pm f')(1 \pm f_1')$ terms, which account for Bose-stimulated scattering $(+)$ or Pauli blocking $(-)$.

Neglecting Bose-stimulated scattering, or Pauli blocking, gives the BE, which is appropriate for nondegenerate regimes where $f \ll 1$. In detail, the BE reads

$$\left[\frac{\partial}{\partial t} + \frac{\mathbf{p}}{m} \cdot \nabla_{\mathbf{r}} - \nabla_{\mathbf{r}} U(\mathbf{r}, t) \cdot \nabla_{\mathbf{p}} \right] f = \frac{1}{m} \int \frac{d^3 p_1}{h^3} \int d\Omega \frac{d\sigma}{d\Omega} |\mathbf{p}_1 - \mathbf{p}| [f' f_1' - f f_1], \quad (2.7)$$

and is the main focus of this thesis, except for the extensions of the DSMC algorithm discussed in Chapter 6 to describe the quantum BE [Eqs. (2.1) and Eq. (2.4)].
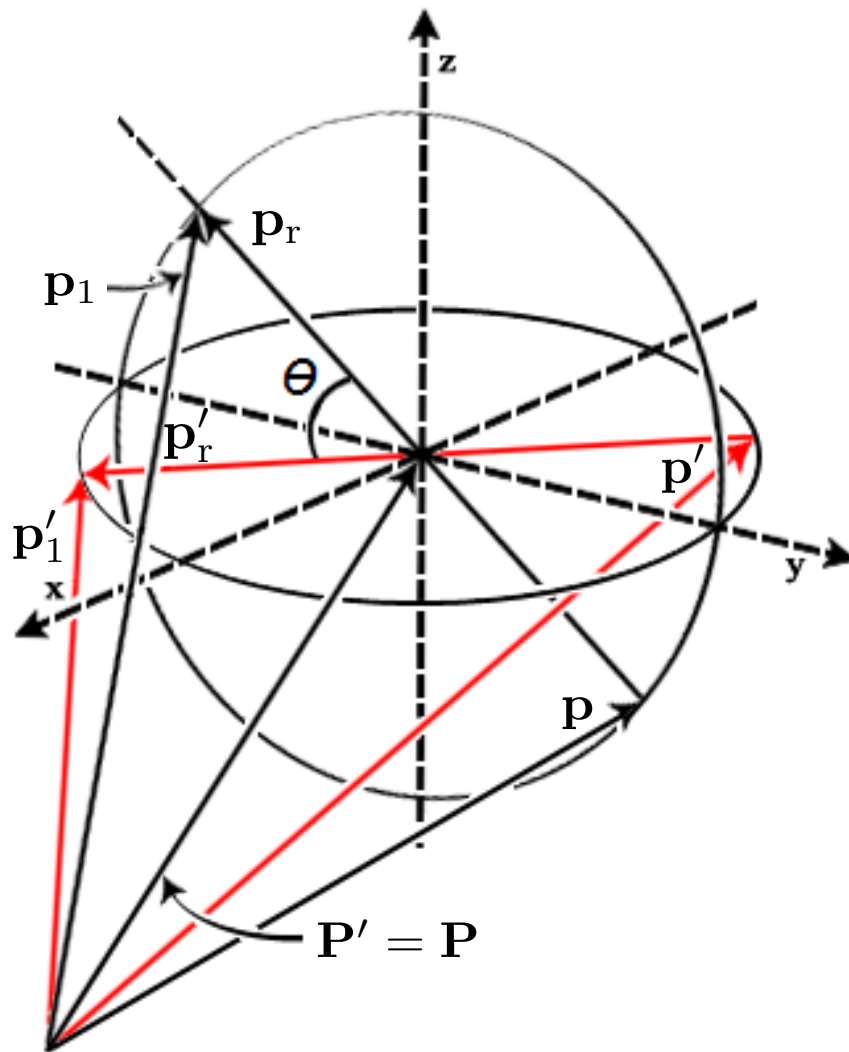
Figure 2.1: Geometrical representation of a binary collision of point-like particles. During the collision, the total energy and the total momentum of the pair are conserved. Only the momenta are changed by keeping the total momentum constant, and rotating the relative momentum vector about its center [37]. The initial states of the two particles are shown in black, while the final states are shown in red, while the axes give the momenta in x, y, and z directions.

2.2 Partial-Wave Treatment of Collisions

While our main interest here is in ultracold gases with sufficiently low phase-space density to neglect many-body quantum statistics, the two-body collisions themselves are in the quantum collision regime and are conveniently characterized in terms of a partial-wave expansion [39]. The differential cross section for identical bosons $(+)$ or fermions $(-)$ in the same internal state is

$$\frac{d\sigma}{d\Omega} = |f_{\text{sc}}(\theta) \pm f_{\text{sc}}(\pi - \theta)|^2, \tag{2.8}$$

where

$$f_{\text{sc}}(\theta) = \frac{\hbar}{imv_{\text{r}}} \sum_{l=0}^{\infty} (2l + 1) \left(e^{2i\delta_l} - 1 \right) P_l(\cos\theta), \tag{2.9}$$

is the scattering function, δ_l is the phase shift associated with partial wave l, $P_l(\cos\theta)$ is the lth Legendre polynomial and θ is the centre-of-mass scattering angle. In general, the phase shifts have a collision energy dependence (v_{r}), which is a nontrivial task to calculate. For bosons (fermions), the total wave function is required to be symmetric (antisymmetric), and hence, only the even (odd) l terms in Eq. (2.9) contribute to the differential cross section.

In the low collision energy limit, only *s*-wave scattering will occur. Taking the limit $v_{\text{r}} \to 0$, Eq. (2.9) approaches a constant,

$$\lim_{v_{\text{r}} \to 0} f_{\text{sc}}(\theta) = \lim_{v_{\text{r}} \to 0} \frac{2\hbar}{mv_{\text{r}}} \frac{1}{\cot\delta_0 - i} = -a_{\text{sc}}, \tag{2.10}$$

which is called the *s-wave scattering length*. A curious observation, is that, identical fermions require their wave function to be antisymmetric, thus, their lowest energy interactions are the *p*-wave interactions $l = 1$. As a system of identical fermions cools, at some point the *p*-wave interactions freeze out, rendering the system noninteracting. As the evaporative cooling technique requires interactions for the system to rethermalize, reaching Fermi degeneracy for trapped fermions was achieved by sympathetic cooling. This is where a Fermi-Fermi mixture [40] or Bose-Fermi mixture [41] is used, since two species are distinguishable, and do have *s*-wave interactions between each other, hence, giving the fermions a pathway to rethermalize.

The low collision energy limit gives the angle-independent differential cross section for identical bosons

$$\frac{d\sigma}{d\Omega} = 8\pi a_{\text{sc}}^2, \tag{2.11}$$

and this limit is where the majority of cold atom theory is applied. Most famously seen in the Gross-Pitaevskii equation [42], which uses the Fermi pseudo potential,

$$U(\mathbf{r}' - \mathbf{r}) = \frac{4\pi\hbar^2 a_{\text{sc}}}{m} \delta(\mathbf{r}' - \mathbf{r}) = g\delta(\mathbf{r}' - \mathbf{r}), \tag{2.12}$$

for the atom-atom interactions, where $\delta \left(\mathbf{r}' - \mathbf{r} \right)$ is the Dirac delta-function. Here, we will use this low energy limit for simple tests in Chapter 4.

The total cross section $\sigma \left(v_{\mathrm{r}} \right)$, is obtained by integrating over only half the total solid angle, to avoid double counting, and is given by the sum of the total cross sections for each partial-wave,

$$\sigma \left(v_{\mathrm{r}} \right) = \sum_{l=0}^{\infty} \sigma_l \left(v_{\mathrm{r}} \right), \tag{2.13}$$

where

$$\sigma_l \left(v_{\mathrm{r}} \right) = 32\pi \left(2l + 1 \right) \left(\frac{\hbar \sin \delta_l}{m v_{\mathrm{r}}} \right)^2. \tag{2.14}$$

Chapter 3

Direct Simulation Monte Carlo Method

The DSMC method has a very strong following outside of ultra-cold-atom research, and is actively developed. We give a background to the DSMC method, and discuss general considerations, before presenting our DSMC algorithm.

3.1   Background to DSMC

The DSMC method is the most widely used tool for modeling fluid flow on the subcontinuum scale and has found itself successfully applied to a huge range of physics from shock waves [35] and Rayleigh-Bénard flow [43] to aerodynamics of spacecraft [44], chemical reactions [45], microfluidics [46], acoustics on Earth, Mars, and Titan [47], volcanic plumes on Jupiter's moon Io [48], and much more.

These situations are characterized by being dilute (two-body collisions) and having a high Knudsen number (Kn), which is given by the ratio of the mean-free path λ, to the representative length scale of the system L, i.e.,

$$\mathrm{Kn} = \frac{\lambda}{L}. \tag{3.1}$$

For $\mathrm{Kn} \gtrsim 0.1$, a microscopic kinetic theory is necessary, while for $\mathrm{Kn} \lesssim 0.1$, the system tends to be sufficiently hydrodynamic for a continuum approach to be applicable for understanding coarse-grained dynamics.[1][2] This is not to say that DSMC is inapplicable or is inefficient in this regime; indeed, recently, Bird has shown that, in nonequilibrium situations with $\mathrm{Kn} \sim 0.01$, the DSMC algorithm (employing many of the techniques we introduce for cold atoms

---

[1] In the cold-atom community, it is more common to specify these regimes as $\omega\tau$, where ω is the excitation frequency and τ is the collision time.

[2] For a detailed discussion on which regimes the various methods are traditionally used, see Ref. [44].

here) can be more accurate and efficient than Navier-Stokes methods, while also providing details of the microscopic (subcontinuum) dynamics [49]. We also note that the *consistent Boltzmann algorithm* [50] was developed by making an adjustment to the DSMC algorithm, where the positional shifts of the atoms due to collisions are taken into account, thus, giving the correct hard-sphere virial. This allows for exploration into even lower Kn and has been explored in the context of quantum nuclear flows [51, 52].

For reference, cold-atom experiments often operate in the collisionless regime (Kn > 1), however, values of Kn $\sim$ 0.01 have been explored, e.g., the above-critical temperature collective modes of a ^{23}Na gas studied by Stamper-Kurn *et al.* [4] had Kn $\sim$ 0.1; Shvarchuck *et al.* [1] studied the hydrodynamical behavior of a normal ^{87}Rb gas in which Kn $\sim$ 0.02−0.5.

3.2   Overview of Formalism and General Considerations

In the DSMC method, the distribution function is represented by a swarm of test particles,

$$f\left(\mathbf{p}, \mathbf{r}, t\right) \approx \alpha\, h^3 \sum_{i=1}^{\mathcal{N}_{\mathrm{T}}} \delta\left[\mathbf{p} - \mathbf{p}_i\left(t\right)\right] \delta\left[\mathbf{r} - \mathbf{r}_i\left(t\right)\right], \tag{3.2}$$

where $\alpha = \mathcal{N}_{\mathrm{P}}/\mathcal{N}_{\mathrm{T}}$ is the ratio of physical atoms ($\mathcal{N}_{\mathrm{P}}$) to test particles ($\mathcal{N}_{\mathrm{T}}$). These test particles are evolved in time in such a manner that $f\left(\mathbf{p}, \mathbf{r}, t\right)$ evolves according to the BE.

The basic assumption of DSMC is that the motion of atoms can be decoupled from collisions on time scales much smaller than the mean-collision time. In practice, this means that a simulation is split up into discrete time steps Δt, during which, the test particles undergo a collisionless evolution, then, collisions between test particles are calculated.

The relation of the test particles to physical atoms is apparent in Eq. (3.2) when $\alpha = 1$, but, in general, they are simply a computational device for solving the BE. In many conventional applications of DSMC, good accuracy can be obtained with $\alpha \gg 1$ (i.e., each is a *super particle* representing a larger number of physical atoms), however, in our applications to the nonequilibrium dynamics of ultracold gases, we often require $\alpha \ll 1$. Increasing the number of particles improves both the accuracy and the statistics of the simulation, and in highly nonequilibrium situations, it can be essential to have a large number of particles. The DSMC algorithm is designed so that the number of computational operations per time step scales linearly with the number of particles, i.e., $O\left(\mathcal{N}_{\mathrm{T}}\right)$. The recent work of Lepers *et al.* [25] departs from DSMC by using a stochastic particle method similar to that developed in nuclear physics for the simulation of heavy-ion collisions [53, 54], which tests if two particles are at their closest approach in the present time step, causing the algorithm to scale as

$O\left(\mathcal{N}_{\mathrm{T}}^{2}\right)$. These methods have been reformulated in terms of DSMC by Lang *et al.* [55]. We typically use $\mathcal{N}_{\mathrm{T}} = 10^5 - 10^7$ test particles, and, by the various improvements we describe below, in most cases we consider here, we can obtain accuracy to within 1%.

As pointed out in Sec. 2.1, the BE has a simple interpretation in terms of the flow of atoms through phase space. Hence, the collisionless evolution of the test particles is performed by solving Newton's laws for the potential $U\left(\mathbf{r}, t\right)$, and collisions are governed by the collision integral [Eq. (2.7)]. The collisions are implemented probabilistically (see Sec. 3.3.3) using a scheme that requires the particles to be binned into a grid of cells in position space. This serves two purposes: (i) It allows for the sampling of the distribution function, and (ii) it establishes a computationally convenient mechanism for determining which particles are in close proximity. Thus, the accuracy of DSMC depends on the discretization of the problem, the cell size, the time step, and $\mathcal{N}_{\mathrm{T}}$. It has been shown to converge to the exact solution of the BE in the limit of infinite test particles, vanishing cell size, and vanishing time step [56].

In the original DSMC algorithm [35], a test particle may collide with any other particle within the cell. This coarse grains position and momentum correlations, such as vorticity, to be the length scale of the cells, as observed by Meiburg [57]. If the cells are not small enough, this transfer of information across a cell could lead to nonphysical behavior. To combat this, we have employed a nearest neighbor collision (NNC) scheme [58] outlined in Sec. 3.3.3, where the collision partner of a particle must be chosen from the nearest neighbors. Although a NNC scheme alleviates this problem, the cell sizes still must be small in comparison to the local mean-free path and the length scale over which the density varies for accurate sampling.

The time step of the simulation must also be small in comparison to the smallest local mean-collision time to ensure the validity of the basic assumption of DSMC and that physical atoms do not propagate further than the local mean free path before colliding. To ensure this (and for added efficiency), we implement LATSs [58] where, instead of a single global time step, the time step can vary over the whole system, adapting to the local environment.

Finally, we note that the most useful choice of computational units (for the harmonic potential) for length, time, and energy, are respectively given by

$$x_0 = \sqrt{\frac{\hbar}{m\omega}}, \qquad t_0 = \frac{1}{\omega}, \qquad \epsilon_0 = \hbar\omega, \tag{3.3}$$

where ω is chosen to be ω_x, ω_y, or ω_z.

3.3 Implementation of DSMC

Here, we consider the basic implementation of DSMC; a collisionless evolution followed by a collision step where test particles are binned in position space and collisions between them are implemented stochastically via a collision probability. We also discuss the various adaptive schemes we employ for better accuracy and efficiency, while retaining the desired linear scaling of the computational complexity with test particle number.

3.3.1 Collisionless Evolution

The collisionless evolution is performed by a second-order symplectic integrator [59, 18], which updates the phase-space variables of the ith test particle in three steps:

$$\mathbf{q}_i = \mathbf{r}_i\left(t\right) + \frac{\Delta t}{2m}\mathbf{p}_i\left(t\right), \tag{3.4a}$$

$$\mathbf{p}_i\left(t + \Delta t\right) = \mathbf{p}_i\left(t\right) - \Delta t\,\nabla_{\mathbf{q}_i}U\left(\mathbf{q}_i, t\right), \tag{3.4b}$$

$$\mathbf{r}_i\left(t + \Delta t\right) = \mathbf{q}_i + \frac{\Delta t}{2m}\mathbf{p}_i\left(t + \Delta t\right). \tag{3.4c}$$

Symplectic integrators have the properties of conserving energy and phase-space volume over long periods of time. The conservation of phase-space volume is particularly desirable for fermionic simulations, since it assists in ensuring the Pauli exclusion principle is not violated during the collisionless evolution.

3.3.2 Master Grid and Locally Adaptive Cells

To perform collisions, we must first bin the test particles into a grid of cells according to their position. Collision partners are then selected from within each cell. In general, the binning occurs in up to two levels: (i) the *master grid* on which each master cell is a rectangular cuboid of equal size [see Fig. 3.1(a)] and (ii) the adaptive subdivision of the master cells into smaller LAC subcells dependent on the number of particles in the parent master cell [see Fig. 3.1(b)], which is an optional refinement. The use of several LAC schemes in DSMC is discussed in Ref. [35]. It is a useful refinement to the algorithm for applications to cold-atom systems, because these typically have large variations in density (such a scheme has been employed in Ref. [60] to account for the large change in density during evaporative cooling of a cloud of cesium atoms). We now discuss these levels in further detail.

At the beginning of the collision step, the grid of master cells is chosen to ensure all particles are held within its boundaries [see Fig. 3.1(a)]. We choose to keep the size of the master cells in each direction constant in time so that if the particles spread out further in

(a) Δx

Δy

master cells

adaptive subdivision
of master cells

(b) Δx

Δy
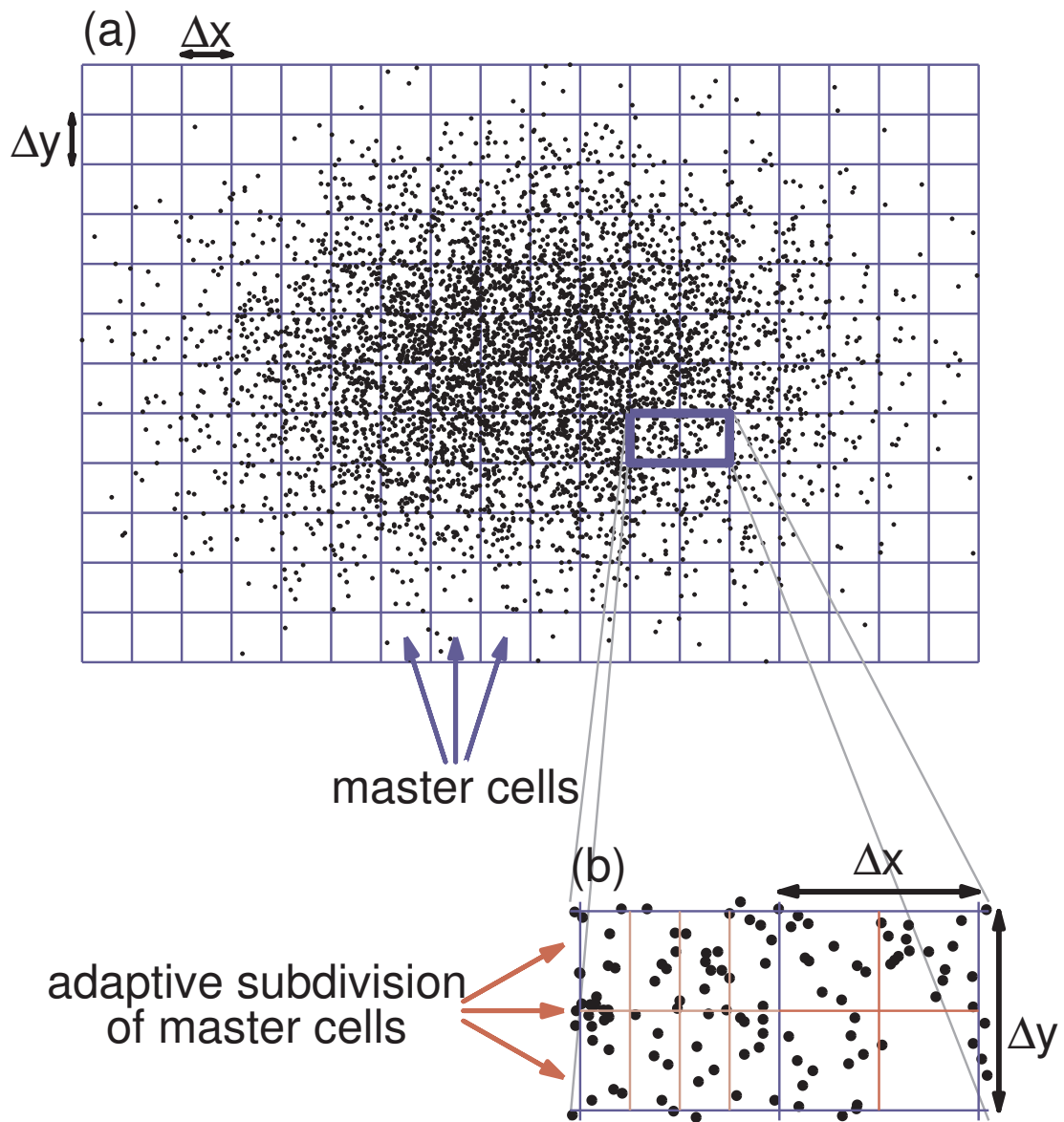
Figure 3.1: A two-dimensional schematic of the cells used for a swarm of
test particles. (a) The rectangular master cells are all of the same size and
are chosen to ensure all particles lie within the boundaries of this grid. Cell
boundaries are indicated by lines, and particles are indicated by dots. (b)
An enlargement of two master cells showing their adaptive subdivisions
into smaller LAC subcells. The number of LAC subcells is determined by
the number of particles within the master cell.

space during the simulation, we add extra cells rather than changing the size of the cells. The particles are then binned into these master cells, and the number of particles in each cell N_c is stored.

For adaptive subdivision, each master cell is considered in turn, and the particles are binned further into a grid of smaller LAC subcells according to N_c [see Fig. 3.1(b)]. Because the number of collisions within a cell increases with density (i.e., number of particles), the subdivision of highly occupied master cells gives a finer resolution of spatial regions where the local collision rate is highest and, hence, more accurate simulations.

Our subdivision procedure aims to produce cells in which the average number of particles is close to some threshold value N_{th} for which the choice of is discussed in Sec. 4.2.2. In our algorithm, we do this by finding the integer l such that $N_c/2^l$ is closest to, but not less than, N_{th}. The master cell is then subdivided into 2^l subcells, while giving no preference to any direction in this subdivision. We choose this division scheme over more complicated schemes, as when additionally implementing LATSs, the protocol for dynamically changing grids becomes simpler.

We have adopted the notation of specifying quantities pertaining to a particular cell by a subscript c. In what follows, when referring to cells, we will mean finest level of cells, i.e., the LAC subcells or master cells otherwise. We do not explicitly label the cells, indeed, this is to partly emphasize that the calculations performed in each cell are independent of other cells. Thus, the algorithm is intrinsically parallel and is suitable for implementation on parallel platforms (e.g., see Ref. [46]).

3.3.3 Collisions

Number of Tested Collisions

The BE describes the evolution of the continuous distribution $f(\mathbf{p}, \mathbf{r}, t)$. However, the replacement of $f(\mathbf{p}, \mathbf{r}, t)$ with a swarm of test particles introduces fluctuations that do not correspond to physical fluctuations when $\mathcal{N}_{\text{P}} \neq \mathcal{N}_{\text{T}}$. As a result, hydrodynamic quantities are required to be obtained from the averages of mechanical variables, not the average of their instantaneous values [61].

In these stochastic particle methods, the collisions of test particles inherently average the instantaneous values of the collision rate. This leads to a biasing of the total collision rate when cells have low occupation numbers (see Fig. 3.2).

The probability distribution of the N_c test particles within a cell is well approximated by
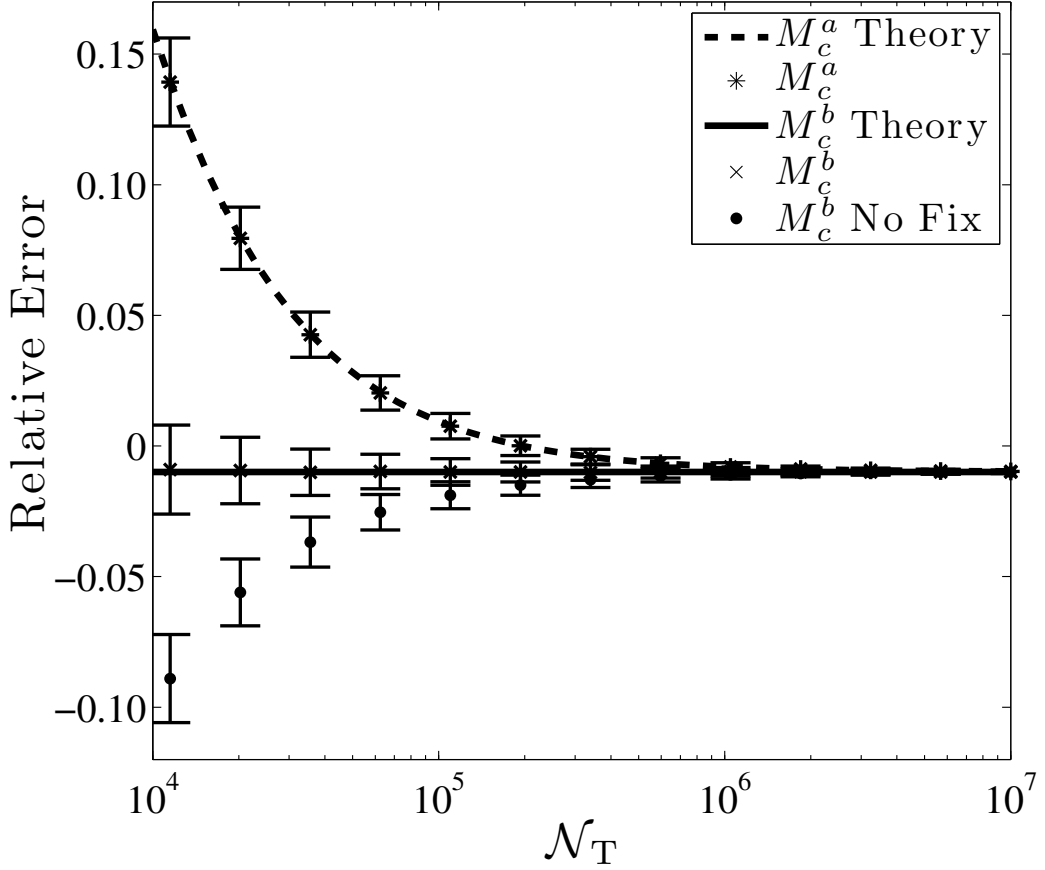
Figure 3.2: Relative error of the numerical total collision rate in the case of the equilibrium distribution [Eq. (4.7)] for the choices of M_c, where the error bars indicate the standard deviations of 500 averages. Here, the original DSMC algorithm is implemented with $\mathcal{N}_T = 10^7$ and bin parameter [Eq. (4.16)] $\gamma = 0.2$. The choice M_c^a is seen to diverge for low $\mathcal{N}_T$ as $\overline{N_c}$ in Eq. (3.8) becomes appreciable, which agrees well with the theoretically calculated error (M_c^a theory) using Eq. (3.8). Using M_c^b removes this divergence, and the error is seen to agree well with the expected error for this discretization (M_c^b theory). The final data set (M_c^b no fix) demonstrates the error that arises when $\tilde{M}_c$ having non integer values after rescaling, is not accounted for [i.e., not including the ceiling function in Eq. (3.14)]. The system parameters are given in Fig. 4.7. [See Sec. 4.2 for the details of the DSMC simulation].

the Poisson distribution [62] of which the variance is equal to the mean, i.e.,

$$\overline{\delta N_c^2} = \overline{N_c^2} - \overline{N_c}^2 = \overline{N_c},$$
(3.5)

where $\delta N_c = N_c - \overline{N_c}$. Note that, formally, the correct number of collisions to test (given by elementary scattering theory and the derivation of the collision probability from the collision integral (2.7) via the Monte Carlo integration [18]) is

$$M_c^a = \frac{N_c^2}{2}.$$
(3.6)

However, with Poissonian fluctuations in N_c, we find that the mean collision rate is $R \propto \overline{M_c} \sim \overline{N_c}^2 + \overline{N_c}$ (but should be $\propto \overline{N_c}^2$). Thus, Poissonian fluctuations can become important when the number of test particles per cell is small. However, the effect of fluctuations from the finite-test particle number can be bypassed (e.g., see Ref. [49]) by instead using the number of possible pairs of test particles,

$$M_c^b = \frac{N_c \left(N_c - 1 \right)}{2},$$
(3.7)

which we have employed in this work.

   To understand the difference in detail, we note that the average calculated by the DSMC simulation (denoted by the asterisks) for Eq. (3.6) is

$$\overline{N_c^2}^* = \overline{N_c}^2 + \overline{N_c} - P_1,$$
(3.8)

where P_1 is the probability of $N_c = 1$ (as the simulation ignores cells with $N_c = 1$, for which no collisions occur, and this must be subtracted from the average). While, for expression (3.7),

$$\overline{N_c \left(N_c - 1 \right)}^* = \overline{N_c}^2,$$
(3.9)

which gives the correct total collision rate for the physical system as seen in Fig. 3.2.

Collision Probability and Scaling

The collision probability for a pair of test particles i and j in a cell of volume ΔV_c is given by

$$P_{ij} = \alpha \frac{\Delta t}{\Delta V_c} v_r \sigma \left(v_r \right).$$
(3.10)

This collision probability can be derived from the collision integral (2.7) via the Monte Carlo integration [18] (see also Sec. 6.1), the kinetic arguments [35], or the elementary scattering theory [54]. The correct collision rate is established by testing

$$M_c = \frac{N_c \left(N_c - 1 \right)}{2}$$
(3.11)

collisions in the cell. This is inefficient as the number of operations scales as $\mathcal{N}_{\mathrm{T}}^2$, and the collision probability may be far less than 1. However, within a cell, the collision probabilities and the number of tested collisions can be rescaled by a single parameter Λ such that the number of operations scales as $\mathcal{N}_{\mathrm{T}}$ [35],

$$P_{ij} \rightarrow \tilde{P}_{ij} = \frac{P_{ij}}{\Lambda}, \tag{3.12a}$$

$$M_c \rightarrow \tilde{M}_c = M_c \Lambda, \tag{3.12b}$$

and still converge to the same BE evolution. Here, Λ is chosen to be

$$\Lambda = \frac{\left\lceil M_c \alpha \frac{\Delta t}{\Delta V_c} \left[v_{\mathrm{r}} \sigma \left(v_{\mathrm{r}} \right) \right]_{\max} \right\rceil}{M_c}, \tag{3.13}$$

where $\left[v_{\mathrm{r}} \sigma \left(v_{\mathrm{r}} \right) \right]_{\max}$ is the maximum of this quantity over all pairs of particles in the cell and $\lceil x \rceil$ denotes the ceiling function. This corresponds to Bird's proposal of using $\Lambda = \max \{ P_{ij} \}$ [35], while we ensure that M_c is an integer and at least one collision is tested (Fig. 3.2 demonstrates the reduction in collision rate, if this is not taken into account). With this choice of scaling, the maximum collision probability within the cell is less than or equal to 1, but is expected to be close to 1, and the number of collisions that need to be tested is reduced to

$$\tilde{M}_c = \left\lceil \frac{N_c - 1}{2} n_c \Delta t \left[v_{\mathrm{r}} \sigma \left(v_{\mathrm{r}} \right) \right]_{\max} \right\rceil, \tag{3.14}$$

where

$$n_c = \alpha N_c / \Delta V_c, \tag{3.15}$$

is the average density in the cell.

This enhancement of efficiency is often missed by other stochastic particle methods, or the collisions are adjusted in some other manner. For example, Tosi *et al.* [27] introduced a scheme for fermions where collision pairs with small classical collision probability were neglected.

Nearest Neighbor Selection of Collision Partners

We employ a NNC scheme to combat discretization effects from finite cell sizes, in particular, the so-called *transient adaptive subcell* (TASC) scheme [58]. Simple sorting of the test particles for the nearest neighbors scales quadratically with the particle number. The TASC sorting scheme retains linear scaling, but it does not guarantee the exact nearest neighbor.

The basic TASC scheme is to further bin the particles into subcells within the cell [see Figs. 3.3(a) and 3.3(b)], the number of which is roughly equal to N_c. In our case, the number

(a)

collision pair

transient sub-cells

central sub-cell

(b)

collision pair

layer 3   layer 2   layer 1
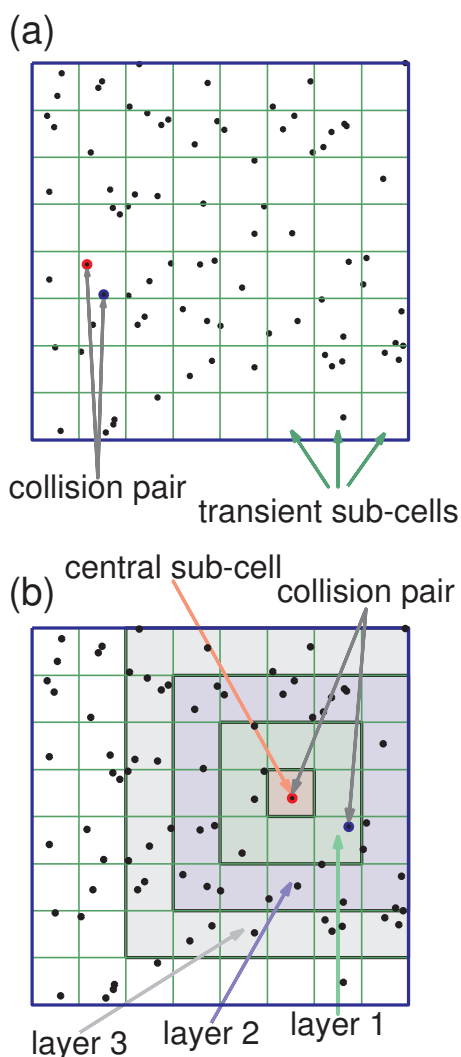
Figure 3.3: A two-dimensional schematic of how collisions are performed within the TASC scheme. A single cell (outer boundary line) and the distribution of test particles (black dots) are shown in (a) and (b) for two different random collisions. The finer grid of internal lines represents the boundaries of the TASC subcells. The first particle of the collision pair is selected at random from all the particles in the cell. In (a), the first particle occupies a TASC subcell that contains other particles, and the second participant in the collision is chosen at random from these other particles. In (b), the first particle (which occupies the *central subcell*) is the sole occupant of a TASC subcell. In this case, we check to see if there are any particles in layer 1, and if so, the collision partner is chosen at random from these other particles. If there were no particles in layer 1, we would then check layer 2, and so on.

of subcells in each direction is equal and is given by $\lfloor \sqrt[3]{N_c} \rfloor$ (with $\lfloor x \rfloor$ as the floor function). When a particle is randomly picked for a collision, its collision partner is established by looking within the immediate TASC subcell [Fig. 3.3(a)], and if not found [Fig. 3.3(b)], each layer starting closest to the particle is searched for other particles. If a layer contains more than one particle, the collision partner is randomly chosen from that set to avoid any biasing. This reduces the distance between colliding pairs significantly and may be decreased even more by increasing $\mathcal{N}_T$.

We use this procedure to select each of the $\tilde{M}_c$ pairs of particles for testing if a collision occurs. We also ensure a particle does not undergo a second collision in the same time step.

Testing and Implementation of Collisions

For each of the pairs, the collision goes ahead if $R < \tilde{P}_{ij}$, where R is a random number uniformly distributed between 0 and 1. As the BE describes binary collisions of point-like atoms that conserve total energy and momentum, only the momenta are changed by keeping the total momentum constant, and the relative momentum vector is rotated about its centre (see Fig. 2.1 or Fig. 3.4). The scattering angles ϕ and θ, are determined by using an acceptance-rejection Monte Carlo algorithm for the differential cross section.

The final momenta of the test particles are given by

$$\mathbf{p}' = \mathbf{P} + \frac{\mathbf{p}'_r}{2}, \tag{3.16a}$$

$$\mathbf{p}'_1 = \mathbf{P} - \frac{\mathbf{p}'_r}{2}, \tag{3.16b}$$

hence, we need to determine $\mathbf{p}'_r$ in the reference frame of the simulation.

In the centre-of-mass reference frame shown in Fig. 3.4, $\mathbf{p}'_r$ is given by a rotation about origin (centre of the relative momentum),

$$\{\mathbf{p}'_r\}_{\text{com}} = p_r \begin{pmatrix} \sin\theta\cos\phi \\ \sin\theta\sin\phi \\ \cos\theta \end{pmatrix}. \tag{3.17}$$

To transform to the reference frame of the simulation, two rotations are required, which are defined by the angles ϕ' and θ'. We take θ' to be the angle between $\mathbf{p}_r$ and the p_z axis in the simulation reference frame, and ϕ' to be the azimuthal angle (i.e., how ϕ and θ are defined in the centre-of-mass frame Fig. 3.4). Thus, $\mathbf{p}'_r$ is rotated about the p_x axis, then, about the p_z axis by $R_z R_x$, where
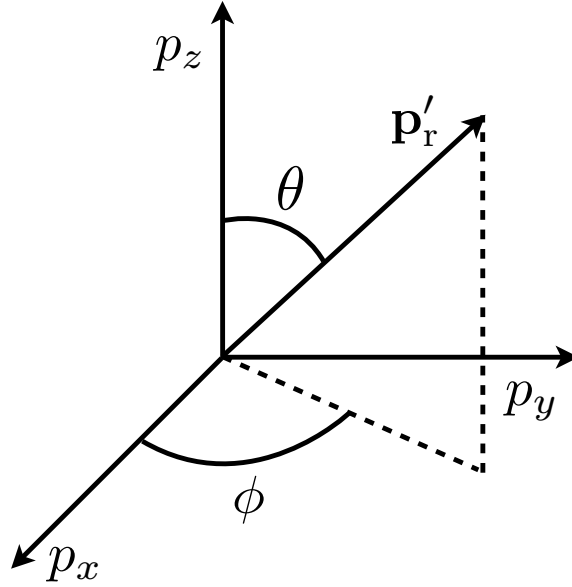
Figure 3.4: In the centre-of-mass reference frame, where the relative momenta initially points along the p_z axis, the collision causes the relative momenta to be rotated about its centre to the new relative momenta $\mathbf{p}'_r$.

$$
R_x = \begin{pmatrix} 1 & 0 & 0 \\ 0 & \cos\theta' & \sin\theta' \\ 0 & -\sin\theta' & \cos\theta' \end{pmatrix}, R_z = \begin{pmatrix} \sin\phi' & \cos\phi' & 0 \\ -\cos\phi' & \sin\phi' & 0 \\ 0 & 0 & 1 \end{pmatrix}. \tag{3.18}
$$

In terms of the components of $\mathbf{p}_r = (p_a, p_b, p_c)$, this gives

$$
R_z R_x = \frac{1}{p_r p_d} \begin{pmatrix} p_r p_b & p_a p_c & p_d p_a \\ -p_r p_a & p_b p_c & p_d p_b \\ 0 & -p_d^2 & p_d p_c \end{pmatrix}, \tag{3.19}
$$

where $p_d^2 = p_a^2 + p_b^2$.[3] Thus, in the simulation reference frame,

$$
\mathbf{p}'_r = \frac{1}{p_d} \begin{pmatrix} \sin\theta\,(p_r p_b \cos\phi + p_a p_c \sin\phi) + p_d p_a \cos\theta \\ \sin\theta\,(p_b p_c \sin\phi - p_r p_a \cos\phi) + p_d p_b \cos\theta \\ p_d\,(p_c \cos\theta - p_d \sin\theta \sin\phi) \end{pmatrix}. \tag{3.20}
$$

---

[3]In the special case where $\theta' = 0$, we take Eq. (3.19) to be the identity, i.e., $\phi' = \pi/2$. In simulations, the identity is used when $p_d \leq eps$, where eps is the numerical precision.

3.3.4 Locally Adaptive Time Steps

All of the preceding aspects of our implementation of DSMC can be performed with the single global time step Δt for all cells such that the evolution of the system is simulated at the times $t_k = k \, \Delta t$, with k as an integer. At each of these steps, the collisionless evolution is performed, then, is followed by the collision step [see Fig. 3.5(a)]. However, if there is large variation in the properties over the system, the use of a single time step can be inefficient, as it may be much smaller than required for low-velocity or low-density regions. This has been addressed by a recent improvement to the DSMC algorithm [58], where a local time step was introduced for the collision step. Performing the collision step is computationally expensive, so this improvement can lead to a great increase in the efficiency of calculations.

With the use of LATSs, there are two time steps of importance for each cell: (i) The global time step δt_i, which is the fundamental increment of time in all cells of the system. The global time after k steps is specified as

$$t_{\mathrm{g}} = \sum_{i=1}^{k} \delta t_i, \tag{3.21}$$

and during each increment of δt_i, collisionless evolution is performed [i.e., Eqs. (3.4a)−(3.4c) with $\Delta t \to \delta t_i$]. (ii) The local time step for the cell δt_c, which is the desirable time scale for performing collisions in this particular cell. Note $\delta t_i = \min\{\delta t_c\}$, i.e., we choose the global time step to be the smallest value of δt_c over all cells in the system at the end of each step.[4]

A collision step is performed at the global time step when, at least, a time of δt_c has passed since the last collision step for the cell under consideration [see Fig. 3.5(b)]. To implement this, we introduce a cell timer t_c, indicating the time up to which collisions have been accounted for in the cell. In general, $t_c < t_{\mathrm{g}}$ and is incremented by δt_c during each collision step. Performing collisions in this way ensures that t_c is within δt_c of t_{g} at all times,[5] and at the end of the simulation, all t_c are updated to the final time by performing collisions with $\delta t_c = t_{\mathrm{g}} - t_c$.

In our simulations, δt_c is chosen to be small compared to the relevant collision and transit

---

[4]If δt_i is sufficiently large that the accuracy of the collisionless evolution is compromised, δt_i is split into smaller increments for this evolution.

[5]If a cell becomes unpopulated ($N_c = 0$), t_c may not have been updated such that $t_c = t_{\mathrm{g}}$ before the test particles leave the cell, which decreases the collision rate. However, δt_c is chosen such that this effect is negligible.
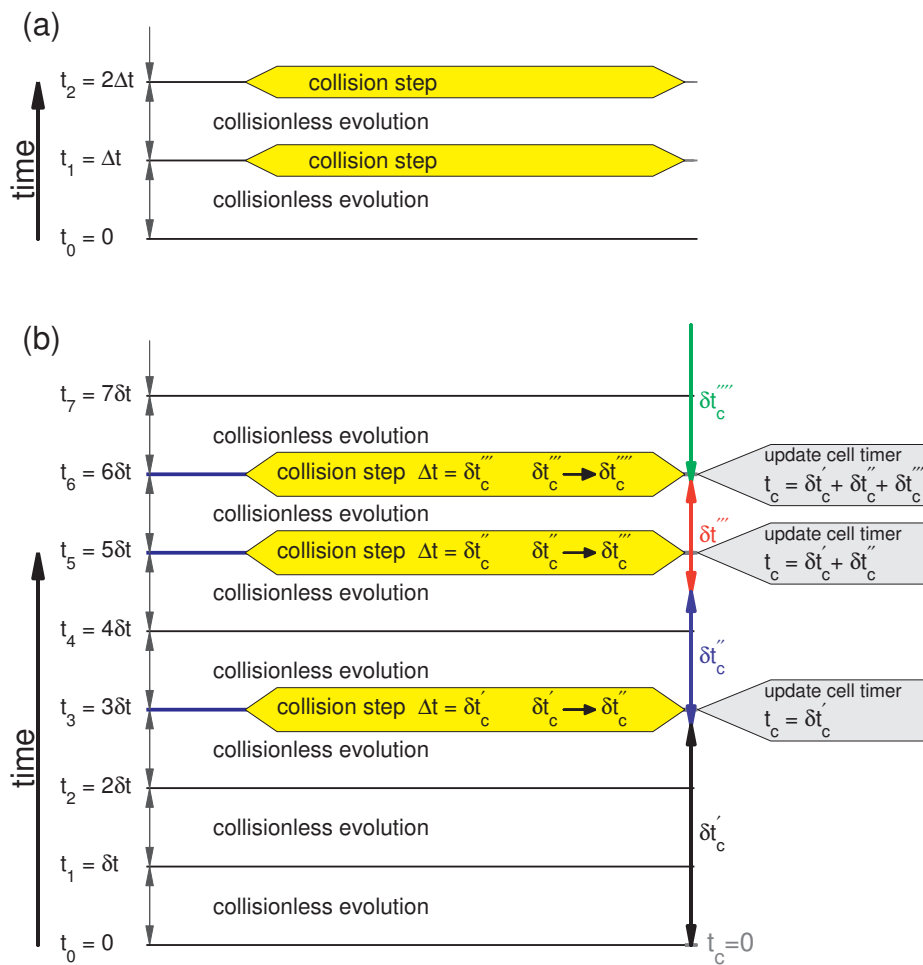
Figure 3.5: An example of the sequence of steps in a DSMC evolution. (a) A simple DSMC scheme where the whole system evolves according to a single global time step Δt. (b) An example of a cell using a LATS. In this example, the global time step (δt) is held constant, while the local time step (δt_c) is shown to vary. Collisionless evolution occurs at each global time step. A collision step is performed at the global step when, at least, δt_c has passed since the last collision step. At global time t_3, we show a collision step, at which the local time counter (t_c) is updated and a new local time step ($\delta t_c''$) is established. Here, the local time step decreases, showing two further collision steps that follow shortly after the first.

times of the cell. In detail, these time scales,

$$\tau_c^{\text{coll}} = \left[n_c \overline{v_{\text{r}} \sigma \left(v_{\text{r}} \right)} \right]^{-1}, \tag{3.22a}$$

$$\tau_c^{\text{max}} = \left\{ n_c \left[v_{\text{r}} \sigma \left(v_{\text{r}} \right) \right]_{\text{max}} \right\}^{-1}, \tag{3.22b}$$

$$\tau_c^{\text{tr}} = \min \left\{ \frac{\Delta x_c}{\overline{v}_x}, \frac{\Delta y_c}{\overline{v}_y}, \frac{\Delta z_c}{\overline{v}_z} \right\}, \tag{3.22c}$$

are the mean-collision time, the maximum collision time, and the mean transit times of the cell, respectively. These expressions are evaluated at the end of each collision step, and the mean speeds $(\overline{v}_x, \overline{v}_y, \overline{v}_z)$ are given by averaging over all the test particles within the cell, while $\overline{v_{\text{r}} \sigma \left(v_{\text{r}} \right)}$ is the average of $v_{\text{r}} \sigma \left(v_{\text{r}} \right)$ over the particles tested for collisions. The cell widths $(\Delta x_c, \Delta y_c, \Delta z_c)$ correspond to the cell under consideration [e.g., Δx_c is the LAC subcell x width, and the master bin width (Δx) otherwise].

In terms of these time scales, we take

$$\delta t_c = \min \left\{ \eta_{\text{coll}} \tau_c^{\text{coll}}, \eta_{\text{max}} \tau_c^{\text{max}}, \eta_{\text{tr}} \tau_c^{\text{tr}} \right\}, \tag{3.23}$$

where η_{coll}, η_{max}, and η_{tr} are constants less than unity. At the end of each collision step, δt_c is reset by Eq. (3.23). Whenever δt_c is established without performing a collision step, i.e., beginning of the simulation or when the LAC subcells are collapsed or expanded, we take it to be

$$\delta t_c = \min \left\{ \eta_{\text{max}} \tau_c^{\text{max}}, \eta_{\text{tr}} \tau_c^{\text{tr}} \right\}. \tag{3.24}$$

For the accurate simulation of dynamics, it is required that $\delta t_c \ll \tau_c^{\text{coll}}$ as well as $\delta t_c \ll \tau_c^{\text{tr}}$. We also require that it is unlikely for an atom to undergo multiple collisions in a collision step (accounted for by τ_c^{max}). These requirements are ensured by the constants η_{coll}, η_{max}, and η_{tr}, which are optimized for the desired accuracy.

Care has to be taken when the LATS scheme is implemented in conjunction with the LAC scheme, as the cells can change dynamically during the evolution (cells can be resized, can be added or can be removed). Our procedure for dealing with dynamically changing LAC subcells is as follows: As each master cell is considered in turn, if the number of LAC subcells changes, a new layout of LAC subcells must be established. If the number of these subcells increases, then each of these new cells inherits the t_c of the original cell. Alternatively, if the number of subcells decreases, then the new cells are formed by merging old cells. In general, the values of t_c for each of the cells to be merged are different, and we take the new value of t_c to be the largest of these. This requires t_c of the old cells to be updated to the new t_c, thus, collision steps are performed within the old cells before merging, using the time difference.

When the LAC scheme is implemented with small threshold numbers (e.g., $N_{\text{th}} < 5$) and the number of test particles is large ($\mathcal{N}_{\text{T}} > 10^6$), it can become inefficient to implement LATSs in conjunction with the LAC subcells. In such regimes, very dense grids of LAC subcells typically arise, for which the computational intensity of the LATS and memory requirements become too great. Furthermore, small cell sizes lead to excessively small time steps (e.g., τ_c^{tr} is proportional to the cell size), which further reduces the algorithm efficiency. In these cases, it is more efficient to implement the LATS scheme for the master cells (i.e., only the master cells have a time counter and desired time step) and implement collisions in all the LAC subcells using that same desired time step.

3.4 Algorithm and Code Development

The algorithm and code to perform these DSMC calculations was developed over the course of a year. In that time, our initial algorithm, based on the work of Jackson and Zaremba [18] was converted from MATLAB to C programming language, and parallelized. Many problems with the Jackson and Zaremba algorithm were identified, understood, and solved, by experimentation and finding relevant literature. Most problems were in relation to simulating far from equilibrium systems, which the Jackson and Zaremba algorithm was not developed with this in mind. However, there were two crucial problems: the choice of the number of tested collisions (see Sec. 3.3.3), and a problem in relation to implementing quantum many-body statistics that we discuss in detail in Chapter 6. Both of these problems, can significantly damage the quality of the simulation.

The final DSMC algorithm, which we presented in this chapter, evolved after testing many different possible routines and subroutines, taking into consideration speed and memory constraints. We now briefly outline our implementation of this DSMC algorithm in C language. While, a significant amount of work has been simultaneously undertaken on a quantum DSMC implementation, we only seek to outline an algorithm in Chapter 6, as we have discovered, such an algorithm merits a significant study in its own right.

The main routine is split into three elements that are required to be executed in serial, and are repeated for each time step of the simulation,

   (i) Collisionless evolution.

  (ii) Establishing the master grid and binning test particles into it.

 (iii) Performing collisions.

Element (i) is the implementation of Eqs. (3.4a)−(3.4c), which is easily parallelized, and is

fast. As for element (ii), the master grid from the previous time step must be expanded if the test particles have evolved outside its boundaries. The master grid holds all the information about the LAC subcells within each master cell (or itself, if the LAC scheme is not implemented), i.e., how many in each direction, cell time steps, cell time counters, etc. It also holds the information of which test particles are within each master cell. This has to be established each time step, where the cell position of each test particle is established, and they are sorted into the cells. Components of this routine are not parallelizable, and in element (ii), there can be large manipulation of memory, causing it to take as long as element (iii).

The last element is the most difficult and intricate, and is usually the most computationally intensive. Thankfully, performing collisions in each master cell is independent of the other master cells. Thus, parallelizing this element is straightforward, by passing each thread a proportion of the master cells. As each master cell is considered, it must be determined if the layout of LAC subcells needs to be changed. If it does, then, the cells must be merged or subdivided, where the most difficult part is dealing with redistributing the time counters and time steps of each LAC subcell (see Sec. 3.3.4). Then, test particles are binned into the LAC subcells, using the routines for the master cell binning. From here, each LAC subcell is considered in turn, and the collisions are finally calculated if the time counter of the cell has fallen behind the global time by its time step. If it has, collisions are calculated, where the number of collisions and collision probabilities are given by Eqs. (3.12). This requires establishing the TASC subcells, where the test particles are binned into a grid of TASC subcells using the routines for the master cell binning. From this grid, the nearest neighbors are selected. If the collision goes ahead, the momenta of the colliding particles are adjusted according to Eqs. (3.16), and Eq. (3.20).

Chapter 4

Initial Investigation

Before we can perform DSMC simulations, the problem must be established by choosing inputs that suitably describe the ultra-cold-atom collider experiment [32], and justifying the neglect of the effect quantum statistics on scattering (Bose-stimulated scattering or Pauli-blocking). This is the purpose of the first section of this chapter.

In the ultracold gas community, with only a few exceptions, careful studies on the performance of DSMC, and other stochastic particle methods, are not presented along side the studies employing these methods. One of the purposes of this work was to establish the accuracy of DSMC, and, as noted in Sec. 3.3.3, a poor implementation of DSMC will result in significant error. To quantify the accuracy of the DSMC simulations, the second section develops tests relevant to ultracold systems, and for the particular case of colliding clouds, our DSMC algorithm is compared to highly accurate pseudo-spectral methods in a simplified case, finding excellent agreement.

Finally, we demonstrate the simulation of the ultra-cold-atom collider with the full energy and angular-dependent-scattering cross section, and consider the long-time dynamics of the collider. In particular, we investigate the delicate problem of rethermalization, and revisit fluctuations in relation to this.

4.1   Establishing the Problem

To describe the ultra-cold-atom collider, the BE requires a differential cross-section, a potential, and initial conditions, all of which must reflect the experiment. We now discuss the choices of these in detail, and we justify neglecting the effect quantum statistics on the collisions (Bose-stimulated scattering or Pauli-blocking).

4.1.1 Collisional Cross-Section

The ultra-cold-atom collider experiment [32] was conducted with ^{87}Rb, which is bosonic, prepared in a single hyperfine spin state ($F = 2, m_F = 2$). The wave function for two such colliding atoms is required to be symmetric, hence, only the even partial-wave terms in Eq. (2.9) contribute to the differential cross section. At the collision energies of the experiment, only the first two even terms contribute, $l = 0$ and $l = 2$ (s- and d-wave). Thus, the differential cross section reduces to

$$\frac{d\sigma}{d\Omega} = \frac{4\hbar^2}{m^2 v_{\mathrm{r}}^2} \left[\overbrace{4\sin^2\delta_0}^{s\,\text{wave}} + \overbrace{25\sin^2\delta_2\left(3\cos^2\theta - 1\right)^2}^{d\,\text{wave}} \right.$$

$$\left. + \underbrace{20\cos\left(\delta_0 - \delta_2\right)\sin\delta_0\sin\delta_2\left(3\cos^2\theta - 1\right)}_{s\text{- and }d\text{-wave interference}} \right], \tag{4.1}$$

and the total cross section is given by the sum of the individual s- and d-wave cross sections,

$$\sigma\left(v_{\mathrm{r}}\right) = \frac{32\pi\hbar^2}{m^2 v_{\mathrm{r}}^2}\left(\sin^2\delta_0 + 5\sin^2\delta_2\right). \tag{4.2}$$

Calculation of the collision energy dependence of the phase shifts δ_0 and δ_2 is a nontrivial task. The values that we use in our simulations [Fig. 4.1(a)] are those calculated by Thomas *et al.* and reported in Ref. [32]. Over the range of collision energies shown in Fig. 4.1, the interference between s- and d-wave scatterings can be important, and a d-wave resonance also occurs. The d-wave resonance can be seen in Fig. 4.1(b) as the peak of the total cross section, attributed to the large d-wave cross section.

4.1.2 Potential and Initial Conditions

Here, we discuss an *ab initio* description of the system and find such a description not possible due to the magnetic fields being insufficiently characterized. Hence, we resort to a simplified description, which we discuss in the last portion of this section.

Ab initio model of the collider

The collisions of the clouds were performed as follows: the atoms were magnetically trapped in a single-well configuration (quadrupole-Ioffe-configuration trap) [63], then, the trap was adiabatically transformed into a double-well configuration [64] [Fig. 4.2(a)]. This spatially separates two segments of the initial cloud, and the separation distance is a controllable parameter, on which, T_{coll} depends. The collision is initiated by rapidly transforming back
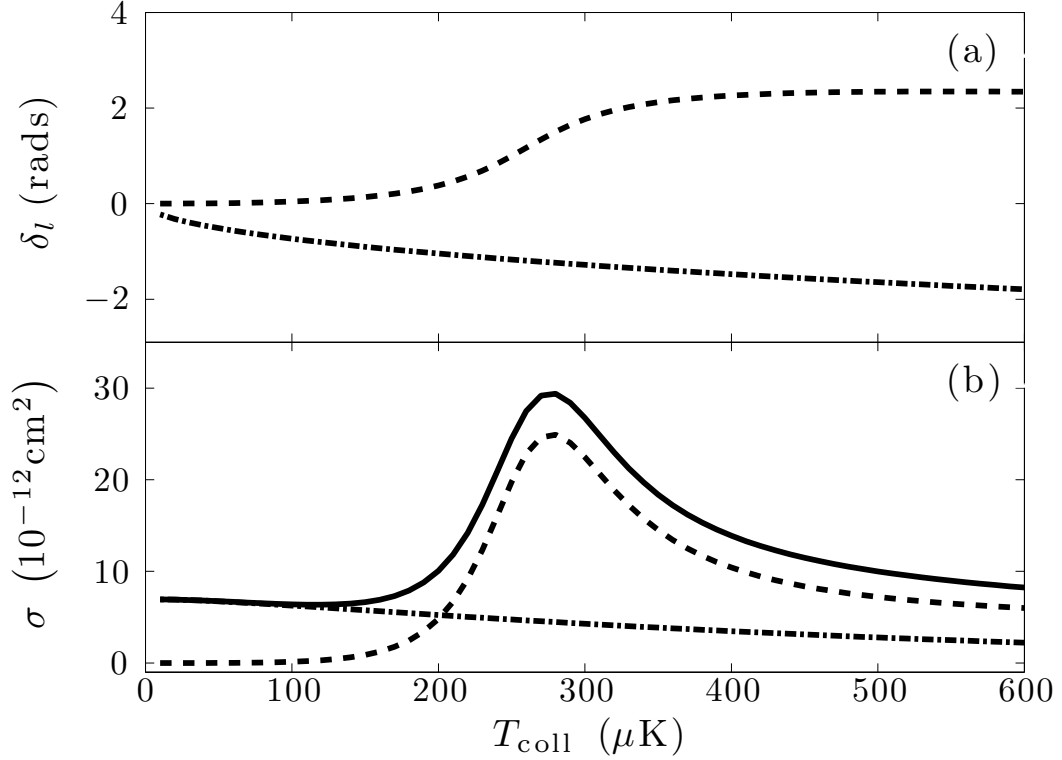
Figure 4.1: (a) Numerically calculated *s*-wave (dotted line) and *d*-wave (dashed line) phase shifts of Ref. [32]. (b) *s*-wave (dotted line), *d*-wave (dashed line), and total (solid line) cross sections.

to the single-well configuration [Fig. 4.2(b)], accelerating the clouds towards each other, causing them to collide near the minimum of the potential [Fig. 4.2(c)].

In the single-well configuration, the potential is approximately harmonic near the trap minima,

$$U(\mathbf{r}) = \frac{m}{2} \left(\omega_x^2 x^2 + \omega_y^2 y^2 + \omega_z^2 z^2 \right), \tag{4.3}$$

and cylindrically symmetric about the collision axis (*z* axis), i.e., $\omega_x = \omega_y$. The experimentaly measured trapping frequencies are

$$\omega_x = \omega_y = 2\pi \times 155 \, \text{Hz}, \tag{4.4a}$$

$$\omega_z = 2\pi \times 12 \, \text{Hz}. \tag{4.4b}$$

After the collision, the scattered atoms, and remaining unscattered atoms, evolved in the trap for quarter of the radial trap period $\pi/4\omega_x$, then, the system was imaged using absorption imaging techniques. In allowing the atoms to propagate for this time, the bulk of the scattered
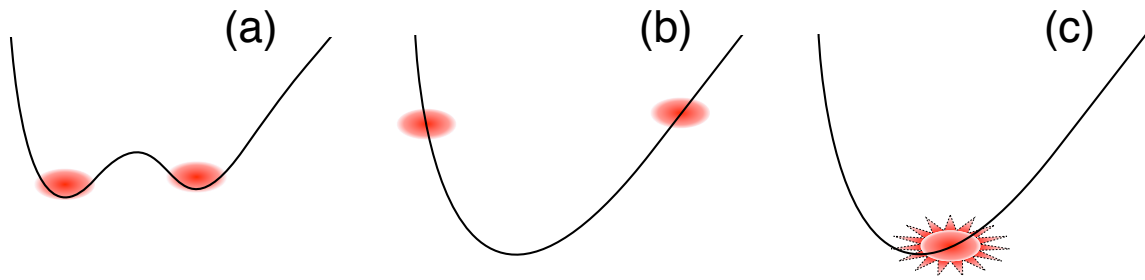
Figure 4.2: A schematic of the collision process. A qualitative potential along the collision axis is indicated by the sold black line, while the atoms are indicated by the red clouds. (a) shows two spatially separated clouds, while the potential is in the double-well configuration. The potential is rapidly transformed to the single-well configuration (b), and the clouds accelerate towards each other. The clouds collide away from the trap center (c), due to the asymmetric nature of the trapping potential.

atoms reach their maximal extent in the radial direction while in the trap, thus, giving the best resolution possible.

The single-well and double-well configurations are generated by three coils (shown in Fig. 4.3) and a rotating bias field that is used to avoid trap losses due to Majorana spin flips. The double-well configuration was established by increasing the current (initially 27 A) to the quadrupole coils, and after cooling, the amplitude of the rotating bias field was $0.2\,\mathrm{mT}$.

The potential generated by these coils is asymmetric along the collision axis of the clouds (Ioffe coil axis), which results in the clouds being asymmetric with respect to each other (e.g., see the results of Ref. [32] in Fig. 1.2). Hence, it would be desirable to model the collision *ab initio* with an analytic form of the potential. Assuming that the ramp from the double-well to the single-well configuration is fast compared to the timescales of the system, and does not cause large fluctuations in the magnetic fields, we may use the double-well potential and measured temperature of the atoms for the initial conditions, and then, the single-well potential for dynamics.

The potential the atoms experience from the magnetic field is given by

$$U\left(\mathbf{r}\right) = -\boldsymbol{\mu} \cdot \mathbf{B} = g_F m_F \mu_\mathrm{B} B, \tag{4.5}$$

where $\boldsymbol{\mu}$ is the magnetic moment of the atoms, hence, g_F is the Landé g-factor, and μ_B is the Bohr magneton. Equations for the magnetic fields in the single-well configuration about
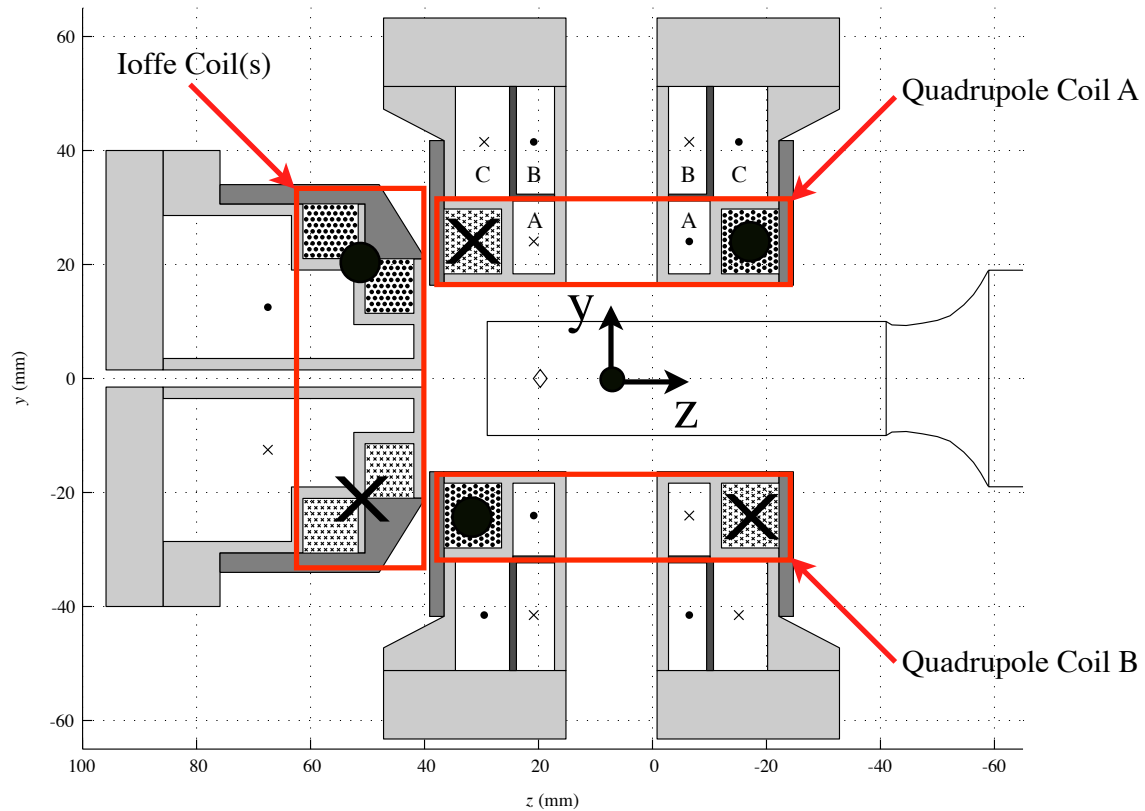
Figure 4.3: A schematic of the coils used for the experiment [32], which was presented in Ref. [65]. Each coil is wound around a former (light grey) with the current direction for each turn either into or out of the page ($\times$ and $\bullet$ respectively). The Ioffe coil (left coil) has 135 turns, while the quadrupole coils (upper and lower coils) have 100 turns each. The operational current for the coils is given to be 27 A. For our modeled potential, the origin is the center of the two quadrupole coils, and is indicated by the overlaid axes. The x direction points out of the page, y up the page, and the z direction is along the Ioffe coil axis.

the trap center are given in Ref. [65]. However, we require analytic equations that extend over the entire range that the atoms occupy during the course of the collision, for the initial conditions, as well as, implementing the collisionless evolution of the test particles in the DSMC algorithm [Eqs. (3.4a)−(3.4c)]. To do this, we extend the methods of Ref. [65], by treating the coils in Fig. 4.3 as current densities, and using the Biot-Savart law. This requires an expansion about the center of the quadrupole coils (see Fig. 4.3), and the resulting magnetic field magnitude must be time averaged, since the total magnetic field includes the rotating bias field. The potential is well approximated by a harmonic potential in the x and y dimensions, however, along the collision axis (z axis), the potential is asymmetric and requires z terms to be kept to tenth order. This causes the clouds to collide away from the single-well minima, and have different velocities. Furthermore, the harmonic trapping frequencies in the x and y directions vary along the collision axis, which leads to the clouds having different initial shapes and undergoing different shape oscillations as they accelerate towards the trap center.

About the single-well minima, the trapping frequencies determined by our model are

$$\omega_x = \omega_y = 2\pi \times 122\,\mathrm{Hz}, \tag{4.6a}$$

$$\omega_z = 2\pi \times 15\,\mathrm{Hz}, \tag{4.6b}$$

which is a different from the experimentally measured frequencies Eqs. (4.4). Thus, the modeled potential is not sufficiently accurate for a quantitative *ab initio* comparison.[1] However, we qualitatively observe the dynamics of the experimental setup.

Figure 4.4 shows the evolution of the system for one trap cycle along the collision axis, as seen in experiment, and by our simulation. One obvious manifestation of the asymmetric potential, is that, the oscillation of the mother clouds is not symmetric about some center. The asymmetric effects are most readily seen in Fig. 4.5, where we focus on the second collision of the clouds. Before and after the second collision, the scattered atoms between the two mother clouds undergo a "mexican wave" like oscillation. That is, parts of the distribution of scattered atoms expand, while other parts collapse, in such a way, that a wave travels between the two mother clouds. This is a result of the trapping frequencies perpendicular to the collision axis, vary along the collision axis. In a harmonic trap, these outscattered atoms would expand and contract along the collision axis in a synchronized fashion. At the time of the collision, the oscillations of outscattered atoms are out of sync with the oscillations of the mother clouds, causing column densities to look like jet planes.

---

[1]This theoretical work was undertaken long after the experiment was decommissioned. Hence, it was not possible to better understand the source of the discrepancy. However, our results are sufficiently close, that, seeking quantitative agreement in future experiments seems possible.
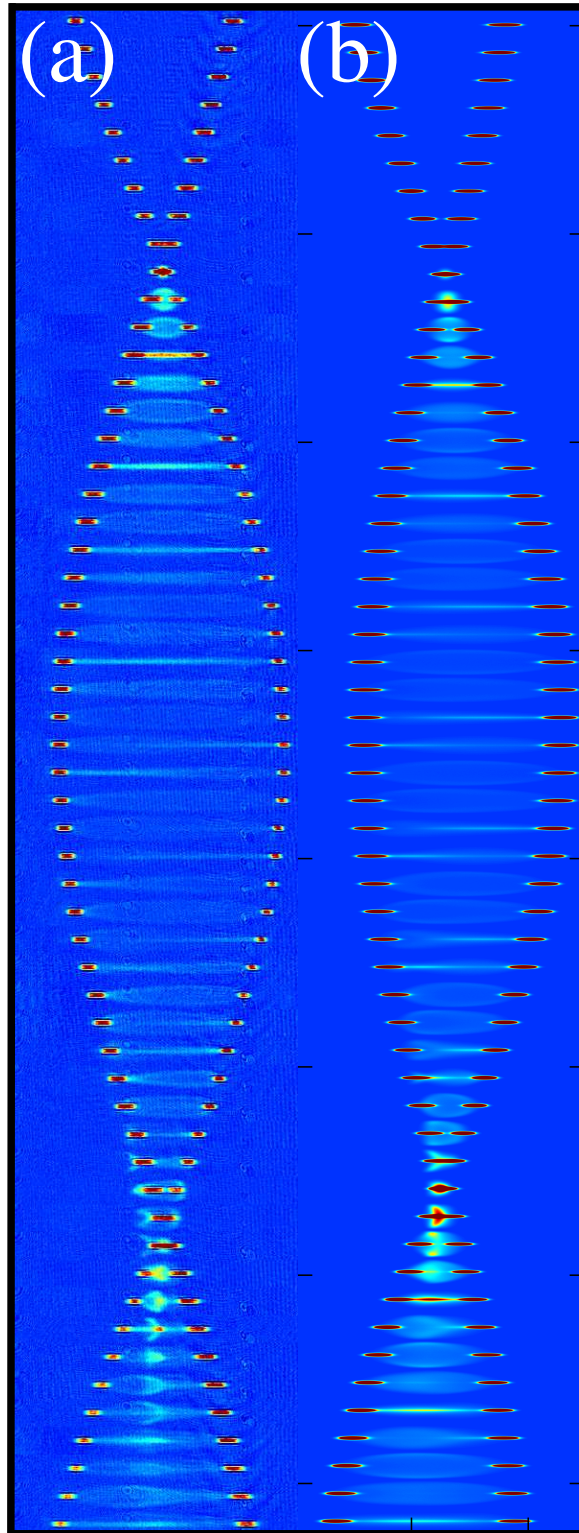
Figure 4.4: Column densities showing a comparison between the dynamics (a) reported in Ref. [33] and the dynamics (b) of a DSMC simulation using the modeled potential. Time increases in the downwards direction, and the time scale is approximately one full oscillation along the collision axis.
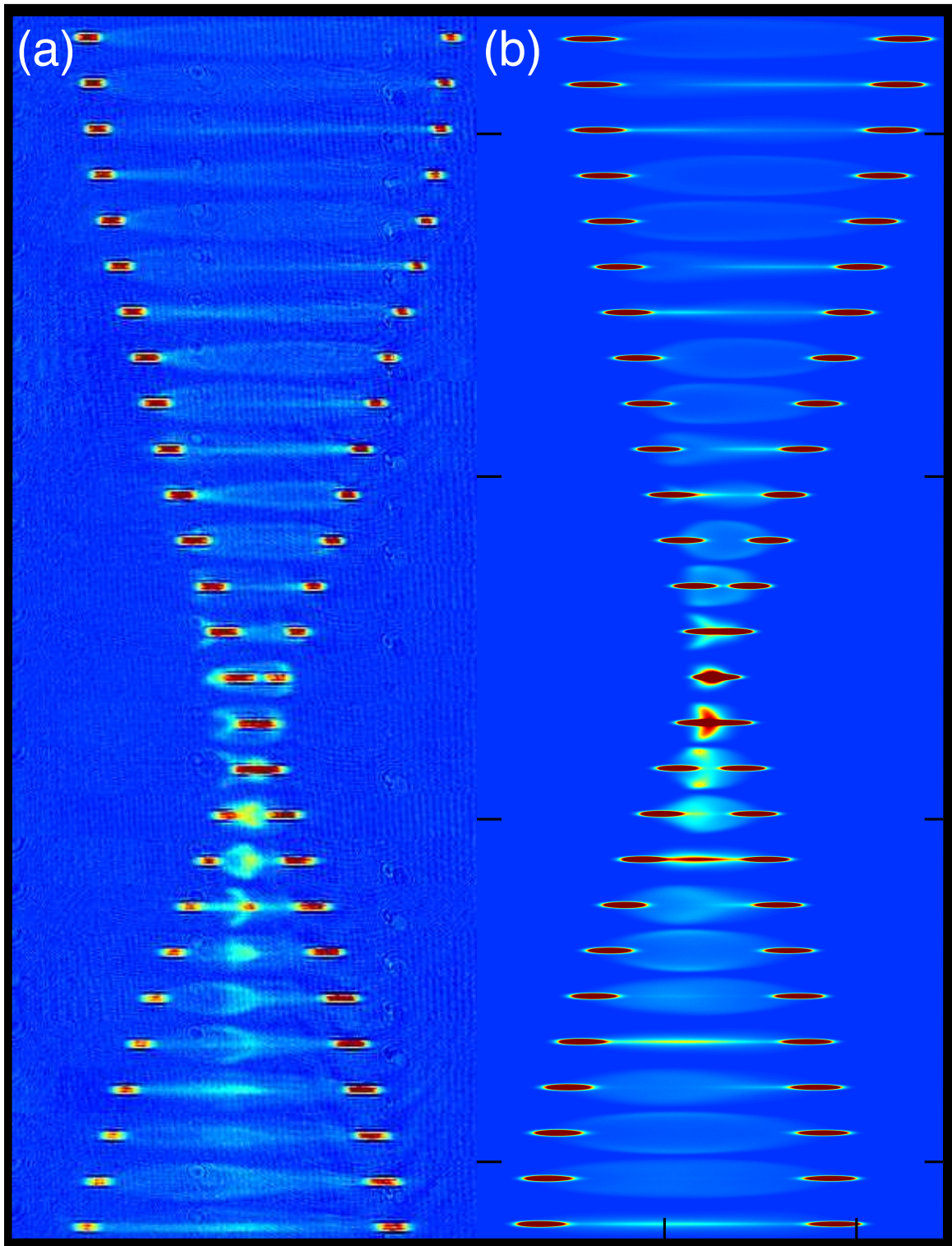
Figure 4.5: Column densities showing a comparison between the dynamics (a) reported in Ref. [33] and the dynamics (b) of a DSMC simulation using the modeled potential. Time increases in the downwards direction, and we focus on the second collision of the clouds in Fig. 4.4.

Simplified potential and initial conditions

Being restricted by the lack of a quantitative description of the potential, the problem is simplified by taking the potential to be the harmonic form given in Eq. (4.3) with the measured trapping frequencies Eqs. (4.4).

In this chapter, it is sufficient to use the equilibrium (Maxwell-Boltzmann) distribution function of a nondegenerate harmonically trapped gas as the initial conditions

$$f_{\text{eq}}\left(\mathbf{p}, \mathbf{r}\right) \equiv \mathcal{N}_{\text{P}} \left(\beta \hbar \omega\right)^3 \exp\left\{-\beta \left[\frac{p^2}{2m} + U(\mathbf{r})\right]\right\}, \qquad (4.7)$$

where $\beta = 1/k_{\text{B}}T$, and $\omega = (\omega_x \omega_y \omega_z)^{\frac{1}{3}}$. However, in Chapter 5, we seek a quantitative description for the experiment. To do this, the initial conditions are given by fitting the experimental images with gaussian distributions and assuming the momentum distributions are given by the Maxwell-Boltzmann distribution;

$$f_{\text{expt}}^i\left(\mathbf{p}, \mathbf{r}\right) = \frac{\mathcal{N}_{\text{P}}^i}{\left(\xi_{xy}^i\right)^2 \xi_z^i} \left(\frac{\hbar^2 \beta}{m}\right)^{\frac{3}{2}} \exp\left\{-\frac{1}{2}\left[\beta \frac{p^2}{m} + \frac{x^2 + y^2}{\left(\xi_{xy}^i\right)^2} + \frac{z^2}{\left(\xi_z^i\right)^2}\right]\right\}, \qquad (4.8)$$

where i indicates which cloud (i.e., cloud 1 or cloud 2), $\mathcal{N}_{\text{P}}^i$ is the number of physical atoms, and ξ_{xy}^i and ξ_z^i are the fitted standard deviations of the density.

The temperature used for the momentum distribution ($T = 225\,\text{nK}$) and the total number of atoms in the system ($\mathcal{N}_{\text{P}} = 4 \times 10^5$) are those of which are reported in Ref. [32]. The choices of $\mathcal{N}_{\text{P}}^i$, ξ_{xy}^i, and ξ_z^i are given in Sec. 5.4.1, where, to justify the description being quantitative, the initial conditions are discussed in detail.

4.1.3 Justification for Using the Classical Boltzmann Eqaution

The effect quantum statistics on collisions (Bose-stimulated or Pauli-blocked scattering) are negligible when $f \ll 1$. This is the case for this chapter, however, in Chapter 5, we will be considering distributions where $f\left(\mathbf{p}, \mathbf{r}, t\right) \sim 1/4$. This leads to an increase of $\sim 5\%$ to the total collision rate for collisions within a cloud. Although a small contribution already, the effects are insignificant, since the dynamics treated in Chapter 5 are of time scales, such that, less than 0.03 collisions per atom occur within the cloud. Thus, the intracollisions (i.e., collisions between atoms in the same cloud) can be treated classically.

For the scattering of atoms between the colliding clouds, many intercollisions occur. Therefore, we compare the phase-space density of one of the colliding clouds f_{cloud} to that of the scattered atoms f_{scat}. To obtain an upper bound, we assume that all atoms are scattered, and thus, they have density twice that of the density of the colliding cloud. In this

case, $f_{\text{cloud}}/f_{\text{scat}} \approx 2\Delta P_{\text{scat}}/\Delta P_{\text{cloud}}$, where ΔP_{cloud} and ΔP_{scat} are the momentum-space volumes which the cloud and the scattered atoms occupy, respectively. Figure 4.6 shows a qualitative depiction of the initial clouds and scattered atoms: the momentum widths of the cloud can be approximated by h/λ_{th}, where λ_{th} is the thermal de Broglie wavelength. The momentum-space volume of the scattered atoms can be approximated by $\pi p_{\text{coll}}^2 h/\lambda_{\text{th}}$, where $p_{\text{coll}}^2 = 4mk_{\text{B}}T_{\text{coll}}$ is the relative momentum of the clouds (πp_{coll}^2 is the surface area of the collision sphere). Thus, in terms of temperatures, $f_{\text{expt}}^i/f_{\text{scat}} = 4T_{\text{coll}}/T$. For the collisions we consider here, $T_{\text{coll}} \approx 1000T$, giving f_{scat} to be three orders of magnitude smaller than f_{expt}^i, hence, the intercollisions can also be treated classically.
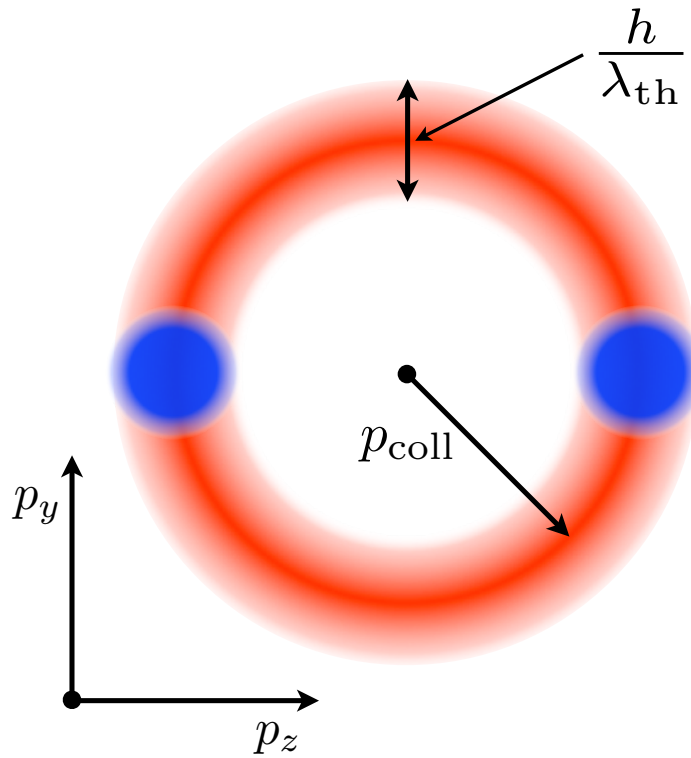
Figure 4.6: A qualitative depiction of the initial clouds (blue) and the scattered atoms (red) in the (p_y, p_z) plane.

4.2 Tests and Optimal Parameters for DSMC

In this section, we develop tests relevant to ultracold systems that we use to validate and to explore how to optimize the performance of the DSMC algorithm by quantifying the effects of the adaptive enhancements. Primarily, we are interested in the quality of the represen-

tation of the phase-space distribution, since this is of fundamental importance for accurate Boltzmann evolution. In particular, we address the effects of increasing the number of test particles, and refining the grid, on collision rates as compared to exact results.

4.2.1 Analytic Results

We develop benchmark analytic results to calibrate the algorithm against. To do this we consider the equilibrium (Maxwell-Boltzmann) distribution function for a harmonically trapped gas Eq. (4.7).

The total collision rate is given by

$$R = \frac{\sigma_0}{m} \int \frac{d^3p}{h^3} \int \frac{d^3p_1}{h^3} \int d^3r \, |\mathbf{p}_1 - \mathbf{p}| \, f f_1. \tag{4.9}$$

Here, we have taken the differential cross section to be velocity independent to give a total cross section of σ_0. Evaluating this expression for the equilibrium cloud, Eq. (4.7), we obtain

$$R_{\text{eq}} = \frac{\mathcal{N}_{\text{P}}^2}{2\pi^2} m\beta\omega^3\sigma_0. \tag{4.10}$$

As we are concerned with simulating the collisions of equilibrium clouds, it will be useful to consider the instantaneous distribution,

$$f_{\text{coll}}(\mathbf{p}, \mathbf{r}) = f_{\text{eq}}(\mathbf{p} + p_0\hat{\mathbf{z}}, \mathbf{r}) + f_{\text{eq}}(\mathbf{p} - p_0\hat{\mathbf{z}}, \mathbf{r}), \tag{4.11}$$

which corresponds to two spatially overlapping clouds with equilibrium shapes that are traveling with opposite momenta $\pm p_0$ along the z direction. The total collision rate for this case is

$$R_{\text{coll}} = \frac{\mathcal{N}_{\text{P}}^2}{2\pi^2} m\beta\omega^3\sigma_0 \left[2 + \exp\left(-p_0^2\frac{\beta}{m} \right) \right.$$
$$\left. + \frac{1}{2p_0}\sqrt{\frac{\pi m}{\beta}} \left(1 + 2p_0^2\frac{\beta}{m} \right) \text{erf}\left(p_0\sqrt{\frac{\beta}{m}} \right) \right]. \tag{4.12}$$

For small p_0, the term in the square brackets scales as $4 + \frac{2}{3}\beta p_0^2/m + O(p_0^4)$, showing that, for $p_0 = 0$, Eq. (4.12) reduces to Eq. (4.10) with $\mathcal{N}_{\text{P}} \to 2\mathcal{N}_{\text{P}}$, as expected. While for large p_0, it scales as $2 + \sqrt{\beta\pi/m}\,p_0 + O(p_0^{-1})$. The first term corresponds to the intra cloud collisions, while the linear term is obtained for the case of Dirac delta-function momentum distributions, $\delta(\mathbf{p} \pm p_0\hat{\mathbf{z}})$.

4.2.2   Grid Parameters and Test Particle Number

To investigate the accuracy with which collisions are treated, we compare the numerical collision rate to the exact values in Eqs. (4.10) and (4.12). To do this, we calculate the relative error of the numerical collision rate and examine its dependence on the number of test particles and grid refinement.[2]

Numerical Collision Rate

For the purpose of comparison, we need to extract a collision rate from the DSMC representation of $f(\mathbf{p}, \mathbf{r}, t)$. To do this, we evaluate the mean number of collisions in each cell over some time δt_c. Hence, in each cell, the mean collision rate per unit volume is

$$R_c \approx 2\alpha \sum_{(ij)}^{\tilde{M}_c} \frac{\tilde{P}_{ij}}{\Delta V_c \delta t_c}, \tag{4.13}$$

where (ij) indicates the indices of the $\tilde{M}_c$ selected collision pairs in the cell. Thus, the total collision rate for the system is

$$R = \sum_{\text{cells}} R_c \Delta V_c. \tag{4.14}$$

By calculating the collision rate in this way, we are, in effect, directly performing a Monte Carlo integration for the integral (4.9), which is the basis of the derivation of the collision probability in Ref. [18] (also see Sec. 6.1). The time step for the cell δt_c is somewhat arbitrary, and we choose it to give $\tilde{M}_c = \lfloor N_c/2 \rfloor$ collision pairs.

A convenient length scale for the trapped system is given by the thermal widths

$$W_i = \sqrt{2k_{\text{B}}T/m\omega_i^2}, \tag{4.15}$$

for the ith dimension, and we choose the master cell widths such that the resolution in each direction (relative to these widths) are the same, i.e.,

$$\gamma = \frac{\Delta x}{W_x} = \frac{\Delta y}{W_y} = \frac{\Delta z}{W_z}. \tag{4.16}$$

In what follows, γ will serve as an important parameter to specify the fineness of the spatial resolution.

---

[2]The relative error in the collision rate is independent of $\mathcal{N}_{\text{P}}$ and σ_0.

Accuracy

To increase the accuracy of our numerical calculation of the total collision rate, we must improve the accuracy of our representation of continuous distribution $f(\mathbf{p}, \mathbf{r}, t)$ or take more samples. In the DSMC algorithm, $f(\mathbf{p}, \mathbf{r}, t)$ is represented in two ways: (i) the test-particle swarm, (ii) the grid of cells that sample the test-particle swarm. In Sec. 3.3.3, the discussion for the number of tested collisions shows that, without cell adaption [i.e., LACs or LATSs], (i) and (ii) are largely decoupled. However, simply decreasing the size of the master cells can cause large statistical fluctuations in the number of collisions, as single occupation of a cell becomes more common, hence, requiring a larger number of samples.

Our LAC scheme essentially establishes a local maximum size of the cells (i.e., maximum error), which is set by $\mathcal{N}_\mathrm{T}$, N_th, and $n(\mathbf{r}, t)$. In our results, this is seen for the collision rate of the equilibrium cloud given in Fig. 4.7. These results show that the magnitude of the relative error does not continue to increase with increasing γ (as it does in the unadapted case), but tends to a constant dependent on N_th. With decreasing N_th, smaller cell sizes are achieved, hence, lower error.[3] However, we restrict ourselves to $N_\mathrm{th} \geq 2$ to avoid the increasingly large statistical fluctuations mentioned earlier. The results in Fig. 4.7 remain qualitatively similar for different values of $\mathcal{N}_\mathrm{T}$, however, the fluctuations (i.e., error bars Fig. 4.7) increase with decreasing test-particle number.

It is worth noting that systems with identical density distributions are coarse grained in the same fashion (provided $\mathcal{N}_\mathrm{T}$ is the same when using the LAC scheme), hence, they have the same accuracy. For example, the equilibrium (4.7) and collision (4.11) distributions have identical relative error profiles as seen in Fig. 4.7. However, if a system is dynamically changing and no adaption was employed, evolving to a more dilute system would decrease the magnitude of the relative error, while increasing if becoming denser. For adaptive schemes, this is not an issue, as the cell sizes automatically adjust to this change.

Performance Considerations

The results in Fig. 4.7 show that the following cases approximately have the same relative error in collision rate:

(i) **SIM1:** An unadaptive simulation with $\gamma = 0.02$.

---

[3]Care needs to be taken with other adaptive schemes, since the approach outlined in Sec. 3.3.3, to remove statistical biasing, neglects to take into account statistical fluctuations from other sources (e.g., cell volume), which may become important [66].
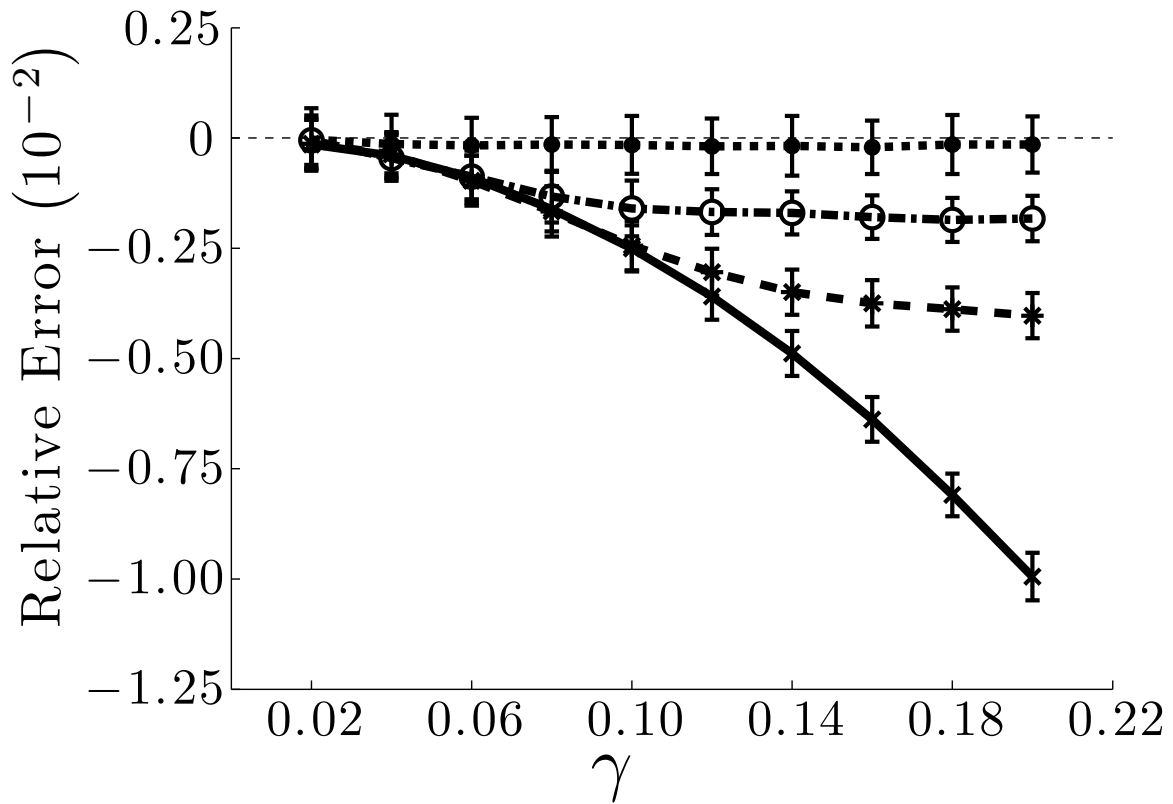
Figure 4.7: The relative error of the total collision rate, Eq. (4.10), for the equilibrium distribution $f_{eq}(\mathbf{p}, \mathbf{r})$ against γ with $\mathcal{N}_T = 10^7$ is shown for the cases without (solid line) and with cell adaption where $N_{th} = 2$ (dotted line), 150 (dashed-dotted line), and 500 (dashed line). The results shown here are averaged over 200 initial conditions, while the error bars give the standard deviation. Without adaption, the error increases with increasing γ, since $f_{eq}(\mathbf{p}, \mathbf{r})$ becomes more coarsely grained. However, with the inclusion of adaption, this behavior is combatted as the LAC subcells adapt accordingly. We obtain the initial conditions for the test particles from $f_{eq}(\mathbf{p}, \mathbf{r})$ using the Monte Carlo acceptance-rejection method. System parameters: The harmonic potential is chosen to be the same as that used in the ultra cold collider experiment with $\omega_x = \omega_y = 2\pi \times 155\,\mathrm{Hz}$ and $\omega_z = 2\pi \times 12\,\mathrm{Hz}$, $\mathcal{N}_P = 2 \times 10^5$ and $T = 600\,\mathrm{nK}$.

(ii) **SIM2:** A LAC simulation with $N_{th} = 2$ and $\gamma = 0.2$, which we also include LATSs for dynamics.

A fuller picture of the merits of using either of these approaches for a simulation requires us to understand their resource requirements.

Speed: We find that, with our code SIM2 is approximately five times faster than SIM1 for near-equilibrium evolution. Note, we only use the LATS scheme in SIM2 for the master cells (as discussed at the end of Sec. 3.3.4). It should also be noted that this performance indicator is dependent on the code implementation and physical problem under consideration (i.e., equilibrium cloud versus highly nonequilibrium situation).

Storage: SIM1 requires $\sim 5 \times 10^7$ master cells, while SIM2 requires $\sim 5 \times 10^4$ master cells with a maximum of 4096 LAC subcells within a master cell (typically requiring a total of $\sim 7 \times 10^6$ LAC subcells).

4.2.3 Collisions Between Clouds: Comparison to Simple Methods

In this subsection, we consider the collision of two equilibrium clouds in a harmonic trap, $f_{\text{eq}}\left(\mathbf{p} \pm p_0\hat{\mathbf{z}}, \mathbf{r} \mp r_0\hat{\mathbf{z}}\right)$, shown schematically in Fig. 4.8. We study this collision using our DSMC algorithm and compare its results to a simplified model that has been used previously to analyze this problem. Initially, the two clouds are centered at locations separated by a distance of $2r_0$ along the z direction, chosen to ensure that (initially) the clouds do not overlap. The clouds approach each other, moving at a relative momentum of $2p_0$, and when they overlap, collisions scatter atoms out of the clouds. Here, our main interest is the total number of such scattered atoms $\mathcal{N}_{\text{sc}}$, after the two clouds have completed passing through each other.

The simple model we consider was used in Ref. [32] (see also, Ref. [67]) and was derived from the BE description of the colliding clouds by making the following approximations:

(**a1**) The harmonic potential is ignored (collision taken to be in free space).

(**a2**) The momentum distribution of each cloud is replaced by $\delta\left(\mathbf{p} \pm p_0\hat{\mathbf{z}}\right)$.

(**a3**) The dynamics of scattered atoms are neglected.

These approximations lead to equations for the densities $n_i\left(\mathbf{r}, t\right)$ of cloud $i = a, b$,

$$\left(\frac{\partial}{\partial t} \pm \frac{v_{\text{r}}}{2}\frac{\partial}{\partial z}\right) n_i\left(\mathbf{r}, t\right) = -v_{\text{r}}\sigma_0 n_a\left(\mathbf{r}, t\right) n_b\left(\mathbf{r}, t\right), \tag{4.17}$$

where $v_{\text{r}} = 2p_0/m$. We can solve these equations directly using a pseudo-spectral method.
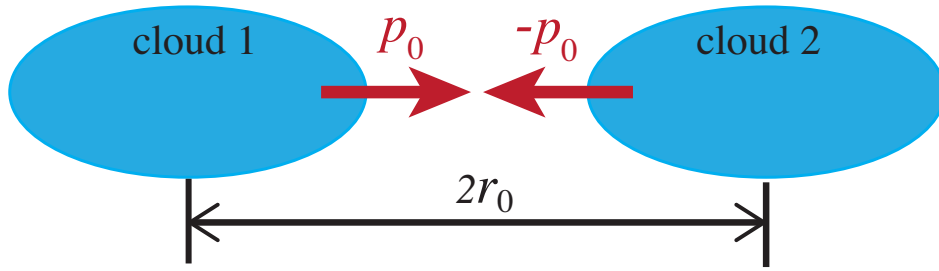
Figure 4.8: A schematic of the ultra-cold-atom collider used in Sec. 4.3. Two clouds initially separated by a distance of $2r_0$ collide at a relative momentum of $2p_0$. The number of atoms that have scattered out of the clouds, after they have passed through each other, is referred to as $\mathcal{N}_{\mathrm{sc}}$.

An analytic expression may be derived with an additional approximation:

(a4) The loss of atoms is small enough such that the shape of the densities do not deform but remain Gaussian while the normalization of each cloud $\mathcal{N}_{\mathrm{P}}$ decreases.

Using this, one can integrate Eq. (4.17) over all position space to find the total number of scattered atoms from the collision,

$$\mathcal{N}_{\mathrm{sc}} = \frac{\mathcal{N}_{\mathrm{P}}^2}{4\pi} m\beta\omega_x\omega_y\sigma_0. \tag{4.18}$$

As shown in Sec. 4.2.1, when considering the limiting behavior of Eq. (4.12), the approximation (a2) is satisfied when $T_{\mathrm{coll}} \gg T$ (which is the case for collider velocities we consider here). That the momentum distributions can be replaced with Dirac δ functions is consistent with the quantum statistics not playing a significant role in the scattering that occurs when the two clouds collide. However, the internal motion of each cloud can be influenced by quantum statistics.

As the full DSMC solution includes the dynamics of scattered atoms, it is useful to split the scattered atoms into two groups: (i) scattered atoms that have not undergone any subsequent collisions, (ii) scattered atoms that have undergone additional collisions, including all collision partners.[4] All of the scattered atoms predicted by Eqs. (4.17) and (4.18) are of group (i).

In Eqs. (4.17) and (4.18), $\mathcal{N}_{\mathrm{sc}}$ is independent of the details of the differential cross section (only depending on the total cross section), and this is largely true for the full solution in the

---

[4]We include atoms that are scattered out of cloud 1 or 2 by a collision with an already scattered atom.
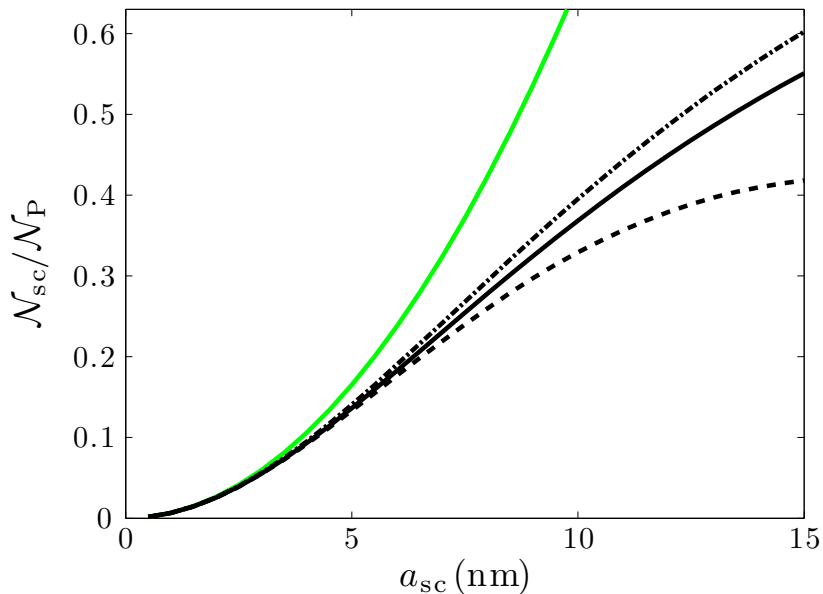
Figure 4.9: The fraction of scattered atoms due to the collision of two equilibrium clouds as a function of $a_{\rm sc}$. Equation (4.18) [solid green line] has poor agreement with the solution of Eq. (4.17) (solid black line) for $\mathcal{N}_{\rm sc}/\mathcal{N}_{\rm P} > 0.05$, since approximation (a4) is no longer valid. Group (i) scattered atoms (dashed black line) and total scattered atoms [groups (i) and (ii)] (dashed-dotted black line) from the DSMC solution. The system parameters are given in Fig. 4.7, and for the DSMC simulation, $\gamma = 0.2$, $\mathcal{N}_{\rm T} = 10^7$, and $N_{\rm th} = 2$. The standard deviation error is not shown as it is on the order of the line width.

case considered here. Thus, it is convenient to take $\sigma_0 = 8\pi a_{\rm sc}^2$, which is of the form of the total cross section for *s*-wave scattering in the low-collision energy limit with scattering length $a_{\rm sc}$ (see Sec. 2.2). Additionally, $\mathcal{N}_{\rm sc}$ in both equations is independent of $v_{\rm r}$, i.e., $T_{\rm coll}$. However, this is not the case for the full solution, since the collision occurs in a trap. For example, if the radial confinement is tight, then a scattered atom can oscillate out and back in the radial plane and can recollide (depending on the timescale over which the collision proceeds). Here, we choose to operate in a regime where these effects are small and the simple model should accurately describe the full solution. To do this, we choose parameters such that $T_{\rm coll} = 300\,\mu{\rm K}$,[5] giving a short time scale for the collision.

The results of Eqs. (4.17) and (4.18), as well as the full solution, are shown in Fig. 4.9

---

[5]For the full DSMC solution, the clouds accelerate as they approach the trap center, and we take the value of p_0 that they obtain at the trap center as the value to compare against the simple model.

for varying a_{sc}. All models agree well in the low scattering regime $\mathcal{N}_{\mathrm{sc}}/\mathcal{N}_{\mathrm{P}} < 0.05$, while for higher scattering fractions, approximation (a4) becomes invalid, and the dynamics of the scattered atoms becomes increasingly important. However, the solution of Eq. (4.17) agrees to within 10% of the relative error to the total [groups (i) and (ii) combined] scattered fraction given by the full solution over the whole range.

We can modify the collision problem and DSMC method to a regime that is exactly described by the simplified equation (4.17). To do this, all particles are taken to have momentum $\pm p_0$ along the z axis (the components of momenta in the xy plane are zero) and evolve without an external trapping potential. Consistent with the approximations going into Eq. (4.17), whenever a pair of particles undergoes a collision, it is removed from the system (eliminating any need for consideration of multiple collisions). Due to the form of the distribution function, NNCs cannot be used.[6]

The relative error of $\mathcal{N}_{\mathrm{sc}}$ as calculated by the DSMC solution to that of our numerical solution of Eq. (4.17) is shown in Fig. 4.10 for the two cases $\mathcal{N}_{\mathrm{T}} = 10^5$ and 10^7. The excellent agreement of the two results is a good test that the DSMC method is correctly implemented. The error bars represent the statistical fluctuations of the DSMC results. These fluctuations reduce with increasing a_{sc} as $\mathcal{N}_{\mathrm{sc}}$ increases, while between the two cases, they are reduced by a factor of 10, since they also decrease with increasing $\mathcal{N}_{\mathrm{T}}$ (to be definite, these fluctuations are given by the inverse square root of the number of scattered test particles).

---

[6]Particles have no transverse momenta, thus particles from the same cloud never leave the proximity of each other. Hence, it is required that a particle from one cloud is closest to a particle from the other cloud before a collision can occur, which results in a decreased number of collisions.
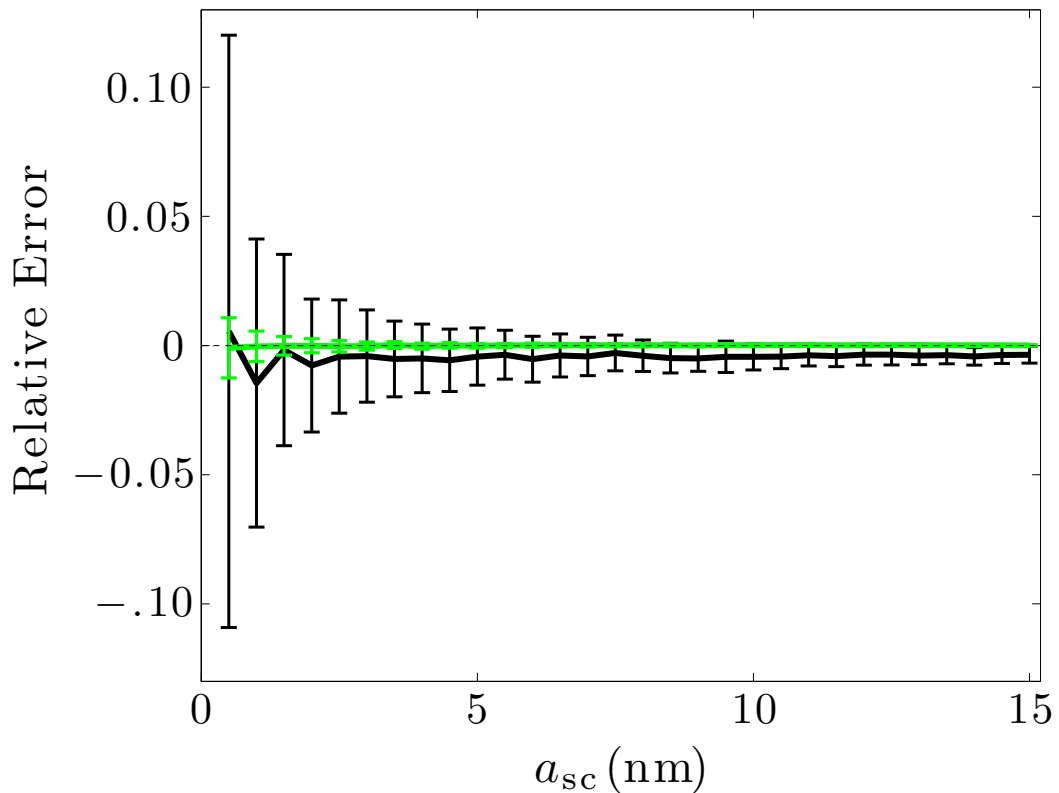
Figure 4.10: The relative error of $\mathcal{N}_{sc}$ as calculated by the DSMC solution of Eq. (4.17) [see text] to that of our pseudo spectral solution of Eq. (4.17). Here, we show the two cases $\mathcal{N}_T = 10^5$ (black) and 10^7 [green] with $\gamma = 0.2$, $N_{th} = 25$, and the system parameters given in Fig. 4.7. We use $\eta_{coll} = \eta_{tr} = 0.01$, and $\eta_{max} = 0.1$. The results shown here are averaged over 200 simulations, while the error bars give the standard deviation.

4.3 Many-body simulation of an ultra-cold-atom collider

In this section, we demonstrate the application of our DSMC algorithm to the simulation of the ultra-cold-atom collider reported in Ref. [32]. The main extension, over the DSMC collision test presented in Sec. 4.2.3, is the inclusion of the full two-body collisional cross section needed for a realistic microscopic description of the collisional interactions. We then extend our consideration to the long-time dynamics of the collider and how the system progresses to equilibrium.

4.3.1 DSMC simulations

Using the full energy and angular-dependent-scattering cross section, we present the results of column densities calculated after two equilibrium clouds $f_{\text{eq}}\left(\mathbf{p} \pm p_0\hat{\mathbf{z}}, \mathbf{r} \mp r_0\hat{\mathbf{z}}\right)$ have collided for the cases $T_{\text{coll}} = 200\,\mu\text{K}$ and $300\,\mu\text{K}$. Following the experimental procedure [32], we calculate these column densities at a quarter of the radial trap period ($\pi/2\omega_x$) after the clouds reach the center of the trap. At this time the bulk of the scattered atoms reach their maximal extent in the radial direction. Figures 4.11(a) and 4.11(c) show a regime of *s*- and *d*-wave interference ($T_{\text{coll}} = 200\,\mu\text{K}$), while Figs. 4.11(b) and 4.11(d) show a *d*-wave regime ($T_{\text{coll}} = 300\,\mu\text{K}$). Clearly, the distribution of scattered atoms deviates from the typical *s*-wave halo (e.g., see Ref. [68]).

4.3.2 Long-time dynamics: Rethermalization

The idea of using rethermalization of colliding condensates to perform calorimetry has been proposed in Ref. [69], however, no direct simulations were made of the thermalization dynamics. More generally, there has been significant recent interest in how a quantum system rethermalizes [70], particularly in systems that might be experimentally realized with ultra-cold-atomic gases (e.g., see Refs. [71, 72]). To date, much of the attention has focused on integrable or nearly integrable systems where numerical solutions are available for small samples of atoms (typically $\mathcal{N}_{\text{P}} < 10^2$). However, in such regimes, thermalization is often inhibited or is strongly affected by constraints (e.g., see Ref. [73]) as well as being difficult to explore experimentally due to the small atom number (or requiring many similarly prepared systems to get a good signal).

Thus, we are motivated to apply the DSMC method to model the dynamics of colliding ultracold clouds well past the first collision. As the collisions occur in the trap, the clouds will oscillate back and forth, recolliding each time, and thus, are provided with the opportunity
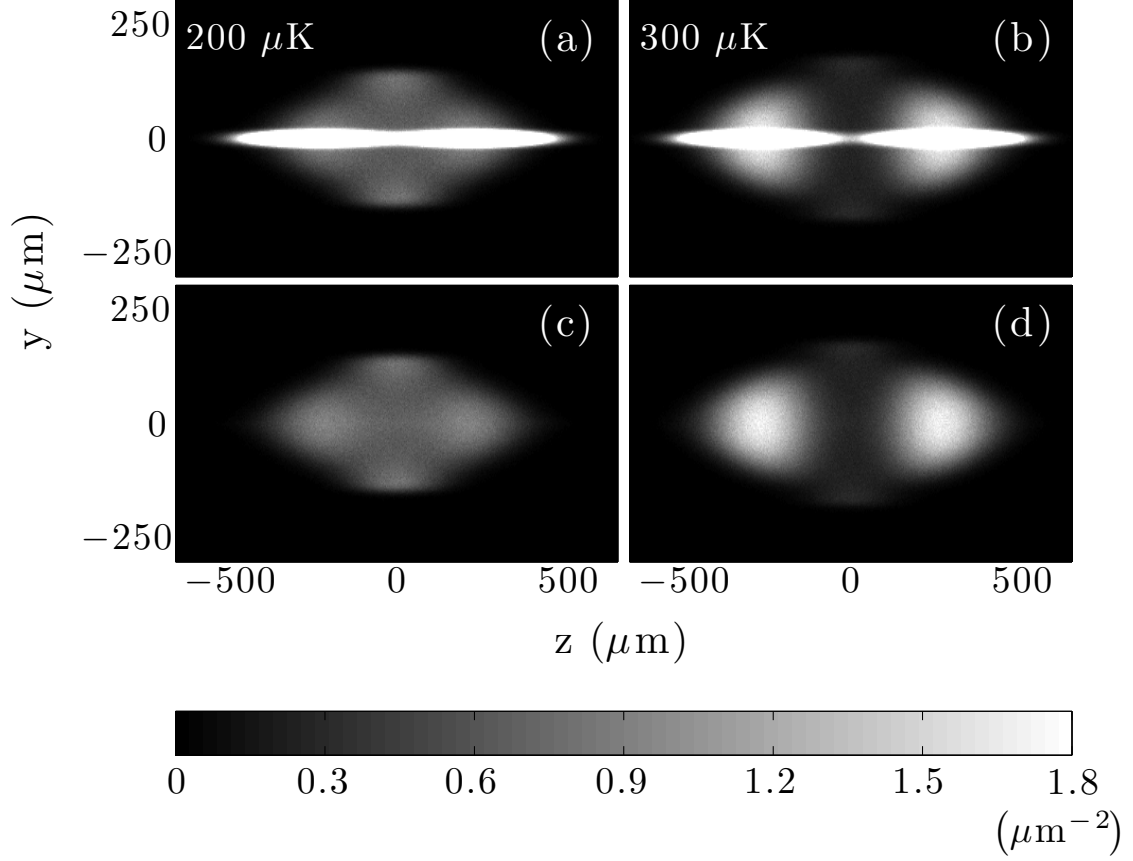
Figure 4.11: Column densities at time $\pi/2\omega_x$ after the clouds reach the center of the trap. $T_{\text{coll}} = 200\,\mu\text{K}$ [(a) and (c)] is a regime of s- and d-wave interference, while $T_{\text{coll}} = 300\,\mu\text{K}$ [(b) and (d)] is a d-wave regime. (c) and (d) only show the scattered atoms. The initial conditions for the clouds are chosen as in Sec. 4.2.3, and the system parameters are given in Fig. 4.7, while the simulation parameters are $\gamma = 0.2$, $\mathcal{N}_{\text{T}} = 10^5$, and $N_{\text{th}} = 2$. The results were averaged over 200 simulations. Note, we have compared these results to simulations with $\mathcal{N}_{\text{T}} = 10^7$ also averaged over 200 runs, and we find that the number of scattered particles and the angular scattering distributions agreed to within 1%.

to rethermalize. This system is much larger and classical in nature than the small quantum systems generically considered for thermalization studies. However, we believe this is an interesting system: first as a bridge between quantum and classical thermalization in ultracold gases that is practical for experimental investigation. Second, such a system might provide a unique opportunity to test the BE in a regime where the microscopic parameters are precisely known and with well-characterized far-from-equilibrium initial conditions. Few equations in theoretical physics have evoked as much discussion and controversy as the BE – particularly in reference to the introduction of irreversibility – and such a test could be of broad interest and shed light on some long-standing issues in statistical mechanics.

Our first evidence for thermalization comes from examining the density profiles of the colliding clouds at times after the first collision. Some examples of these density profiles are shown in Figs. 4.12(a)-4.12(d) and reveal that, as time passes, the number of atoms participating in the parametric oscillation of the mother clouds along the z axis decreases as the collisions convert the system to a more isotropic form. Indeed, the system clearly appears to increase entropy and approaches an equilibrium like configuration.

In order to quantify the approach to equilibrium, it is useful to consider how various moments of the system evolve dynamically. In Fig. 4.13, we show the envelope of the oscillations in the position spread moment $\langle r^2 \rangle^{1/2} = \langle x^2 + y^2 + z^2 \rangle^{1/2}$, characterizing the root-mean square of the distance of the particles from the trap center. [Note the oscillations of this moment occur on a much faster timescale and are shown in an inset to Fig. 4.13.] These results show that the system rethermalizes quite rapidly over the first approximately five trap periods. The number of collisions per particle over the first approximately three trap periods is shown in the inset to Fig. 4.13. The steps in collision number, which are initially apparent, arise from the periodic recolliding of the clouds. However, as the system is distributed over modes, these steps smooth out. These results show that, during this initial rapid phase of rethermalization, atoms experience $\gtrsim 10$ collisions, much greater than the value of 2.7 often quoted in the literature from the study of Wu and Foot [13].

After this rapid thermalization phase, the relaxation to equilibrium proceeds more slowly as energy contained within a few low-frequency collective modes waits to be damped. We find that two modes are dominant on long time scales. Most importantly, a mode that oscillates at $2\omega_x (= 2\omega_y)$ is dominated by radial breathing character and is well described (both frequency and damping) by the analytic predictions given in Ref. [12].[7] Also, we note that the rate of relaxation is strongly dependent on the trapping geometry and collision rate. The analytical predictions are only applicable when the system is near the final equilibrium state,

---

[7] Calculations based on these analytic prediction were performed by Danny Baillie.
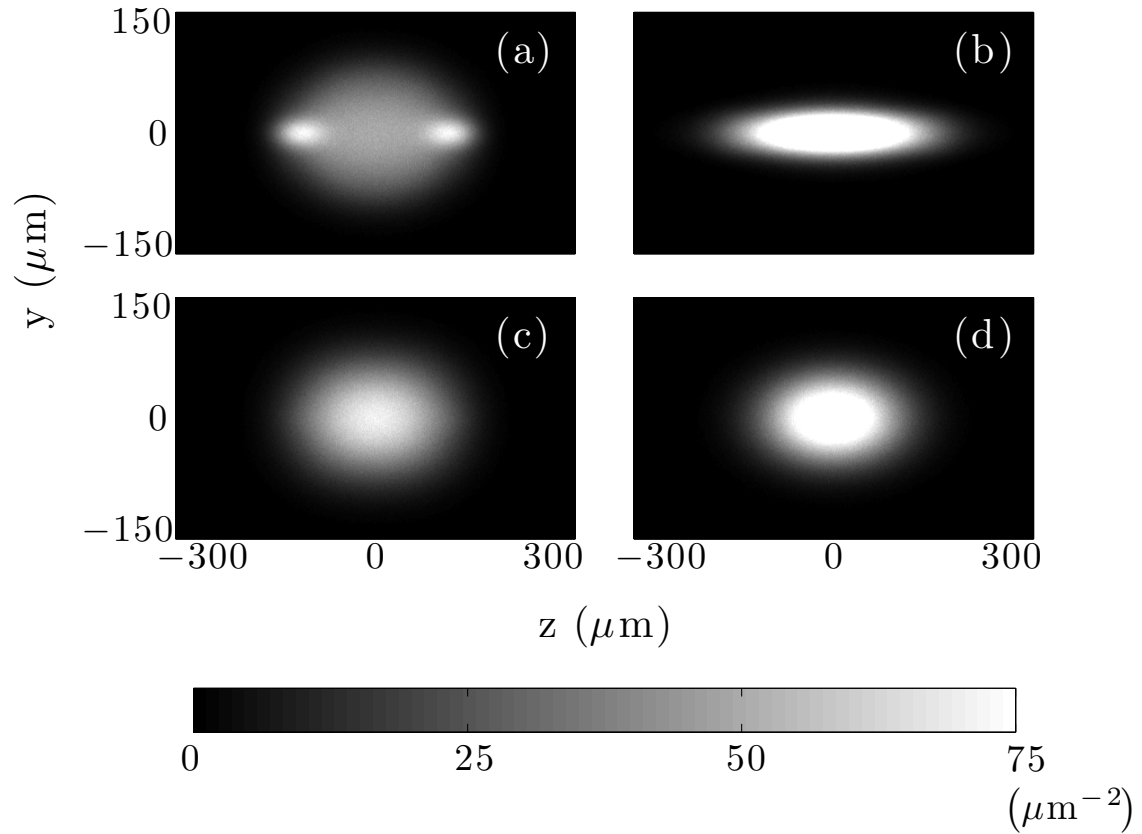
Figure 4.12: Column densities illustrating the long time dynamics of rethermalization. (a) At time $t\omega_z = 7.04$ after the clouds have passed through each other twice. The colliding clouds are still visible (density peaks). When the colliding clouds are depleted, the system continues to evolve through collective oscillations that are illustrated by the images (b) and (c) at $t\omega_z = 18.85$ and 19.60, respectively. The decay of these collective oscillations occurs on a slower time scale than the depletion of the colliding clouds, and the distribution does not take on the equilibrium distribution until much later times as seen in (d) at $t\omega_z = 500.02$. The trap frequencies are $\omega_z = 2\pi \times 50\,\text{Hz}$ and $\omega_x = \omega_y = 2\omega_z$, and each of the initial clouds has $\mathcal{N}_{\text{P}} = 10^6$ and $T = 600\,\text{nK}$. We use an isotropic differential cross section with $a_{\text{sc}} = 10$ nm. The initial separation is chosen such that there is insignificant overlap of the clouds. The momenta are chosen to give $T_{\text{coll}} = 32.4\,\mu\text{K}$, giving a final equilibrium temperature of $T = 6\,\mu\text{K}$. Note, for an isotropic trap, the system does not completely thermalize without mean-field effects, since the breathing mode does not damp [12].
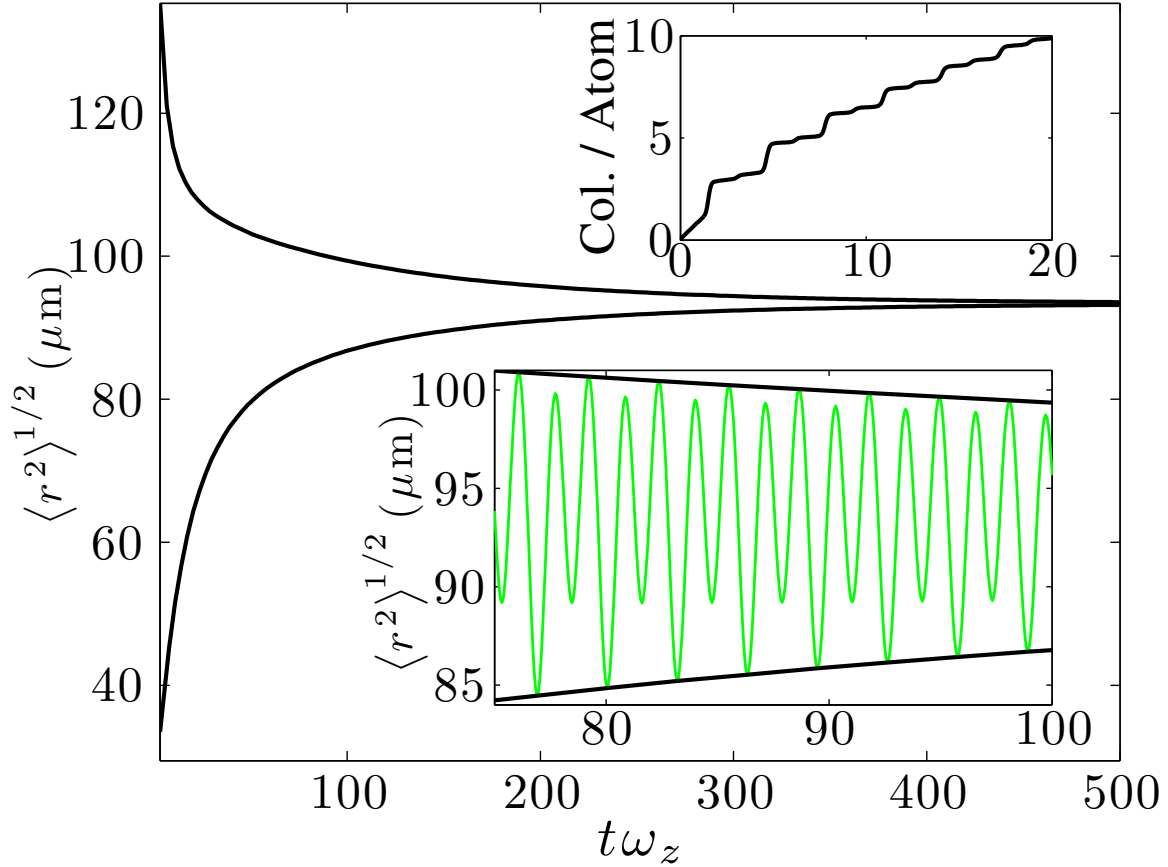
Figure 4.13: Envelope of the oscillations (as seen in the lower inset) of the root-mean-square of r. The rapid decay of the envelope within the first ten trap cycles is attributed to the depletion of the colliding clouds, while the slower decay is the decay of the collective modes. The upper inset shows the mean number of collisions per atom.

as they use the Gaussian anstaz

$$f\left(\mathbf{p}, \mathbf{r}, t\right) = \frac{\mathcal{N}_{\mathrm{P}}\hbar^3}{\xi_{xy}^2 \xi_z \zeta_{xy}^2 \zeta_z} \exp\left[-\frac{1}{2}\left(\frac{p_x^2 + p_y^2}{\zeta_{xy}^2} + \frac{p_z^2}{\zeta_z^2} + \frac{x^2 + y^2}{\xi_{xy}^2} + \frac{z^2}{\xi_z^2}\right)\right], \qquad (4.19)$$

where the standard deviations hold the time dependence.

In relation to thermalization dynamics, it is interesting to revisit the role of test particles in the DSMC simulation. In general, increasing $\mathcal{N}_{\mathrm{T}}$ has the effect of reducing fluctuations in a simulation and, hence, the number of trajectories needed to obtain an ensemble average. However, in order to gain a better understanding of typical results (and, hence, fluctuations) that might be expected in experiments, it is necessary to take $\mathcal{N}_{\mathrm{T}} = \mathcal{N}_{\mathrm{P}}$. To illustrate this, we show some results for a small amplitude collective-mode oscillation in Fig. 4.14 for

a system with $\mathcal{N}_P = 10^4$ and various numbers of test particles. As the number of test particles increases, the results become increasingly indistinguishable from the ensemble-averaged results. However, for $\mathcal{N}_T = \mathcal{N}_P$, the individual trajectory deviates significantly.

We emphasize that our simulations for thermalization in this section have been performed for the case of purely *s*-wave scattering. A detailed study of thermalization, including higher-order partial waves (e.g., as the collision energy is scanned across the *d*-wave resonance), would be needed for detailed comparison with experiments in this area but is beyond the scope of this thesis. Along these lines, we would like to note an interesting interplay between the partial waves that has been shown in the study of the thermalization of mixtures by Anderlini and Guéry-Odelin [74]. In that thesis, they performed an analytical study of near-equilibrium thermalization of a two-component mixture and showed that the thermalization time (unlike the collision rate) depended on the interference between the scattering partial waves.
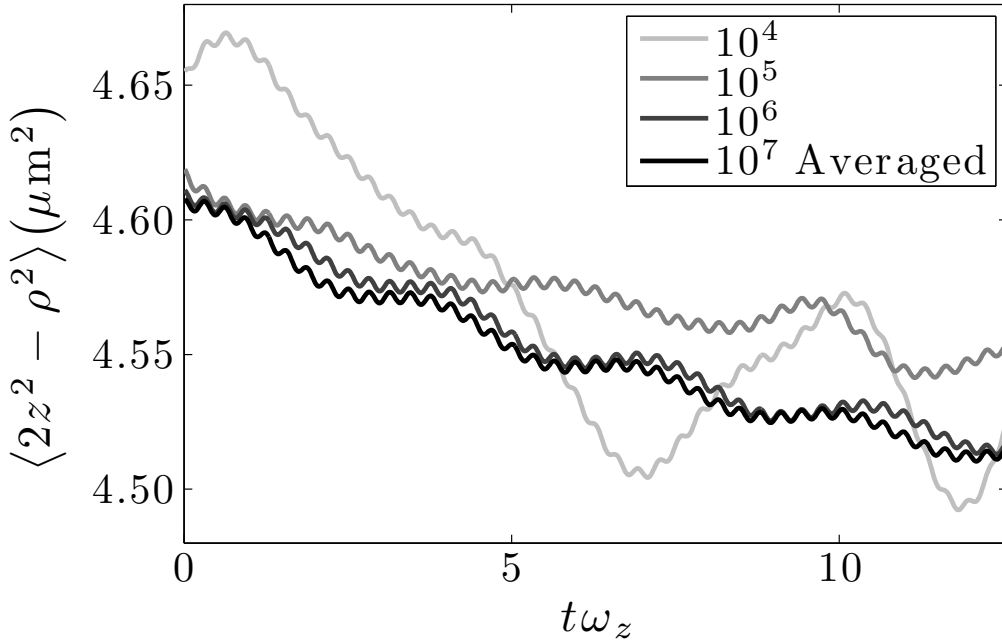
Figure 4.14: Collective oscillation induced by a small contraction of the radial trap confinement for a system with $\omega_z = 2\pi \times 50\,\mathrm{Hz}$, $\omega_x = \omega_y = 10\omega_z$, $\mathcal{N}_P = 10^4$, and $T = 600\,\mathrm{nK}$. The legend gives $\mathcal{N}_T$ used, and as this increases, the results for a single run become increasingly indistinguishable from the ensemble-averaged result for $\mathcal{N}_T = 10^7$.

Chapter 5

Comparison to the Ultracold-Atomic Collider Experiment

The partial-wave phase shifts completely characterize the two-body interactions between atoms, and having an accurate description of these is fundamentally important to describing ultracold atomic systems. The theoretical model of these phase shifts uses potentials that rely on experimental results for their optimization. The ultracold-atomic collider [32] was developed with the motivation to measure the phase shifts of atoms, in particular, their collision energy dependence. We quantify the development, since the experiment to current day, of the theoretical predictions of the *s*- and *d*-wave phase shifts for ^{87}Rb, in Sec. 5.1.

In the collider experiments [33, 34, 75], the phase shifts were measured by fitting the differential cross section to the angular scattering probability $P(\theta)$, where $P(\theta)\,d\theta$ gives the probability that an atom will scatter between θ and $\theta + d\theta$. However, in Sec. 5.4.2, we establish for this particular collider, the many-body effects are significantly large that this two-body method cannot be applied. Thus, we are motivated to employ our DSMC algorithm to: (i) establish the level of agreement between the experiment [32] and the theoretical models (Sec. 5.4.1); (ii) give a quantitative measure the phase shifts (Sec. 5.4.3).

5.1   Theoretical Calculations of ^{87}Rb Phase Shifts

A complete description of the two-body interactions between atoms is not currently possible through *ab initio* calculations. Instead, informed by numerous photo-association, Feshbach spectroscopy, and other experiments, collision theorists have been able to infer many properties of the inter-atomic potentials to various degrees of accuracy.

For the purposes of understanding the ultracold collider experiment, we need to have

a model for the interactions at low, but finite, collision energy. Such a description can be furnished by knowledge of the first few partial-wave phase shifts as a function of energy (see Sec. 2.2), in particular, the *s*- and *d*-wave shifts. Calculations of these were made Paul Julienne, of the National Institute of Standards in Gaithersburg, Maryland, in 2004 [32]. These calculations were based on a coupled-channels model that includes the ground state singlet and triplet potentials, and all spin-dependent interactions. These used the, at the time, state of the art values for the triplet potential: van der Waals C_6 constant of 4707 atomic units (1 atomic unit $= 9.5734 \times 10^{-26}\,\mathrm{J\,nm^6}$), and a scattering length of 98.96 atomic units (1 atomic unit $= 0.052918\,\mathrm{nm}$) [76].

In 2010, two-photon dark-state spectroscopy experiments, and associated theory, claim to have further refined the ^{87}Rb potentials [77]. Using these potentials, Eite Tiesinga, of the National Institute of Standards in Gaithersburg, Maryland, has recalculated the *s*- and *d*-wave phase shifts. These results are compared to the original Julienne calculations [32] in Fig. 5.1. The difference of the *s*-wave properties in these two calculations is very small ($\approx 0.1\%$ relative difference in the phase shift at a given T_{coll}). However, the *d*-wave phase shifts are more significantly changed, with the new results shifting the location of the resonance down by $5 - 10\,\mu\mathrm{K}$.

5.2 Method of Analysis

Here, we discus how the angular scattering distribution is extracted from experiment and simulation. We also detail how the angular scattering distribution is used to determine the DSMC simulations which give best agreement to the experimental data.

5.2.1 Determining the Angular Scattering Distribution

The angular scattering probability is extracted from the experimental images using the methods given in Ref. [33], which includes the dynamics of the scattered atoms in the trap (see Fig. 5.2). This forms the central observable that we use to fit the many-body simulations to the experimental data. The process is shown in Fig. 5.3, where the experimental absorption images are converted to column densities, then, these are converted to the three-dimensional densities by performing an inverse-Abel transform, which exploits the cylindrical symmetry of the system. The scattered atoms are isolated in a simple manner, from which, $P(\theta)$ is obtained by binning the density into cells of size $\pi/32$ rads, along the θ coordinate.[1]

---

[1]The Cloud in a Cell interpolation scheme [78] is used.
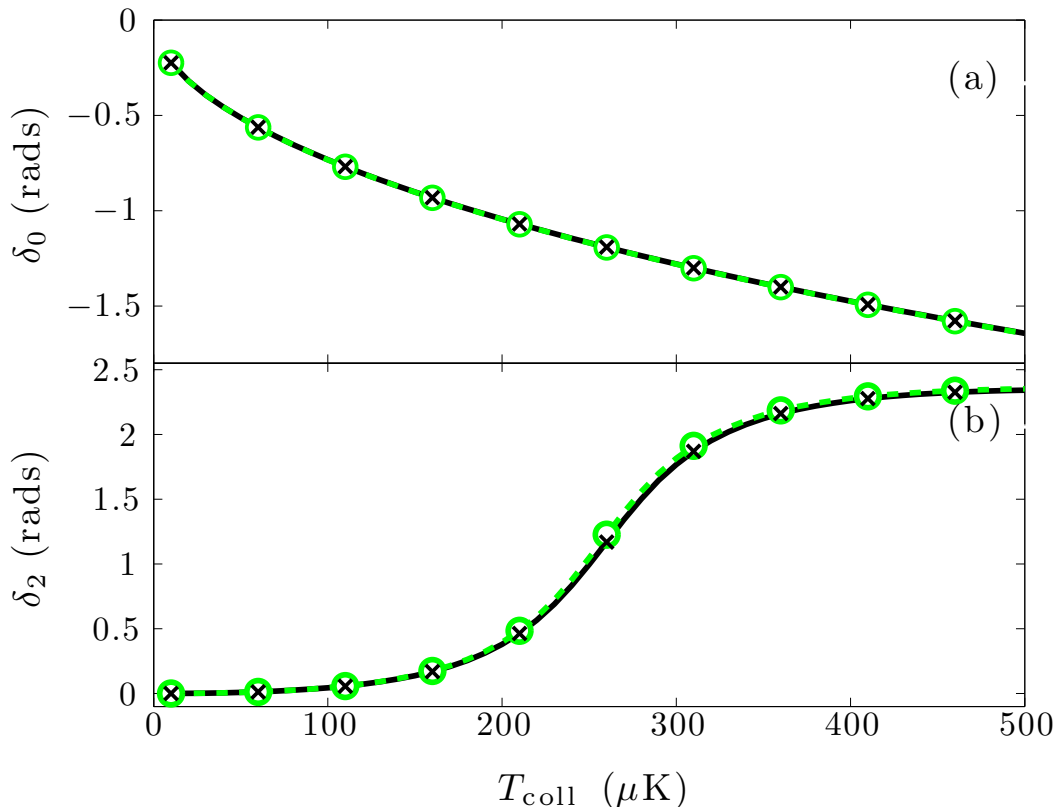
Figure 5.1: Numerically calculated *s*-wave (a) and *d*-wave (b) partial-wave phase shifts, by Eite Tiesinga (dashed green line with circles) using the optimized potentials of Strauss *et al.* [77], and by Paul Julienne (solid black line with crosses) in 2004 [32].

Obtaining $P(\theta)$ from the DSMC simulations (also binned into cells of size $\pi/32$ rads) is straightforward, since the scattered atoms can be labelled. This enables us to isolate their three-dimensional density easily. The scattered atoms are those of which have scattered with an atom that is not part of the isolated equilibrium evolution of a cloud [groups (i) and (ii) in Sec. 4.2.3].

We have removed a segment of the density near the collision axis by the isolation of scattered atoms, hence, this part of $P(\theta)$ is ignored in the fitting procedure. This presents a problem, as we wish to normalize the scattered distribution to unity (number of atoms is difficult to measure and varies from shot-to-shot). We make the approximation that the considered region of the experimental data has the same total probability for the scattering of an atom, as the normalized angular scattering probability obtained from the DSMC simulation.
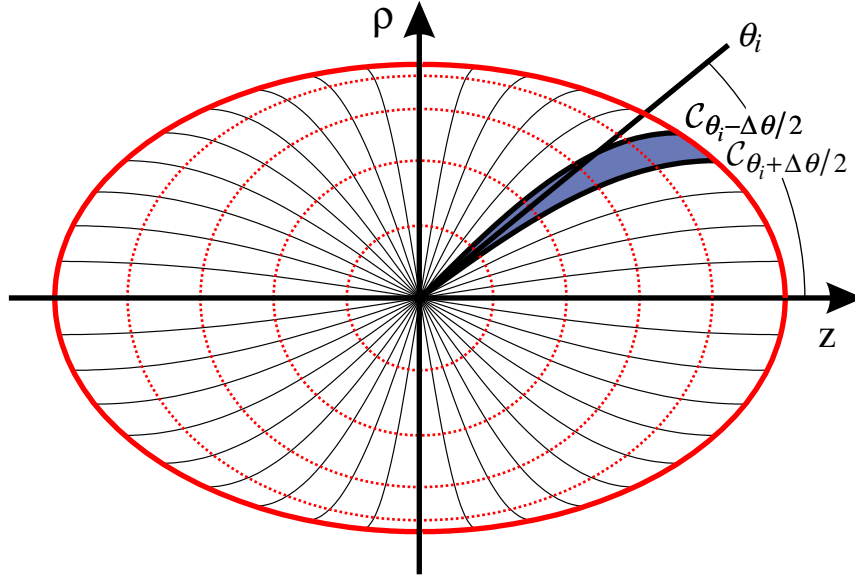
Figure 5.2: After the collision, the systems continues to evolve in the trapping potential. Thus, scattered atoms will evolve along curved trajectories. Here, this is indicated by the black curved lines, where the atoms are emitted from the origin. To account for this during the binning procedure, the boundaries ($\mathcal{C}_{\theta_i - \Delta\theta/2}$ and $\mathcal{C}_{\theta_i + \Delta\theta/2}$) of a bin centered at θ_i, with width $\Delta\theta$, are curved according to these trajectories. This image was presented in Ref. [33].

I.e,

$$\sum_{i=N_{\mathrm{r}}+1}^{N_{\mathrm{t}}-N_{\mathrm{r}}} P_{\mathrm{expt}}\left(\theta_i\right) = \sum_{i=N_{\mathrm{r}}+1}^{N_{\mathrm{t}}-N_{\mathrm{r}}} P_{\mathrm{sim}}\left(\theta_i\right), \tag{5.1}$$

where N_{t} is the total number of bins, and N_{r} is the number of bins removed from each end of the angular scattering probability for the experiment $P_{\mathrm{expt}}\left(\theta_i\right)$, and simulation $P_{\mathrm{sim}}\left(\theta_i\right)$.

5.2.2 Establishing the Best Fits

The best fits to the experimental data are determined by a χ^2 fitting procedure [79] for $P\left(\theta\right)$, which also allows us to establish confidence limits for the results. In detail, for each of the experimental $P_{\mathrm{expt}}\left(\theta\right)$, the χ^2 value is calculated for each of the simulated $P_{\mathrm{sim}}\left(\theta\right)$,

$$\chi^2 = \sum_{i=N_{\mathrm{r}}+1}^{N_{\mathrm{t}}-N_{\mathrm{r}}} \left[\frac{P_{\mathrm{expt}}\left(\theta_i\right) - P_{\mathrm{sim}}\left(\theta_i\right)}{\xi_i}\right]^2, \tag{5.2}$$

where ξ_i is the standard deviation for data point i.
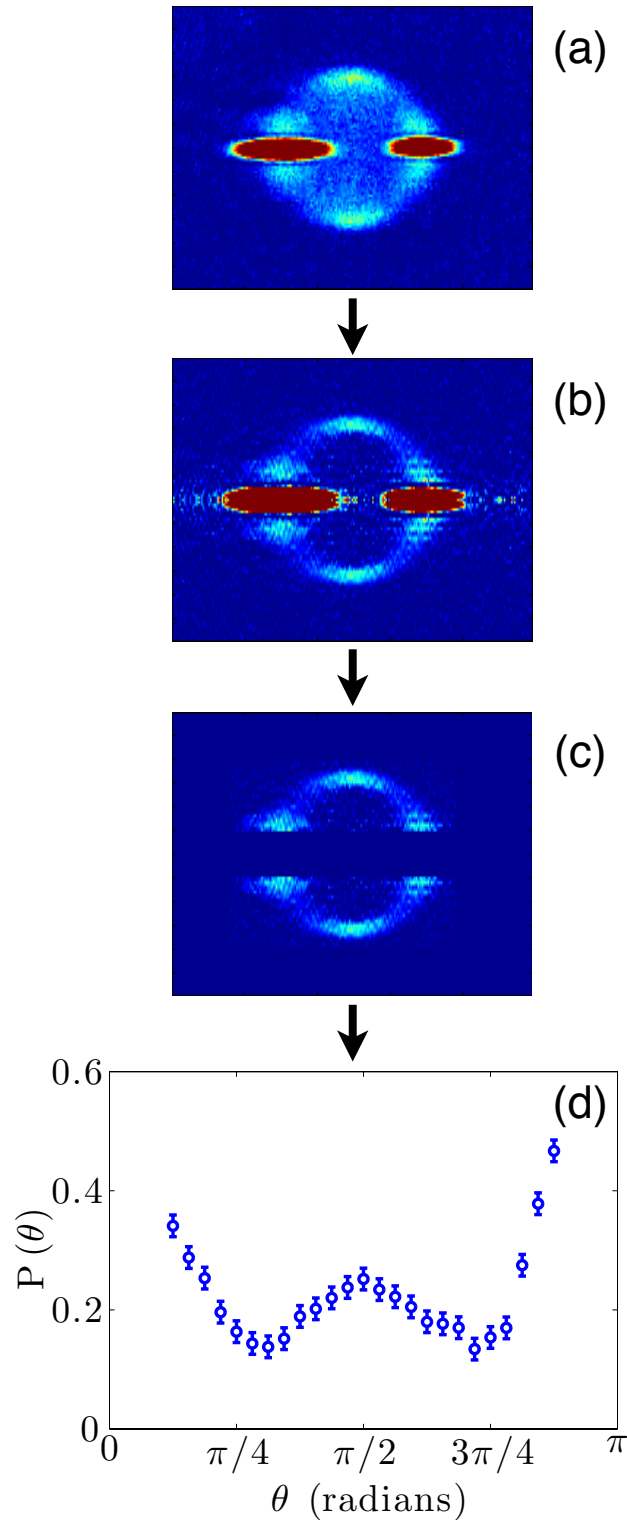
Figure 5.3: Illustration of the process of determining $P(\theta)$. (a) The column density extracted from the experimental images. (b) Three-dimensional density obtained by performing an inverse-Abel transform on the column density. (c) The scattered atoms are isolated as shown. (d) $P(\theta)$ established by binning the isolated density.

Since, the standard deviation of each data point in $P_{\text{expt}}(\theta)$ are not available (only one data set for each collision energy), we assume that the "goodness-of-fit" is good, errors are normally distributed, and the standard deviation of each data point is the same, i.e., $\xi_i = \xi_0$. This allows us to assign the standard deviation

$$\xi_0^2 = \frac{1}{N_t - 2N_r - M} \sum_{i=N_r+1}^{N_t - N_r} [P_{\text{expt}}(\theta_i) - P_{\text{sim}}(\theta_i)]^2 \qquad (5.3)$$

to each point, where $M = 1$ is the number of fit parameters.

The additional assumption that the model is linear (or near enough in the region of interest), confidence limits can be established according to the change in χ^2 about its minimum.

5.3 Sensitivity to Initial Conditions

Following the discussions of Sec. 4.1 and Sec. 5.1, our ability to accurately simulate the experiment is limited in two ways:

(i) The limited accuracy in the experimental measurements, and characterization of the ultracold-atomic collider, that we do not have precise knowledge of the cloud properties (i.e., sizes and atom numbers) prior to the collision. These relate to the initial conditions for the phase-space distributions we use to simulate the experiment (see Sec. 4.1.2).

(ii) The accuracy of existing theoretical two-body calculations of the ^{87}Rb phase shifts (as discussed in Sec. 5.1).

The main purpose of this chapter, is to discuss the limitations of the theoretical two-body calculations of the ^{87}Rb phase shifts. Hence, we first establish the collision energy regime, where our results are insensitive to the initial conditions of the phase-space distribution function, thus, eliminating the first limitation.

First, we discuss the sensitivity of our results to the number of atoms in each cloud, and the spatial widths of the clouds, as these were not well characterized. Then, we discuss the role that trap dynamics plays in the results.

5.3.1 Relative Number of Atoms and Spatial Widths

The initial phase-space distribution functions of the clouds prior to the collision are not well characterized, hence, assumptions of their form were made (see Sec. 4.1.2). Here, we establish the sensitivity of the collision results, to the number of atoms in each cloud, and the

spatial widths of the clouds. To do this, we vary the density parameters, which were obtained by fitting the experimental data, significantly (see Tab. 5.1), and observe changes in the collision energy of the simulation that gives the best agreement with the experimental data. The s- and d-wave differential cross section [Eq. (4.1)], and the collision energy dependent phase shifts calculated by Paul Julienne in Ref. [32] (see Fig. 4.1), were used to describe the interactions between the ^{87}Rb atoms in the DSMC simulations.

Case	$\mathcal{N}_P^1$ (10^5)	$\mathcal{N}_P^2$ (10^5)	ξ_{xy}^1 (μm)	ξ_{xy}^2 (μm)	ξ_z^1 (μm)	ξ_z^2 (μm)
0	2.6	1.4	9	9	50	50
1	2.8	1.2	9	9	50	50
2	2.3	1.7	9	9	50	50
3	2.6	1.4	11.25	6.75	62.5	37.5
4	2.6	1.4	6.75	11.25	37.5	62.5
5	2.6	1.4	9	9	37.5	37.5

Table 5.1: Parameters used for establishing the sensitivity to the initial conditions. Case 0 is the fitted parameters to the experimental data, while in the other cases, the parameters are varied by 25% from case 0.

Since, our results are determined from fitting $P(\theta)$, the accuracy is dependent upon the sensitivity of the differential cross section to changes in T_{coll}, as it determines the directions at which the atoms scatter. Prior to the d-wave resonance, there is a region of s- and d-wave interference that rapidly changes the angular dependence of the differential cross section. In this region, the results are found to be least sensitive to the initial conditions, and the highest accuracy can be obtained. This is illustrated in Fig. 5.4, which displays χ^2 for the $P(\theta)$ fits to the experimental data sets $T_{\text{coll}} = 113, 174$, and $225\,\mu$K, against the collision energy of the simulation. The cases 113 and $225\,\mu$K are outside this interference region, as indicated by the χ^2 minima being broader than that of the $174\,\mu$K case (which is within the region). For the former cases, the broad minima results in larger confidence limits of the best fit collision energy, and the results are sensitive to the initial conditions.

The least sensitive cases are found to be $T_{\text{coll}} = 146, 174$, and $204\,\mu$K. For the $146\,\mu$K data, varying the initial conditions leads to a $\pm 10\,\mu$K change in the collision energy of the best fit simulation, while at 174 and $204\,\mu$K this is reduced to $\pm 5\,\mu$K.
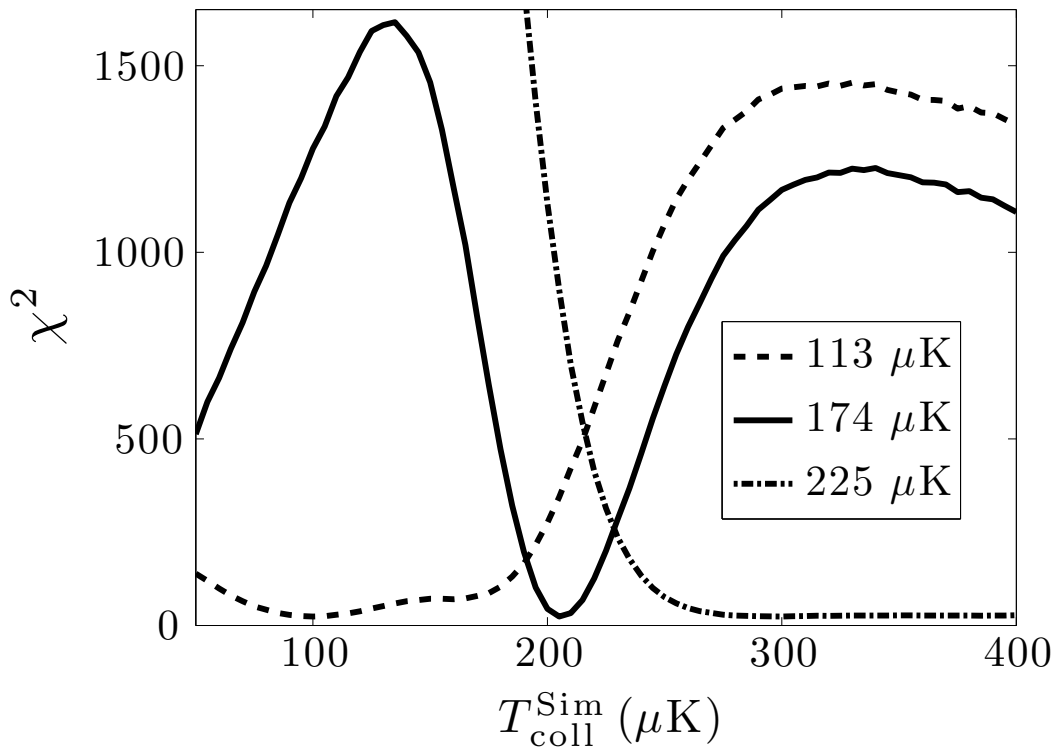
Figure 5.4: For the case 0 initial conditions, χ^2 is shown against the collision energy of the simulation, for three cases to illustrate the fitting process is most accurate when the differential cross section is most sensitive to changes in T_{coll}. The cases $T_{\mathrm{coll}} = 113$ and $225 \, \mu\mathrm{K}$ are in regions where it is insensitive, hence, the minima are broad. However, the $174 \, \mu\mathrm{K}$ case is within a region where the differential cross section changes rapidly, due to the *s*- and *d*-wave interference, hence, the minima is much sharper in comparison.

5.3.2   The Role of Trap Dynamics

Here, we seek to establish the dependence of the angular scattering distribution on T_{coll} through mechanisms other than the dependence of the phase shifts, i.e., the differential cross section. We know from Sec. 4.2.3 that increasing the collision energy while retaining the same differential cross section, has a little effect the number of scattered atoms. This is easily realized when considering the collision probability, which contains the product $v_{\mathrm{r}}\Delta t$. Qualitatively speaking, Δt is inversely proportional to v_{r}, thus, this product is constant.

Our main concern is the time scales of the collision and the trap in the radial direction. Ideally, the trap time scale should be much greater than that of the collision, otherwise, when

the system is imaged quarter the radial trap period after the clouds overlap, the collision may not yet be complete (the clouds still spatially overlap). This can be seen in Fig. 5.5, which shows the fraction of total scattered atoms to the total number of atoms $(\mathcal{N}_{sc}^1 + \mathcal{N}_{sc}^2)/\mathcal{N}_P$ (the superscript indicates which cloud). Below $T_{coll} = 100\ \mu K$ the number of scattered atoms decreases with decreasing T_{coll}. However, in this region, the total cross section increases (see Fig. 4.1) with decreasing T_{coll}, which is expected to cause an increase in scattered atoms.
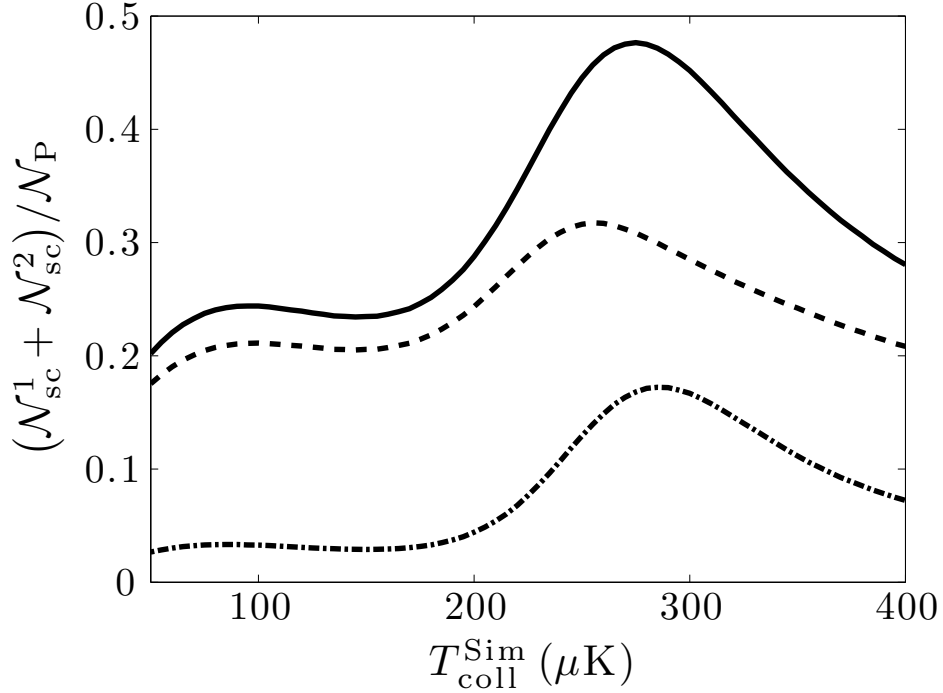
Figure 5.5: The total fraction of scattered atoms for the fitted set of initial conditions (Case 0) against the collision energy of the simulation. The solid black line gives scattered fraction for both groups (i) and (ii), while the dashed black line gives group (i), and dashed-dotted black line gives group (ii). The groups are defined as in Sec. 4.2.3: (i) scattered atoms that have not undergone any subsequent collisions, (ii) scattered atoms that have undergone additional collisions, including all collision partners.

In the extreme case, where the collision time scale is much greater than the trap time scales, atoms that scatter at the beginning of the collision, may undergo multiple trap oscillations in the radial direction. This is not ideal, as the angular distribution of scattered atoms becomes difficult to measure. Provided we concern ourselves with collision energy regimes $T_{coll} > 100\ \mu K$, these issues will be less of a concern, as increasing T_{coll} (increasing the relative speed of the clouds) diminishes the collision timescale.

For the cases we wish to consider, the $146\ \mu\mathrm{K}$ case has a small dependence on these issues, while for 174 and $204\ \mu\mathrm{K}$, these issues have negligible effect, i.e., the dependence on T_{coll} is solely through the differential cross section.

5.3.3   Summary of Important Results

We have seen that the experimental scattering patterns for $T_{\mathrm{coll}} = 146,\ 174$, and $204\ \mu\mathrm{K}$ are insensitive to the initial conditions, hence, suitable for us to focus our attention upon. These cases all occur in a regime where there is significant *s*- and *d*-wave interference, with the phase shifts varying rapidly with collision energy.

We have also seen that the results are largely insensitive to the collision energy of the simulation, except through the collision energy dependence of the differential cross section.

5.4   Results

In this section we present the main results of the chapter. We first apply the DSMC method to provide a quantitative model of the experiments, using the partial-wave phase shifts predicted by Paul Julienne. Our results show significant disagreement between the theoretical and experimental results suggesting that the theoretical phase shifts are inconsistent with experiment. From our simulations, we infer that the location of the *d*-wave resonance is significantly lower than Paul Julienne's, and more recently, Eite Tiesinga's predictions (see Sec. 5.1). We also use these simulations to investigate the role of the many-body dynamics in the experimental data, and show that a simple differential cross section model is inappropriate for providing a quantitative model of this experimental regime.

Motivated by the inadequacy of the current two-body predictions, we establish a model differential cross section to simulate experiments, and quantitatively determine the partial-wave phase shifts at $T_{\mathrm{coll}} = 174\ \mu\mathrm{K}$.

5.4.1 Comparison using Paul Julienne's Phase Shifts

Here, we compare our DSMC simulations to the experimental results of Thomas *et al.* [32], where the simulations use the *s*- and *d*-wave differential cross section

$$
\frac{d\sigma}{d\Omega} = \frac{4\hbar^2}{m^2 v_{\mathrm{r}}^2} \left[\overbrace{4\sin^2\delta_0}^{s\text{ wave}} + \overbrace{25\sin^2\delta_2 \left(3\cos^2\theta - 1\right)^2}^{d\text{ wave}} \right.
$$

$$
\left. + \underbrace{20\cos\left(\delta_0 - \delta_2\right)\sin\delta_0\sin\delta_2 \left(3\cos^2\theta - 1\right)}_{s\text{- and }d\text{-wave interference}} \right], \tag{5.4}
$$

discussed in Sec. 4.1.1, where the predictions of Paul Julienne are used for the collision energy dependence of the phase shifts (see Sec. 5.1), and the initial conditions given in Tab. 5.2. We only seek comparison to the cases $T_{\mathrm{coll}} = 146$, 174, and 204 μK, since, as discussed in Sec. 5.3 for these cases, we have the highest sensitivity to the phase shifts, and least sensitivity to the initial conditions. It is also shown that the results are dependent on the collision energy of the simulation only through the differential cross section.

$\mathcal{N}_{\mathrm{P}}^1\ (10^5)$	$\mathcal{N}_{\mathrm{P}}^2\ (10^5)$	$\xi_{xy}^1\ (\mu\mathrm{m})$	$\xi_{xy}^2\ (\mu\mathrm{m})$	$\xi_z^1\ (\mu\mathrm{m})$	$\xi_z^2\ (\mu\mathrm{m})$
2.6	1.4	9	9	50	50

Table 5.2: The parameters, determined from fits to the experimental data, used for the initial distribution [Eq. (4.8)] of the DSMC simulations in this chapter.

The column densities of the experiment, theoretical predictions, and best match to experiment are shown in Fig. 5.6. The inadequacy of the theoretical prediction is most obvious in the angular scattering probability shown in Fig. 5.7, which also shows the excellent agreement between the experiment and best fits.

These results indicate a discrepancy of $\approx 40\ \mu$K between the experimental measurements, and the predictions of Paul Julienne (similarly Eite Tiesinga), suggesting the *d*-wave resonance is shifted from the current theoretical predictions. However, our approach is not sufficient to determine this, as adjusting collision energy is effectively performing a one dimensional search through the *s*- and *d*-wave phase shifts constrained into a relationship by Paul Julienne's calculation. However, this basic idea can be adjusted to make a more comprehensive model, in which, the *s*- and *d*-wave phase shifts at the collision energy are free parameters. We will return to this in Sec. 5.4.3.
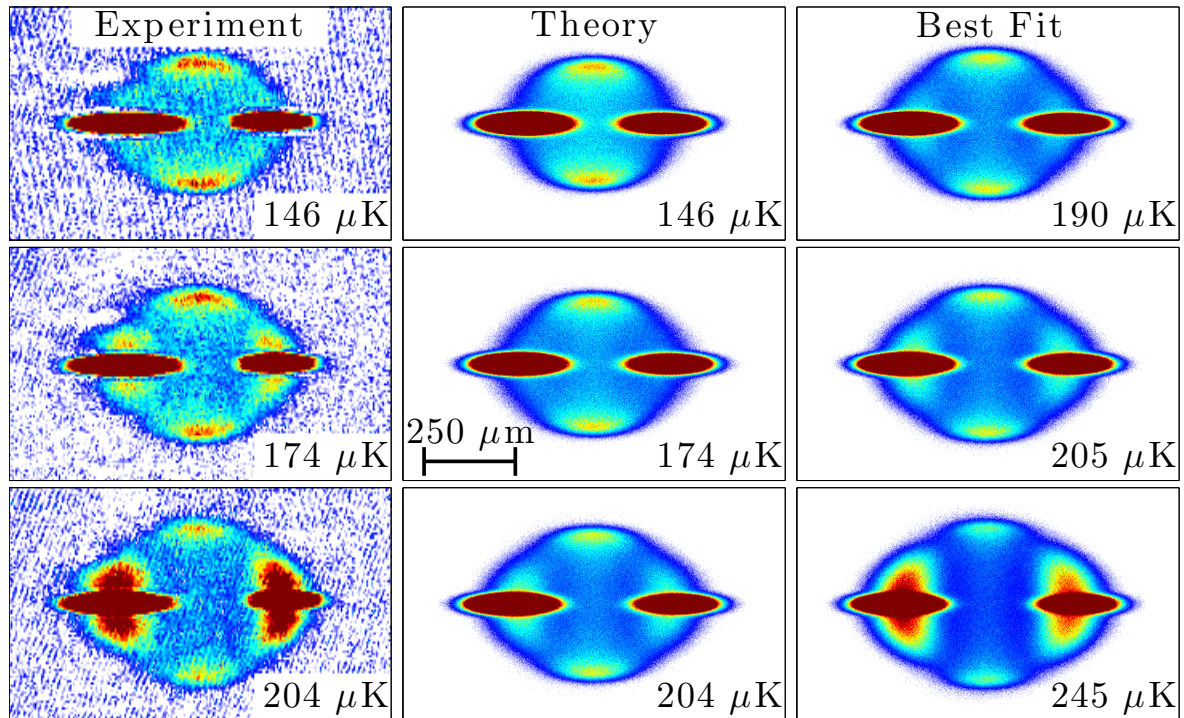
Figure 5.6: The experimental column densities are displayed in the first column, while the theoretical predictions (DSMC simulations furnished with the two-body calculations of the *s*- and *d*-wave phase shifts) are displayed in the second column. The collision energy of the experiment/simulation is displayed in the bottom right corner of each image. The best matches to the experimental data is to the right of the experimental data in the third column. These show a discrepancy of $30 - 40\ \mu$K between the collision energy of experiment and of theory. The confidence limits for the collision energy of the best fit for the $146\ \mu$K case is ± 10 μK, while $\pm 5\ \mu$K for the other two cases.
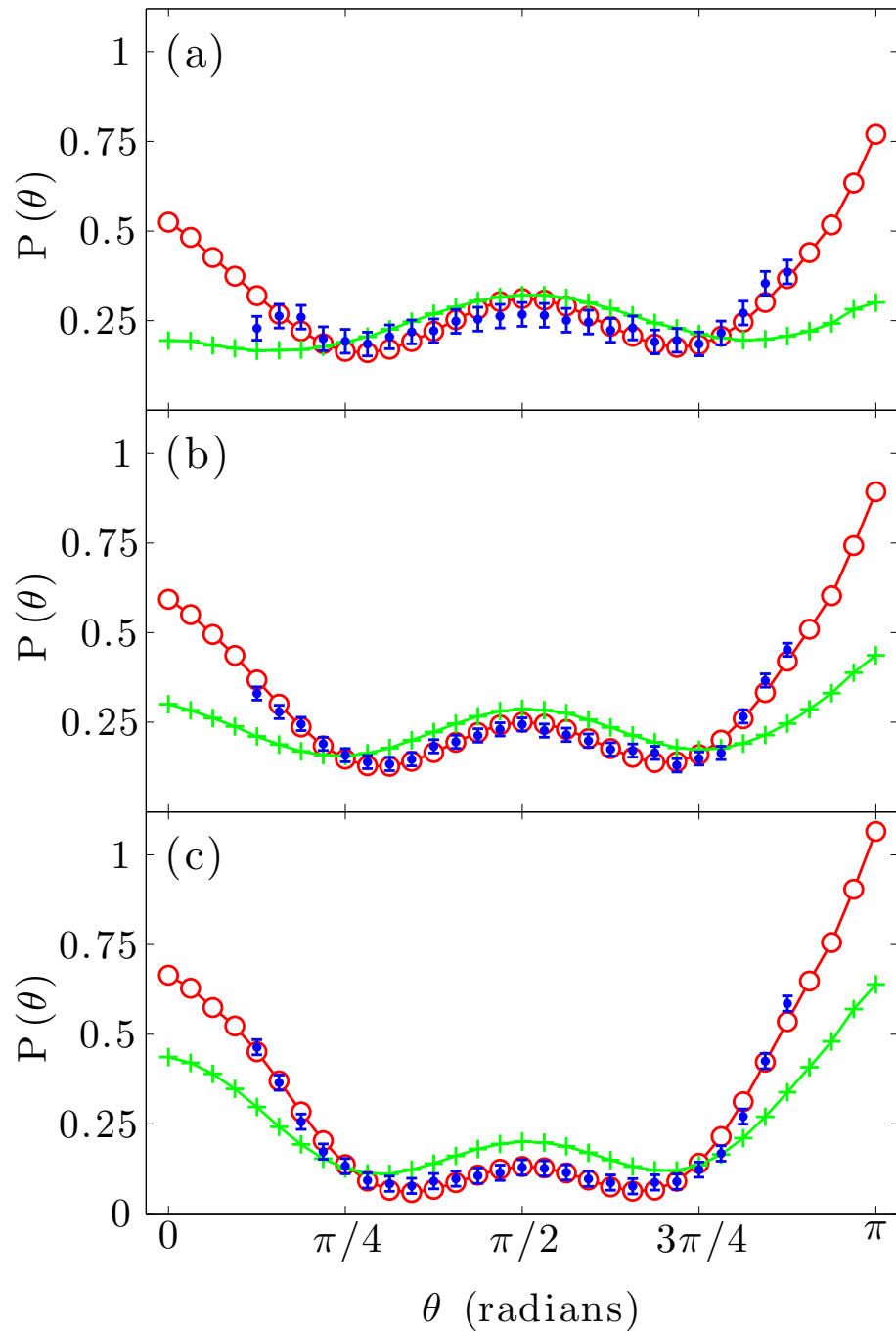
Figure 5.7: $P(\theta)$ for experiment (blue), theoretical prediction (green), and best fit (red) for the cases: (a) $T_{\text{coll}} = 146\,\mu\text{K}$, (b) $174\,\mu\text{K}$, and (c) $204\,\mu\text{K}$. We only show the experimental data points that are included in the fitting procedure, while the simulated lines include all points. The error bars for the experimental data are determined from the best fit using the method given in Sec. 5.2.2. The experimental data is normalized to the best fit (Sec. 5.2.1), and the theoretical prediction is normalized to the same value over the range of experimental data points, for the purpose of comparison.

5.4.2 Necessity of the DSMC method

Inadequacy of Differential Cross Section Analysis

The simple two-body approach of using the *s*- and *d*-wave differential cross section [Eq. (5.4)] itself as the fitting model for $P(\theta)$ does not provide a quantitative model of the experimental data, as the many-body effects are significantly large. For example, Fig. 5.8 compares the best fits of the DSMC simulation (as discussed in Sec. 5.4.1), and the differential cross section, to the experimental data for the case of $T_{\text{coll}} = 174\ \mu K$. Notably, using this simple model increases the discrepancy found between the experimental collision energy and best match using Paul Julienne's prediction for the phase shifts (see Sec. 5.4.1) from $\approx 40\ \mu K$ to $\approx 60\ \mu K$.

In the following, we examine the underlying physics that makes the differential cross section analysis inapplicable. Finally, we discuss the changes that would be required for the collider experiments to operate in a regime where differential cross section analysis could be used.

Many-Body and Finite Size Effects

Since, the trap dynamics are mostly accounted for in the procedure to determine the angular scattering probability (see Fig. 5.2, and Sec. 5.2.1), and the results are only dependent upon the collision energy through the differential cross section for $T_{\text{coll}} > 100\ \mu K$ (see Sec. 5.3.2), it is primarily atoms undergoing multiple collisions, and the finite sizes of the clouds, which cause the differential cross section analysis to be inapplicable. Indeed, the differential cross section analysis would be exact provided all the collisions occurred at the same point in space and time (i.e., no finite size effects), and the scattered atoms did not undergo any subsequent collisions.

The most important many-body effect, is atoms undergoing multiple collisions after the initial outscattering collision. This can significantly change the trajectory of the outscattered atoms, and causes asymmetries in the initial clouds to be resolved in $P(\theta)$ (e.g., see Fig. 5.7). The second source is the finite sizes of the clouds. This causes collisions to occur over a range of times and positions, which has the effect of broadening the collision halo.[2]

---

[2]Multiple collisions also broaden the collision halo.
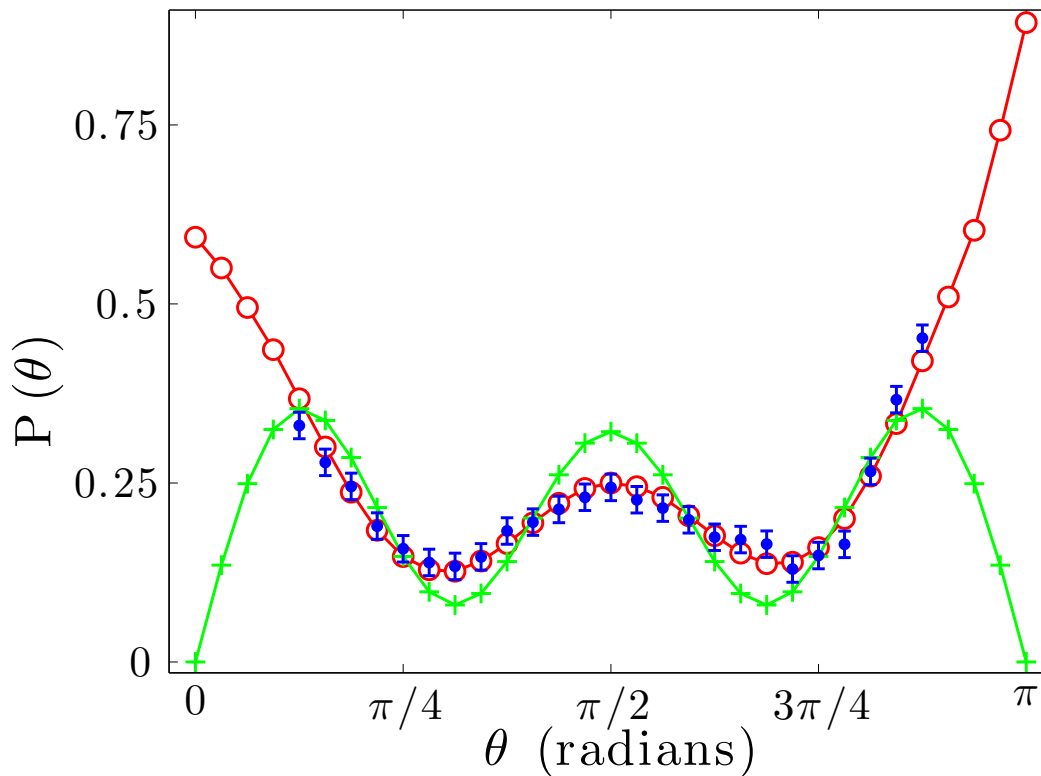
Figure 5.8: $P(\theta)$, for the case of $T_{\mathrm{coll}} = 174\,\mu K$, is shown for experiment (blue), the best fit of the differential cross section (green), and the best fit of the DSMC simulations of Sec. 5.4.1. This demonstrates that the differential cross section is a poor model for this experimental regime. The differential cross section model yields a best fit collision energy of $228\,\mu K$. We do not include the confidence limits, as the requirement that the model is appropriate for the "goodness-of-fit" in Sec. 5.2.2 is no longer fulfilled.

Minimizing the Many-Body and Finite Size Effects

The effects that cause the differential cross section to be a poor model for the fit, can be negated by changing the experimental set up in several ways. First, reducing the density of the clouds, so that, fewer collisions occur. How much of a reduction, and how to best achieve this, is given qualitatively by Fig. 4.9 and Eq. (4.18),

$$\mathcal{N}_{\text{sc}} = \frac{\mathcal{N}_{\text{P}}^2}{4\pi} m\beta\omega_x\omega_y\sigma_0. \tag{5.5}$$

Equation (5.5) is not accurate for $\mathcal{N}_{\text{sc}}/\mathcal{N}_{\text{P}} > 0.05$, but it qualitatively illustrates how a reduction in the density, reduces the scattering fractions. In Fig. 4.9, our results showed that for scattering fractions less than 15%, relatively few second collisions occurred.

The finite sizes of the clouds, become less important with increasing distance between the atoms when imaged and the collision site. Hence, one can use a weaker trap in the radial direction, or turn the trap off during, or after, the clouds collide. However, the imaging capabilities of the experiment must be kept in mind, since the density of the scattered atoms decreases as the collision halo expands.

5.4.3   Two-Parameter Model for Fitting to the Experiments

As we have shown in the previous sections, the current theoretical model for the partial-wave phase shift collision energy dependence is not in agreement with experiment, thus, we are motivated to give quantitative measures of the phase shifts from the experimental data. Here, we first introduce a model appropriate for performing such measurement, and then, give quantitative results of the experimental data at the collision energy of $T_{\text{coll}} = 174\,\mu\text{K}$.

The Model Differential Cross Section

Determining the simulation collision energy that most closely matches the experimental result is not a sufficiently general description to determine the phase shifts, since, this is a single parameter search (in terms of collision energy), and does not allow the *s*- and *d*-wave phase shifts to vary independently.

Here, we will concentrate on the $T_{\text{coll}} = 174\,\mu\text{K}$ case, since the angular scattering probability is most sensitive to changes the phase shifts, giving the most accurate results. In the simulation, the collision energy of the clouds is taken to be $T_{\text{coll}}^{\text{Sim}} = 174\,\mu\text{K}$, and we introduce a model, where all collisions occuring with $T_{\text{coll}} \leq 0.95\,T_{\text{coll}}^{\text{Sim}} = 165.3\,\mu\text{K}$, are described by the low energy *s*-wave (isotropic) differential cross section. For collisions occurring with $T_{\text{coll}} > 0.95\,T_{\text{coll}}^{\text{Sim}}$, we use the *s*- and *d*-wave differential cross section, with the

constant phase shifts $\bar{\delta}_0$ and $\bar{\delta}_2$ (the fitting parameters). I.e.,

$$\frac{d\sigma}{d\Omega} = \begin{cases} 8\pi a_{\mathrm{sc}}^2 & T_{\mathrm{coll}}^{ij} \leq 0.95\, T_{\mathrm{coll}}^{\mathrm{Sim}}, \\ D\left(\theta, \bar{\delta}_0, \bar{\delta}_2\right) & T_{\mathrm{coll}}^{ij} > 0.95\, T_{\mathrm{coll}}^{\mathrm{Sim}}, \end{cases} \tag{5.6}$$

where D indicates the *s*- and *d*-wave differential cross section [Eq. (5.4)], and ij indicates the colliding pair of test particles. The rational of model (5.6) is as follows: It ensures that low-energy collisions (e.g., collision within each cloud) occur at the background low-energy cross section. However, a majority of high-energy collisions between the clouds occur with $T_{\mathrm{coll}}^{ij} \approx T_{\mathrm{coll}}^{\mathrm{Sim}}$, and these contribute most significantly to the angular scattered distribution. Thus, for these collisions ($T_{\mathrm{coll}}^{ij} > 0.95\, T_{\mathrm{coll}}^{\mathrm{Sim}}$), we take the phase shifts to be constant parameters, which form the basis of our fitting procedure.

We have already established that a significant number of atoms undergo multiple inter-collisions, which occur at various T_{coll}^{ij} (most are close to $T_{\mathrm{coll}}^{\mathrm{Sim}}$). Thus, we test this model by comparing it to the simulated results of Sec. 5.4.1 for the cases of $T_{\mathrm{coll}} = 174$, and 205 μK, which include the full collision energy dependence of the phase shifts. These are the collision energy of the the simulations undertaken here, and the best fit from that section for the experimental results of $174\,\mu$K (e.g., see Fig. 5.8), respectively. This comparison is done by taking

$$\left\{\bar{\delta}_0, \bar{\delta}_2\right\} = \left\{\delta_0\left(T_{\mathrm{coll}}^i\right), \delta_2\left(T_{\mathrm{coll}}^i\right)\right\}, \tag{5.7}$$

for the model differential cross section 5.6, where T_{coll}^i refer to the two cases above, and the T_{coll} dependence is the same as that used in Sec. 5.4.1 (i.e., Paul Julienne's predictions). The Fig. 5.9 shows good agreement for this comparison, indicating our choice of model is sufficient to describe the regime of interest for the collider.

Best Fits and Corresponding Phase Shifts

By performing simulations for a range of $\bar{\delta}_0$ and $\bar{\delta}_2$, the best fits to the experimental data (see Fig. 5.10) are given by the phase shifts in Tab. 5.3. We find that the partial-wave predictions of Paul Julienne, and Eite Tiesinga in Sec. 5.1, give very good agreement for the *s*-wave phase shift, however, the *d*-wave phase shift is significantly different.

5.5 Conclusion

Our DSMC simulations have shown there is a serious discrepancy between theoretical predictions for the phase shifts of ^{87}Rb in the $200\,\mu$K regime. By developing an adjustable
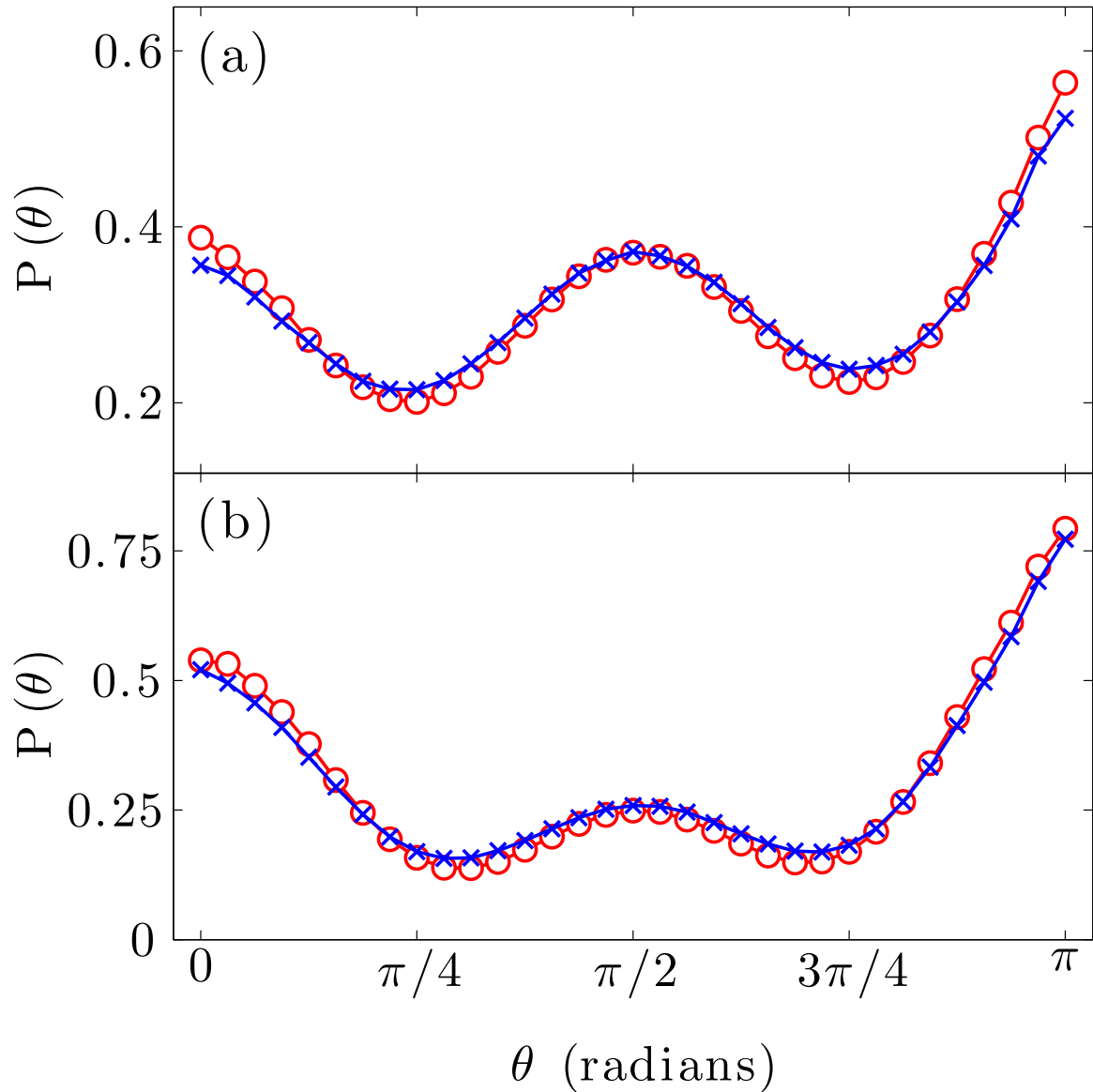
Figure 5.9: The red lines indicate the simulated results of Sec. 5.4.1 for the cases of $T_{\text{coll}}^{\text{Sim}} = 174$ (a), and 205 (b) μK. These results use the full collision energy dependence shown in Fig. 4.1. The blue lines are given by the *s*-wave cutoff model of this section. The good agreement shows that this simplified model is sufficient.
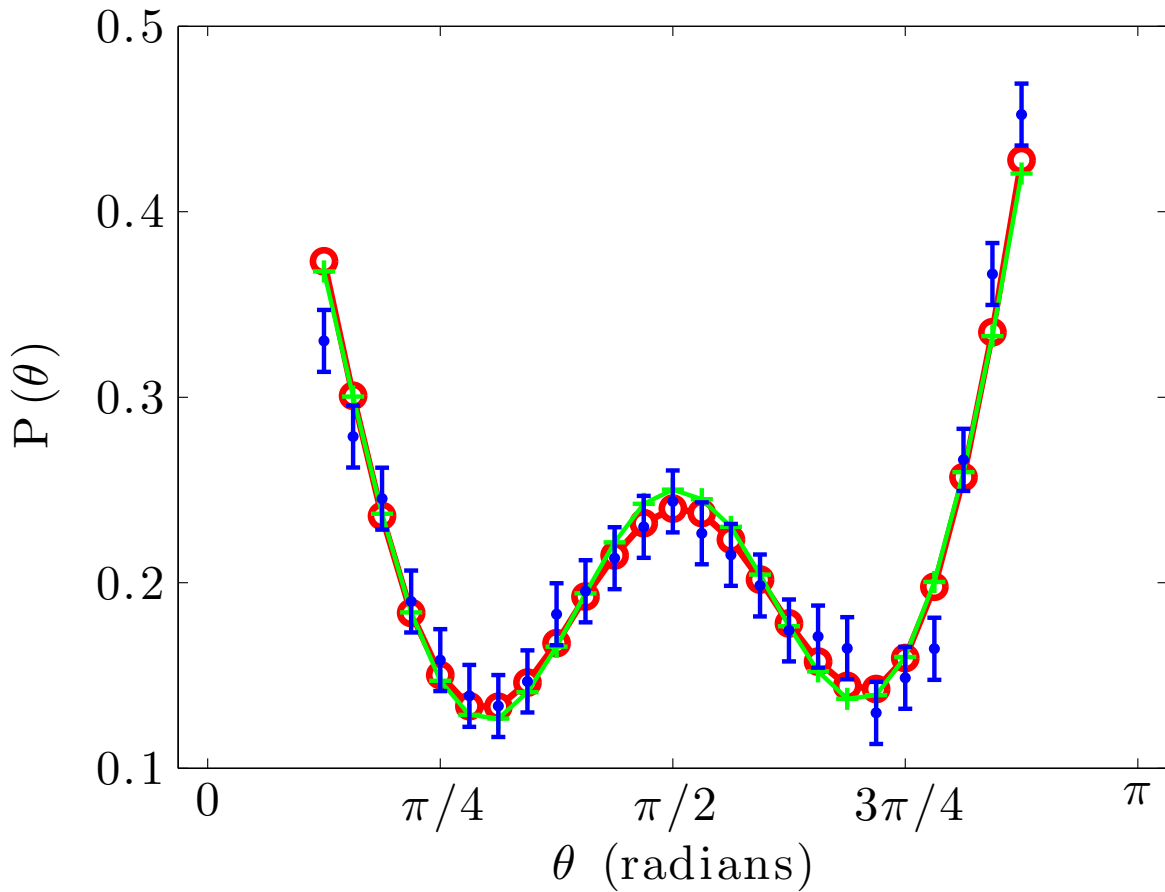
Figure 5.10: Comparison of the best fit of Sec. 5.4.1 (green), and the *s*-wave cutoff model of this section (red), to the experimental data for $T_{\mathrm{coll}} = 174\ \mu\mathrm{K}$ (blue). We only plot $P(\theta)$ over the considered range of the experimental $P(\theta)$, to highlight the quality of the agreement. The least-squares residual for case (a) is 0.0080, while for case (b) it is 0.0067.

$T_{\text{coll}}^{\text{Expt}}$	δ_0^{Fit}	δ_2^{Fit}	δ_0^A	δ_2^A	δ_0^B	δ_2^B
174	-0.97 ± 0.08	0.52 ± 0.02	-0.97	0.23	-0.97	0.23

Table 5.3: Here the fitted partial-wave phase shifts δ_i^{Fit}, and phase shifts calculated by Eite Tiesinga (δ_i^A), and Paul Julienne (δ_i^B), are shown, where $i = \{0, 2\}$. At this collision energy ($T_{\text{coll}} = 174~\mu\text{K}$), the two theoretical calculations agree to two significant figures. We find good agreement with the *s*-wave phase shift. However, the *d*-wave phase shift disagrees significantly.

model for the phase shifts, we have determined that this discrepancy lies mostly in the determination of the *d*-wave phase shift, and we have been able to provide a measure of the phase shifts at $174~\mu\text{K}$ to an accuracy that should be a constraint in future two-body calculations to improve our knowledge of the inter-atomic potentials.

The techniques that we have developed and applied, demonstrate that the ultracold-atomic collider (with appropriate theoretical analysis) can provide a tool for precision collision spectroscopy.

Chapter 6

Extension of DSMC to Include Quantum Many-Body Statistics

In this chapter, we discuss extending the DSMC method to the quantum many-body description given by the quantum Boltzmann equation. First, we derive the quantum many-body collision probability, and then, show how the algorithm presented in Chapter 3 is modified to accommodate this new collision probability. Then, we discuss the problems associated with constructing $f(\mathbf{p}, \mathbf{r}, t)$ during runtime, which is of crucial importance to the accuracy of the simulation. We suggest several new constructions of $f(\mathbf{p}, \mathbf{r}, t)$ to remedy this currently unsolved problem.

6.1 Derivation of the Quantum Collision Probability

Jackson and Zaremba [18] showed that the collision probability may be derived by treating the test particles as an accepted set of samples for the Monte Carlo integration of the collision rate per unit volume,

$$R(\mathbf{r}, t) = \frac{1}{m} \int \frac{d^6 u}{h^6} \int d\Omega \frac{d\sigma}{d\Omega} |\mathbf{p}_1 - \mathbf{p}| f f_1 (1 \pm f')(1 \pm f'_1), \qquad (6.1)$$

where $d^6 u = d^3 p \, d^3 p_1$. Deriving the collision probability in this fashion directly links the collisions of the test particles to the collision integral [Eq. (2.4)], and gives insight as to how the test particles function to solve the quantum BE. It also shows how the quantum many-body statistics are incorporated into the collision probability without resorting to *ad hoc* arguments. This result provides a useful framework to discuss the quantum extension of DSMC in detail. We now follow their methodology, and, where relevant to our purposes, we discuss details and make adjustments.

Rewriting Eq. (6.1) as

$$R\left(\mathbf{r}, t\right) = \int \frac{d^6 u}{h^6} w\left(\mathbf{u}, \mathbf{r}, t\right) g\left(\mathbf{u}, \mathbf{r}, t\right), \tag{6.2}$$

where $\mathbf{u}$ is a point in the six-dimensional momentum hyper-space, and the weight function is

$$w\left(\mathbf{u}, \mathbf{r}, t\right) \equiv f f_1, \tag{6.3}$$

and

$$g\left(\mathbf{u}, \mathbf{r}, t\right) = \frac{1}{m} \int d\Omega \frac{d\sigma}{d\Omega} \left|\mathbf{p}_1 - \mathbf{p}\right| \left(1 \pm f'\right) \left(1 \pm f'_1\right). \tag{6.4}$$

If the integrand is non-zero on the domain $\left[-\frac{p_{\max}}{2}, \frac{p_{\max}}{2}\right]$ for each of the six momentum components, we may approximate the integral by Monte Carlo integration with the following process: randomly select a point $\mathbf{u}_i$ in the non-zero domain of the integrand and randomly select a number w_i in the range $[0, w_{\max}]$, where $w_{\max}$ is the maximum of the weight function. If $w_i < w\left(\mathbf{u}_i, \mathbf{r}, t\right)$ then the point $\mathbf{u}_i$ is accepted. By repeating this N times, the approximate solution to the integral is given by

$$R\left(\mathbf{r}, t\right) \simeq \left(p_{\max}\right)^6 w_{\max} \frac{1}{N} \sum_{i=1}^{N_{\mathrm{acc}}} g\left(\mathbf{u}_i^{\mathrm{acc}}, \mathbf{r}, t\right), \tag{6.5}$$

where the summation is over only the accepted points $\mathbf{u}_i^{\mathrm{acc}}$, hence, $N_{\mathrm{acc}} \leq N$ is the number of such accepted points. If $g\left(\mathbf{u}, \mathbf{r}, t\right) = 1$, then, the integral would equate to the square of the density, i.e.,

$$n\left(\mathbf{r}, t\right)^2 = \int \frac{d^6 u}{h^6} f f_1, \tag{6.6}$$

and thus, we may write

$$n\left(\mathbf{r}, t\right)^2 \simeq \left(p_{\max}\right)^6 w_{\max} \frac{N_{\mathrm{acc}}}{N}. \tag{6.7}$$

Using this, we can rewrite Eq. (6.5) as

$$R\left(\mathbf{r}, t\right) \simeq n\left(\mathbf{r}, t\right)^2 \frac{1}{N_{\mathrm{acc}}} \sum_{i=1}^{N_{\mathrm{acc}}} g\left(\mathbf{u}_i^{\mathrm{acc}}, \mathbf{r}, t\right). \tag{6.8}$$

The momenta, $\mathbf{p}$ and $\mathbf{p}_1$, in the set of N_{acc} accepted points $\mathbf{u} = \left(\mathbf{p}, \mathbf{p}_1\right)$ are distributed according to $f\left(\mathbf{p}, \mathbf{r}, t\right)$. Since, the test particles are also distributed according to $f\left(\mathbf{p}, \mathbf{r}, t\right)$, they can form the set of accepted Monte Carlo samples. However, there are a limited number of test particles representing $f\left(\mathbf{p}, \mathbf{r}, t\right)$, demanding we take a reasonable cell volume about $\mathbf{r}$ to ensure enough test particles to implement Eq. (6.8). Two important questions we address later are:

(i) What considerations are important in deciding the cell volume?

(ii) What value of $n(\mathbf{r}, t)$ should be used for a finite cell volume?

Using Eq. (6.8), the number atoms which undergo a collision within the cell volume ΔV about the point $\mathbf{r}$ in the time interval t to $t + \Delta t$ is approximately

$$N_{\text{coll}} \simeq n(\mathbf{r}, t)^2 \frac{1}{N_{\text{acc}}} \sum_{i=1}^{N_{\text{acc}}} g(\mathbf{u}_i^{\text{acc}}, \mathbf{r}, t) \Delta V \Delta t, \tag{6.9}$$

Here we have assumed that the density across the volume is constant, thus, regardless of the approach taken for questions (i) and (ii) we may write $n(\mathbf{r}, t) = 2\alpha N_{\text{acc}}/\Delta V$, where we have taken the number of atoms in that volume to be $2N_{\text{acc}}$ (i.e., we have used the $2N_{\text{acc}}$ test particles to provide N_{acc} samples of $\mathbf{p}$, and N_{acc} samples of $\mathbf{p}_1$). Using this, and the fact that the number of test particles which undergo a collision is $\tilde{N}_{\text{coll}} = N_{\text{coll}}/\alpha$, since each atom is represented by $1/\alpha$ test particles, one arrives at

$$\tilde{N}_{\text{coll}} \simeq 2n(\mathbf{r}, t) \sum_{i=1}^{N_{\text{acc}}} g(\mathbf{u}_i^{\text{acc}}, \mathbf{r}, t) \Delta t. \tag{6.10}$$

Thus, we may associate a collision probability P_{ij}, for the pairs of test particles within the volume,

$$P_{ij} = n(\mathbf{r}, t) g(\mathbf{u}_i^{\text{acc}}, \mathbf{r}, t) \Delta t = n(\mathbf{r}, t) v_{\text{r}} \sigma_{\text{eff}} \Delta t, \tag{6.11}$$

where the factor of 2 has been dropped as two test particles participate in the collision, and i and j refer to the individual test particles of a given pair. The effective total cross section is given by

$$\sigma_{\text{eff}} = \int d\Omega \frac{d\sigma}{d\Omega} (1 \pm f')(1 \pm f_1'). \tag{6.12}$$

We now return to the questions (i) and (ii) posed earlier: We have seen that regardless of the choices for the cell volume and $n(\mathbf{r}, t)$, we arrive at the same collision probability for testing $N_{\text{acc}} = n(\mathbf{r}, t) \Delta V/2\alpha$ collisions. Thus, the choices only have an effect on how well $n(\mathbf{r}, t)$, f', and f_1' are represented, and hence, the accuracy of the simulation. Here, we consider three different choices: (1) the original DSMC method, (2) the NNC scheme, and (3) a scheme we call *locally sampled density* (LSD). The relevant characteristics of the schemes are shown in Tab. 6.1. Before we introduce the LSD scheme, it is useful to discuss the first two.

In the original DSMC method, $\Delta V = \Delta V_c$, and the density is the average density of the cell n_c. The current form (P_{ij} given by Eq. (6.11) and $N_{\text{acc}} = N_c/2$) corresponds to $M_c = N_c^2/2$ collisions. In light of the discussions in Sec. 3.3.3, we know that this derivation should be modified, such that, $M_c = N_c(N_c - 1)/2$, which is done by now taking $N_{\text{acc}} = (N_c - 1)/2$. Thus, this choice reduces Eq. (6.11) to exactly that of which is obtained by

Scheme	ΔV	$n(\mathbf{r}, t)$
Original DSMC	ΔV_c	n_c
NNC	$2\alpha/n_c$	n_c
LSD	$2\alpha/n(\mathbf{r}_{\text{com}}, t)$	$n(\mathbf{r}_{\text{com}}, t)$

Table 6.1: Choices for ΔV and $n(\mathbf{r}, t)$ for the different schemes.

Bird [35], Eq. (3.10), with the appropriate scaling for Eqs. (3.12), and $\sigma(v_{\text{r}}) = \sigma_{\text{eff}}$. The NNC scheme can be understood as restricting ΔV to the volume, which on average for the collision cell, contains only two test particles, however, retaining the density to be n_c.

We have developed the LSD scheme, which restricts ΔV to contain two test particles using the (yet to be determined) density evaluated at the centre-of-mass $n(\mathbf{r}_{\text{com}}, t)$. This density could be obtained via an ansatz for the density or the interpolation of all test particles in the simulation or in the cell itself. However, if $n(\mathbf{r}_{\text{com}}, t)$ is determined from the test particles, it can reintroduce the finite number fluctuation issues discussed in Sec. 3.3.3, and we find for the classical DSMC algorithm, this disadvantage is significant enough that it should not be used. The fluctuation issues can, ofcourse, be circumvented by using more test particles. However, we shall see later in Sec. 6.3 that the quantum extension of DSMC requires large cells for many test particles, which causes n_c to be a very coarse grained representation. Here, the LSD scheme is expected to be most useful, as it can remove this coarse graining, giving potentially more accurate simulations.

6.2 Adjustments to the DSMC Algorithm

Here, we discuss how the addition of the quantum many-body component changes the classical DSMC algorithm we presented in Chapter 3.

6.2.1 Scaling and LATS

Scaling of the collision probability and number of tested collisions is discussed in Sec. 3.3.3.

$$P_{ij} \to \tilde{P}_{ij} = \frac{P_{ij}}{\Lambda}, \tag{6.13a}$$

$$M_c \to \tilde{M}_c = M_c\Lambda, \tag{6.13b}$$

is now given with

$$\Lambda = \frac{\left\lceil M_c \Delta t \left[n(\mathbf{r}, t) v_{\text{r}} \sigma_{\text{eff}}\right]_{\text{max}} \right\rceil}{M_c}. \tag{6.14}$$

For computational simplicity and performance, we take

$$[n\left(\mathbf{r}, t\right) v_{\mathrm{r}} \sigma_{\mathrm{eff}}]_{\max} = n_{\max} \left[1 + \varepsilon f_{\max}\right]^2 \left[v_{\mathrm{r}} \sigma\left(v_{\mathrm{r}}\right)\right]_{\max}, \tag{6.15}$$

where $n_{\max}$ and $f_{\max}$ are the maximum values within the cell, and $\varepsilon = 1\,(0)$ for bosons (fermions). Thus,

$$\tilde{P}_{ij} = \frac{M_c n\left(\mathbf{r}, t\right) v_{\mathrm{r}} \sigma_{\mathrm{eff}} \Delta t}{\left\lceil M_c \Delta t n_{\max} \left[1 + \varepsilon f_{\max}\right]^2 \left[v_{\mathrm{r}} \sigma\left(v_{\mathrm{r}}\right)\right]_{\max}\right\rceil}. \tag{6.16}$$

Finally, for the LATS scheme, the relevant collision times of a cell are now given by

$$\tau_c^{\mathrm{coll}} = \overline{n\left(\mathbf{r}, t\right) v_{\mathrm{r}} \sigma_{\mathrm{eff}}}^{-1}, \tag{6.17a}$$

$$\tau_c^{\max} = \left\{n_{\max} \left[1 + \varepsilon f_{\max}\right]^2 \left[v_{\mathrm{r}} \sigma\left(v_{\mathrm{r}}\right)\right]_{\max}\right\}^{-1}. \tag{6.17b}$$

6.2.2 Testing and Implementation of Collisions

The evaluation of $\tilde{P}_{ij}$ is more involved, due to the addition of the integral

$$\sigma_{\mathrm{eff}} = \int d\Omega \frac{d\sigma}{d\Omega}\left(1 \pm f'\right)\left(1 \pm f_1'\right). \tag{6.18}$$

During runtime, this integral must be evaluated, which, analytically, is almost always intractable, and the analytical solutions can often be infeasible to implement numerically.[1] Then, if the test particles collide, they scatter at angles determined by $\frac{d\sigma}{d\Omega}\left(1 \pm f'\right)\left(1 \pm f_1'\right)$. We can combined these procedures into one, by employing the Monte Carlo method of staked probabilities. This gives an approximate solution to Eq. (6.18), while determining the scattering angles of the particles if they collide. The collision probability is taken to be

$$\tilde{P}_{ij} = \frac{2\pi}{N_{\mathrm{s}}} \sum_{k=1}^{N_{\mathrm{s}}} \tilde{P}_{ij}^{\Omega_k}, \tag{6.19}$$

where N_{s} is the number of samples, and

$$\tilde{P}_{ij}^{\Omega_k} = \frac{n\left(\mathbf{r}, t\right) v_{\mathrm{r}} \Delta t}{\Lambda} \left[\frac{d\sigma}{d\Omega}\left(1 \pm f'\right)\left(1 \pm f_1'\right)\right]^{\Omega_k}, \tag{6.20}$$

with $[x]^{\Omega_k}$ indicating that x is evaluated at the randomly selected angles Ω_k. The collision goes ahead if $R < \tilde{P}_{ij}$, where R is a random number uniformly distributed between 0 and 1, and the scattering angles are given as Fig. 6.1 demonstrates.

---

[1] For example, Eq. (6.18) can be solved for the equilibrium Bose-Einstein distribution, however, the solution is an infinite sum.
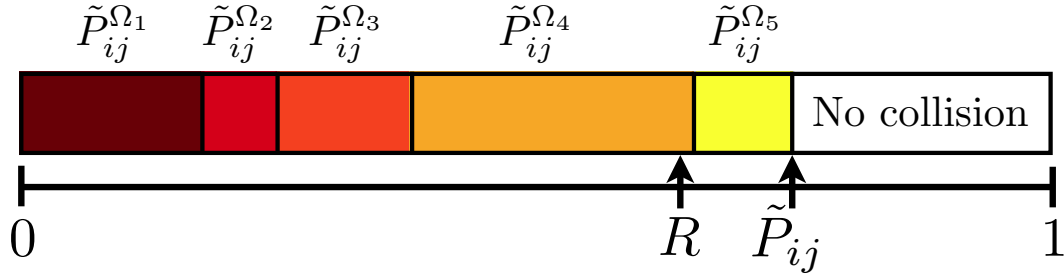
Figure 6.1: Stacked probabilities: If $R \geq \tilde{P}_{ij}$, then no collision goes ahead. Otherwise, the scattering angles are given by Ω_k, such that, $\sum_{l=1}^{k-1} \tilde{P}_{ij}^{\Omega_l} \leq N_s R/2\pi < \sum_{l=1}^{k} \tilde{P}_{ij}^{\Omega_l}$. In the case illustrated here, a collision goes ahead, and the scattering angles are given by Ω_4.

Methods that are not derived as in Sec. 6.1, usually include the quantum many-body statistics by selecting only one set of angles Ω_1, according to the differential cross section. Then, whether or not the collision goes ahead, is determined by testing a collision probability

$$P_{ij} \propto n\left(\mathbf{r}, t\right) \sigma_{\mathrm{T}} v_{\mathrm{r}} \Delta t \left[\left(1 \pm f'\right)\left(1 \pm f_1'\right)\right]^{\Omega_1}, \tag{6.21}$$

where $\sigma_{\mathrm{T}} = \int \frac{d\sigma}{d\Omega} d\Omega$. This is expected to be sufficient for large numbers of test particles, however, when it the description is insufficient, one will have to resort to the above.

6.3 Runtime Constructions of $f\left(\mathbf{p}, \mathbf{r}, t\right)$

How $f\left(\mathbf{p}, \mathbf{r}, t\right)$ is established for the runtime evaluation of σ_{eff}, required to implement the collision probability, is of crucial importance to the accuracy of the simulation. Our initial investigations have shown that, where possible, an ansatz for $f\left(\mathbf{p}, \mathbf{r}, t\right)$ provides a more accurate and efficient simulation. For example, Bonasera *et al.* [54] used a parameterized Fermi-Dirac distribution, and Lopez-Arias and Smerzi [80] used a parameterized Bose-Einstein distribution. However, implementing an ansatz is not always feasible, particularly for systems away from equilibrium, and one must resort to extracting the full six-dimensional distribution $f\left(\mathbf{p}, \mathbf{r}, t\right)$ from the test particles themselves. We have found that, with a simple implementation, the equilibrium state of a quasi-degenerate Bose gas is not always held, and the system evolves to a new equilibrium state, which is more classical in nature, i.e., approaching the Maxwell-Boltzmann distribution. This was also observed by Garcia and Wagner [81]. The equilibrium state the system evolves to depends on the discretization parameters, and requires optimization for the particular case under consideration. This is challenging for

nonequilibrium systems, e.g., for the collisions of ultracold degenerate clouds, for which, the optimized parameters for the initial and final states can be different. Ideally, the algorithm should be robust and stand alone, or the discretization effects well understood and easily accounted for. However, this is largely an unexplored problem, with the exception of the study of Garcia and Wagner [81], and is often overlooked by people working in this area.[2] Here, we do not solve this problem, but present several possible avenues of investigations.

6.3.1 Analytic Result Required for Test of Collision Rate

Until now, the tests we performed on our (classical) DSMC algorithm were largely concerned with giving the correct collision rate (see Sec. 4.2). This is a necessary requirement for the accuracy of the simulation, but not sufficient in the quantum many-body context. The testbed distribution for the collision rate is a degenerate case of the Bose-Einstein distribution

$$f(\mathbf{p}, \mathbf{r}) = \frac{1}{\exp\{\beta[H(\mathbf{p}, \mathbf{r}) - \mu]\} - 1} = \sum_{j=1}^{\infty} \exp\{j\beta[\mu - H(\mathbf{p}, \mathbf{r})]\}, \qquad (6.22)$$

where H is the Hamiltonian of the system. Using the Gaussian expansion, we can solve for the collision rate [Eq. (6.1)], yielding

$$R(\mathbf{r}) = \frac{1}{2\sqrt{2}\hbar^6} \frac{\sigma_1}{m} \left(\frac{m}{\pi\beta}\right)^{\frac{7}{2}} \sum_{j,k=1}^{\infty} \exp\{\beta[j+k][\mu - U(\mathbf{r})]\} \times$$

$$\left\{\frac{1}{jk}\left[\frac{\sqrt{j+k}}{jk} + 2\sum_{l=1}^{\infty}\frac{\sqrt{j+k+l}}{(j+l)(k+l)}\exp\{l\beta[\mu - U(\mathbf{r})]\}\right] + \right.$$

$$\left. \sum_{l,n=1}^{\infty}\frac{\sqrt{j+k+l+n}}{(j+l)(k+l)(j+n)(k+n)}\exp\{\beta[l+n][\mu - U(\mathbf{r})]\}\right\}, \quad (6.23)$$

where we have assumed a constant differential cross section that yields the total cross section σ_1. This result was also found by Lopez-Arias and Smerzi [80]. For a harmonic potential,

---

[2]For methods based on molecular dynamics like closest-approach collisions, which the closest-approach distance does not scale with $\mathcal{N}_{\mathrm{T}}$, it is unclear whether one should be concerned with this, since these methods ultimately do not solve the quantum BE (assumes point particle collisions).

integrating over each position space direction is relatively simple, and gives

$$R = \frac{1}{\omega_x \omega_y \omega_z} \frac{1}{\hbar^6} \frac{m\sigma_1}{\pi^2 \beta^5} \sum_{j,k=1}^{\infty} \exp\left[\beta \left(j + k\right) \mu\right] \times$$

$$\left\{ \frac{1}{jk} \left[\frac{1}{jk} \frac{1}{\left(j+k\right)} + 2 \sum_{l=1}^{\infty} \frac{1}{\left(j+l\right)\left(k+l\right)} \frac{1}{\left(j+k+l\right)} \exp\left[l\beta\mu\right] \right] + \right.$$

$$\left. \sum_{l,n=1}^{\infty} \frac{1}{\left(j+l\right)\left(k+l\right)\left(j+n\right)\left(k+n\right)} \frac{1}{\left(j+k+l+n\right)} \exp\left[\beta\left(l+n\right)\mu\right] \right\}. \quad (6.24)$$

These expressions can be evaluated numerically, and give us a benchmark to test the initial accuracy of the DSMC simulation. However, initially the agreement between the analytical collision rate and the numerical collision rate determined by DSMC can be very good, but when the system is evolved in time, it can still progressively evolve away from the initial distribution. This must be checked for, in conjunction with the collision rate.

6.3.2   Three Constructions

For systems away from equilibrium, it is not always feasible to use an ansatz for $f\left(\mathbf{p}, \mathbf{r}, t\right)$, thus, one must resort to establishing $f\left(\mathbf{p}, \mathbf{r}, t\right)$ from the test particles. We present three constructions of $f\left(\mathbf{p}, \mathbf{r}, t\right)$, the first being the typical construct found in literature, and the other two, suggestions we make to combat issues discussed in due course. We also discuss the mechanism that causes the system to evolve away from the initial state.

Construction (c1):

The simplest construction of $f\left(\mathbf{p}, \mathbf{r}, t\right)$ is the mean density of the cell multiplied by a normalized momentum distribution obtained from the test particles within the cell $\mathcal{K}_c\left(\mathbf{p}, t\right)$,

$$f_c\left(\mathbf{p}, t\right) = n_c \mathcal{K}_c\left(\mathbf{p}, t\right), \quad (6.25)$$

where

$$\int \frac{d^3p}{h^3} \mathcal{K}_c\left(\mathbf{p}, t\right) = 1. \quad (6.26)$$

$\mathcal{K}_c\left(\mathbf{p}, t\right)$ can be determined binning the test particles into a grid of cells in momentum space with width Δp_i in the $i = \left(x, y, z\right)$ direction. This can be performed in several ways, e.g., the particles can be mapped to the nearest grid point (the so called *nearest grid point* or

zeroth order scheme), and the resulting distribution convoluted with a Gaussian function. The convolution theorem allows the convolution to be easily performed in Fourier space, however, performing a Fast Fourier Transform (FFT), and then, the inverse-FFT for each cell is computationally taxing. We find that similar accuracy can be achieved with the higher order interpolation schemes of Ref. [78], and in most cases, for less computational effort.

Construction (c2):

For construction (c1), $\mathcal{K}_c(\mathbf{p}, t)$ requires N_c to be large for a sufficiently accurate description, hence, large ΔV_c, causing the density to be coarsely grained. The first new construction we suggest, is to use the LSD scheme for the density,

$$f_c(\mathbf{p}, t) = n(\mathbf{r}_{\text{com}}, t) \, \mathcal{K}_c(\mathbf{p}, t). \tag{6.27}$$

$n(\mathbf{r}_{\text{com}}, t)$ can be established by the convolution or interpolation methods as discussed for $\mathcal{K}_c(\mathbf{p}, t)$ above. This will give a more accurate description of the density, but, as we noted earlier, this can reintroduce the fluctuation issues discussed in Sec. 3.3.3. However, we note that the form of construction (c1) [Eq. (6.25)] does not remove these issues in the quantum many-body description, since the product

$$n(\mathbf{r}, t) (1 \pm f') (1 \pm f_1'), \tag{6.28}$$

in the collision probability is not linear in $n(\mathbf{r}, t)$. Furthermore, the fluctuation issues may be less significant, as we require large N_c for $\mathcal{K}_c(\mathbf{p}, t)$.

Construction (c3):

A careful study is required to determine whether the coarse graining of construction (c1), or fluctuation issues in both constructions (c1) and (c2), will be important. However, our initial investigations suggest that the fluctuations are most important in both cases. Furthermore, this causes the two problems: (a) accurately representing the collision rate, and (b) the progressive evolution to another state, to be coupled. This motivates us to extend the methods of Sec. 3.3.3 to remove the fluctuation issues, and uncouple the problems. For Eq. (6.25), Eq. (6.28) reads

$$n_c \pm n_c^2 \left[\mathcal{K}_c(\mathbf{p}', t) + \mathcal{K}_c(\mathbf{p}_1', t) \right] + n_c^3 \mathcal{K}_c(\mathbf{p}', t) \, \mathcal{K}_c(\mathbf{p}_1', t), \tag{6.29}$$

thus, the collision rate features N_c^2, N_c^3, and N_c^4. For Poissonian distributed fluctuations, one can show

$$\overline{N_c \left(N_c - 1\right)}^* = \overline{N_c}^2, \tag{6.30a}$$

$$\overline{N_c \left[N_c \left(N_c - 3\right) + 1\right]}^* = \overline{N_c}^3, \tag{6.30b}$$

$$\overline{N_c \left\{N_c \left[N_c \left(N_c - 6\right) + 11\right] - 6\right\}}^* = \overline{N_c}^4, \tag{6.30c}$$

where the asterisks indicates we have taken into account that the DSMC simulation neglects cells with single occupation. Thus, the fluctuation affects can be removed by taking $M_c = N_c/2$, and by replacing Eq. (6.29) with

$$\vartheta \left(N_c - 1\right) \pm \vartheta^2 \left[N_c \left(N_c - 3\right) + 1\right] \left[\mathcal{K}_c \left(\mathbf{p}', t\right) + \mathcal{K}_c \left(\mathbf{p}_1', t\right)\right] + $$
$$\vartheta^3 \left\{N_c \left[N_c \left(N_c - 6\right) + 11\right] - 6\right\} \mathcal{K}_c \left(\mathbf{p}', t\right) \mathcal{K}_c \left(\mathbf{p}_1', t\right), \tag{6.31}$$

where $\vartheta = \alpha/\Delta V_c$, giving our second suggested construction. In detail, this gives

$$P_{ij} = v_{\mathrm{r}}\Delta t \int d\Omega \frac{d\sigma}{d\Omega} \vartheta \left[\left(N_c - 1\right) \pm \vartheta \left[N_c \left(N_c - 3\right) + 1\right] \left[\mathcal{K}_c \left(\mathbf{p}', t\right) + \mathcal{K}_c \left(\mathbf{p}_1', t\right)\right] + $$
$$\vartheta^2 \left\{N_c \left[N_c \left(N_c - 6\right) + 11\right] - 6\right\} \mathcal{K}_c \left(\mathbf{p}', t\right) \mathcal{K}_c \left(\mathbf{p}_1', t\right)\right]. \tag{6.32}$$

We have neglected the fact that $\mathcal{K}_c \left(\mathbf{p}', t\right)$ and $\mathcal{K}_c \left(\mathbf{p}_1', t\right)$ are also determined from the test particles, hence, have correlated fluctuations. The fluctuations may not have a significant effect, and they may be negated by the scheme which established $\mathcal{K}_c \left(\mathbf{p}, t\right)$.

Mechanism for Unphysical Evolution

We now discuss the mechanism that causes the system to progressively evolve away from the initial equilibrium state. This artificial evolution is due to the transfer of information in the collisions of test particles. The NNC scheme, which was introduced in a classical context, combats transfer of information of spatially separated collision partners, however, with the inclusion of quantum many-body statistics $[\left(1 \pm f'\right) \left(1 \pm f_1'\right)]$, there is now another mechanism which destroys the correlations. We are concerned with the final states to which the test particles scatter, which is determined by $\frac{d\sigma}{d\Omega} \left(1 \pm f'\right) \left(1 \pm f_1'\right)$. Since, the momentum distributions are determined from all the test particles within the cell, we are effectively spreading this information across the entire cell, furthermore, if the distributions are not well determined, this can render the $\left(1 \pm f'\right) \left(1 \pm f_1'\right)$ terms ineffective. The density plays a role, but the momentum distributions are less accurately determined. Such problems have been seen by our initial investigations and by Garcia and Wagner [81].

These problems we have discussed with the constructions, and this artificial evolution, merit a careful study to determine the weaknesses of quantum DSMC algorithms, or give the solutions, e.g., the use of an ansatz for $f(\mathbf{p}, \mathbf{r}, t)$ circumvents these problems. This study extends beyond the scope and aims of this work. Our main motivation for including this chapter, is as a record of work undertaken, and to provide a platform for future work on the quantum BE.

Chapter 7

Conclusion and Outlook

In this work, we have presented a DSMC method for simulating the dynamics of nondegenerate ultracold gases. A motivation for our work was to describe experiments in which two clouds were collided at high relative velocity. In order to simulate this highly nonequilibrium regime, we have adopted several modern enhancements of the DSMC algorithm (i.e., locally adaptive time steps and nearest-neighbor collisions) introduced in other fields but not previously used for cold-atom simulation. We have verified that our algorithm is accurate by comparison to a range of analytic results and simplified models. We have also provided some benchmarks of the performance of our algorithm against traditional DSMC to quantify the computational efficiency.

In order to quantitatively describe the collision experiments, we have included the full energy dependence of the s- and d-wave scatterings in the differential cross section. We have presented examples of the scattered distributions for the regime of experiments revealing the d-wave shape resonance. We have also considered the long-time dynamics of the colliding clouds, allowing them to recollide many times in the trap, observing how they approach equilibrium. Our work suggests that this might be a fruitful system for future experimental studies to test the accuracy of the Boltzmann equation and to better understand thermalization. We also find a discrepancy between the experimental measurements of Thomas *et al.* [32], and the two-body calculations of that work and Eite Tiesinga Sec. 5.1, in particular, the phase shifts best fit the experimental data at lower collision energies, which are $\approx 40\ \mu$K lower. Our results suggest that this shift occurs mainly in the d-wave phase shift and that the s-wave collision energy dependence is accurate.

A future application of this work will be to produce a complete dynamical finite temperature theory. Using a simple DSMC algorithm, Jackson and co-workers [16, 17, 18, 19, 20] have already implemented the ZNG formalism [21]. In the future, our DSMC approach

could be used to allow a similar extension to c-field formalism [82]. Having efficient procedures for evolving the c-field equations that describe the low-energy condensed or partially condensed part of the system [83, 84], the algorithm described in this thesis provides the basis for an efficient scheme for simulating the high-energy incoherent modes. In connection with this, we have identified crucial problems in simulating the quantum BE with DSMC techniques. Thus, with our solid understanding of the classical DSMC method, we have suggested several avenues of investigation to remedy these issues.

Also, this work provides a theoretical basis for the next generation high-precision optical collider currently in development by the Kjærgaard group at the University of Otago. The work in this thesis has demonstrated the necessary many-body simulation techniques to link the experimental observations to the two-body theory. This may lead to a better understanding of ultracold interactions, and complement the currently used techniques, such as, Feshbach and photoassociation spectroscopy.

References

[1] I. Shvarchuck, Ch. Buggle, D. S. Petrov, M. Kemmann, W. von Klitzing, G. V. Shlyap-nikov, and J. T. M. Walraven, *Hydrodynamic behavior in expanding thermal clouds of* ^{87}Rb, Phys. Rev. A **68**, 063603 (2003)

[2] J. Kinast, S. L. Hemmer, M. E. Gehm, A. Turlapov, and J. E. Thomas, *Evidence for Superfluidity in a Resonantly Interacting Fermi Gas*, Phys. Rev. Lett. **92**, 150402 (2004)

[3] D. S. Jin, J. R. Ensher, M. R. Matthews, C. E. Wieman, and E. A. Cornell, *Collective Excitations of a Bose-Einstein Condensate in a Dilute Gas*, Phys. Rev. Lett. **77**, 420 (1996)

[4] D. M. Stamper-Kurn, H.-J. Miesner, S. Inouye, M. R. Andrews, and W. Ketterle, *Collisionless and Hydrodynamic Excitations of a Bose-Einstein Condensate*, Phys. Rev. Lett. **81**, 500 (1998)

[5] H. J. Lewandowski, D. M. Harber, D. L. Whitaker, and E. A. Cornell, *Observation of Anomalous Spin-State Segregation in a Trapped Ultracold Vapor*, Phys. Rev. Lett. **88**, 070403 (2002)

[6] J. M. McGuirk, H. J. Lewandowski, D. M. Harber, T. Nikuni, J. E. Williams, and E. A. Cornell, *Spatial Resolution of Spin Waves in an Ultracold Gas*, Phys. Rev. Lett. **89**, 090402 (2002)

[7] F. Gerbier, J. H. Thywissen, S. Richard, M. Hugbart, P. Bouyer, and A. Aspect, *Critical Temperature of a Trapped, Weakly Interacting Bose Gas*, Phys. Rev. Lett. **92**, 030405 (2004)

[8] K.-K. Ni, S. Ospelkaus, D. Wang, G. Quéméner, B. Neyenhuis, M. H. G. de Miranda, J. L. Bohn, J. Ye, and D. S. Jin, *Dipolar collisions of polar molecules in the quantum regime*, Nature **464**, 1324 (2010)

References

[9] T. Nikuni, J. E. Williams, and C. W. Clark, *Linear spin waves in a trapped Bose gas*, Phys. Rev. A **66**, 043411 (2002)

[10] U. Al Khawaja, C. J. Pethick, and H. Smith, *Kinetic Theory of Collective Modes in Atomic Clouds Above the Bose-Einstein Transition Temperature*, J. Low Temp. Phys. **118**, 127 (2000)

[11] P. Pedri, D. Guéry-Odelin, and S. Stringari, *Dynamics of a classical gas including dissipative and mean-field effects*, Phys. Rev. A **68**, 043608 (2003)

[12] D. Guéry-Odelin, F. Zambelli, J. Dalibard, and S. Stringari, *Collective oscillations of a classical gas confined in harmonic traps*, Phys. Rev. A **60**, 4851 (1999)

[13] H. Wu and C. J. Foot, *Direct simulation of evaporative cooling*, J. Phys. B **29**, L321 (1996)

[14] H. Wu, E. Arimondo, and C. J. Foot, *Dynamics of evaporative cooling for Bose-Einstein condensation*, Phys. Rev. A **56**, 560 (1997)

[15] H. Wu and E. Arimondo, *Expansion of the non-condensed trapped Bose gas in Bose-Einstein condensation*, Europhys. Lett. **43**, 141 (1998)

[16] B. Jackson and C. S. Adams, *Damping and revivals of collective oscillations in a finite-temperature model of trapped Bose-Einstein condensation*, Phys. Rev. A **63**, 053606 (2001)

[17] B. Jackson and E. Zaremba, *Finite-Temperature Simulations of the Scissors Mode in Bose-Einstein Condensed Gases*, Phys. Rev. Lett. **87**, 100404 (2001)

[18] B. Jackson and E. Zaremba, *Modeling Bose-Einstein condensed gases at finite temperatures with N-body simulations*, Phys. Rev. A **66**, 033606 (2002)

[19] B. Jackson and E. Zaremba, *Quadrupole Collective Modes in Trapped Finite-Temperature Bose-Einstein Condensates*, Phys. Rev. Lett. **88**, 180402 (2002)

[20] B. Jackson and E. Zaremba, *Dynamical Simulations of Trapped Bose Gases at Finite Temperatures*, Laser Phys. **12**, 93 (2002)

[21] E. Zaremba, T. Nikuni, and A. Griffin, *Dynamics of Trapped Bose Gases at Finite Temperatures*, J. Low Temp. Phys. **116**, 277 (1999)

[22] M. Urban and P. Schuck, *Dynamics of a trapped Fermi gas in the BCS phase*, Phys. Rev. A **73**, 013621 (2006)

[23] M. Urban, *Coupling of hydrodynamics and quasiparticle motion in collective modes of superfluid trapped Fermi gases*, Phys. Rev. A **75**, 053607 (2007)

[24] M. Urban, *Radial quadrupole and scissors modes in trapped Fermi gases across the BCS phase transition*, Phys. Rev. A **78**, 053619 (2008)

[25] T. Lepers, D. Davesne, S. Chiacchiera, and M. Urban, *Numerical solution of the Boltzmann equation for the collective modes of trapped Fermi gases*, Phys. Rev. A **82**, 023609 (2010)

[26] P. Vignolo, M. L. Chiofalo, S. Succi, and M. Tosi, *Explicit Finite-Difference and Particle Method for the Dynamics of Mixed Bose-Condensate and Cold-Atom Clouds*, J. Comp. Phys. **182**, 368 (2002)

[27] F. Toschi, P. Vignolo, S. Succi, and M. P. Tosi, *Dynamics of trapped two-component Fermi gas: Temperature dependence of the transition from collisionless to collisional regime*, Phys. Rev. A **67**, 041605(R) (2003)

[28] P. Capuzzi, P. Vignolo, F. Toschi, S. Succi, and M. P. Tosi, *Effects of collisions against thermal impurities in the dynamics of a trapped fermion gas*, Phys. Rev. A **70**, 043623 (2004)

[29] F. Toschi, P. Capuzzi, S. Succi, P. Vignolo, and M. P. Tosi, *Transition to hydrodynamics in colliding fermion clouds*, J. Phys. B **37**, S91 (2004)

[30] P. Barletta, J. Tennyson, and P. F. Barker, *Direct Monte Carlo simulation of the sympathetic cooling of trapped molecules by ultracold argon atoms*, New J. Phys **12**, 113002 (2010)

[31] P. Barletta, *COOL: A code for dynamic Monte Carlo simulation of molecular dynamics*, Comp. Phys. Comm. **182**, 388 (2011)

[32] N. R. Thomas, N. Kjærgaard, P. S. Julienne, and A. C. Wilson, *Imaging of* s *and* d *Partial-Wave Interference in Quantum Scattering of Identical Bosonic Atoms*, Phys. Rev. Lett. **93**, 173201 (2004)

[33] N. Kjærgaard, A. S. Mellish, and A. C. Wilson, *Differential scattering measurements from a collider for ultracold atoms*, New J. Phys **6**, 146 (2004)

References

[34] A. S. Mellish, N. Kjærgaard, P. S. Julienne, and A. C. Wilson, *Quantum scattering of distinguishable bosons using an ultracold-atom collider*, Phys. Rev. A **75**, 020701(R) (2007)

[35] G. A. Bird, *Molecular Gas Dynamics and the Direct Simulation of Gas Flows*, 2nd ed. (Clarendon Press, Oxford, 1994)

[36] A. C. J. Wade, D. Baillie, and P. B. Blakie, *Direct simulation Monte Carlo method for cold-atom dynamics: Classical Boltzmann equation in the quantum collision regime*, Phys. Rev. A **84**, 023612 (2011)

[37] K. Huang, *Statistical Mechanics*, 2nd ed. (John Wiley & Sons, 1987)

[38] M. Kardar, *Statistical Physics of Particles*, 1st ed. (Cambridge University Press, 2007)

[39] C. J. Pethick and H. Smith, *Bose-Einstein Condensation in Dilute Gases*, 1st ed. (Cambridge University Press, 2001)

[40] B. DeMarco and D. S. Jin, *Onset of Fermi Degeneracy in a Trapped Atomic Gas*, Science **285**, 1703 (1999)

[41] A. G. Truscott, K. E. Strecker, W. I. McAlexander, G. B. Partridge, and R. G. Hulet, *Observation of Fermi Pressure in a Gas of Trapped Atoms*, Science **291**, 2570 (2001)

[42] F. Dalfovo, S. Giorgini, L. P. Pitaevskii, and S. Stringari, *Theory of Bose-Einstein condensation in trapped gases*, Rev. Mod. Phys. **71**, 463 (1999)

[43] T. Watanabe, H. Kaburaki, and M. Yokokawa, *Simulation of a two-dimensional Rayleigh-Bénard system using the direct simulation Monte Carlo method*, Phys. Rev. E **49**, 4060 (1994)

[44] E. S. Oran, C. K. Oh, and B. Z. Cybyk, *Direct simulation Monte Carlo: Recent Advances and Applications*, Annu. Rev. Fluid Mech. **30**, 403 (1998)

[45] J. B. Anderson and L. N. Long, *Direct Monte Carlo simulation of chemical reaction systems: Prediction of ultrafast detonations*, J. Chem. Phys. **118**, 3102 (2003)

[46] *Advances In Multiphysics Simulation And Experimental Testing Of MEMS*, 1st ed., edited by A. Frangi, C. Cercignani, S. Mukherjee, and N. Aluru (Imperial College Press, 2008)

[47] A. D. Hanford and L. N. Long, *The direct simulation of acoustics on Earth, Mars, and Titan*, J. Acoust. Soc. Am. **125**, 640 (2009)

[48] J. Zhang, D. B. Goldstein, P. L. Varghese, L. Trafton, C. Moore, and K. Miki, *Numerical modeling of ionian volcanic plumes with entrained particulates*, Icarus **172**, 479 (2004)

[49] G. A. Bird, "Sophisticated DSMC," (2007), Notes from DSMC07 meeting, Santa Fe. Available at www.gab.com.au/DSMC07notes.pdf

[50] F. J. Alexander, A. L. Garcia, and B. J. Alder, *A Consistent Boltzmann Algorithm*, Phys. Rev. Lett. **74**, 5212 (1995)

[51] G. Kortemeyer, F. Daffin, and W. Bauer, *Nuclear flow in consistent Boltzmann algorithm models*, Phys. Lett. B **374**, 25 (1996)

[52] K. Morawetz, V. Špička, P. Lipavský, G. Kortemeyer, C. Kuhrts, and R. Nebauer, *Virial Corrections to Simulations of Heavy Ion Reactions*, Phys. Rev. Lett. **82**, 3767 (1999)

[53] G. F. Bertsch and S. Das Gupta, *A Guide to Microscopic Models for Intermediate Energy Heavy Ion Collisions*, Phys. Rep. **160**, 189 (1988)

[54] A. Bonasera, F. Gulminelli, and J. Molitoris, *The Boltzmann-Equation at the Borderline - A Decade of Monte-Carlo Simulations of a Quantum Kinetic-Equation*, Phys. Rep. **243**, 1 (1994)

[55] A. Lang, H. Babovsky, W. Cassing, U. Mosel, H. G. Reusch, and K. Weber, *A New Treatment of Boltzmann-like Collision Integrals in Nuclear Kinetic Equations*, J. Comp. Phys. **106**, 391 (1993)

[56] W. Wagner, *A Convergence Proof for Bird's Direct Simulation Monte Carlo Method for the Boltzmann Equation*, J. Stat. Phys. **66**, 1011 (1992)

[57] E. Meiburg, *Comparison of the molecular dynamics method and the direct simulation Monte Carlo technique for flows around simple geometries*, Phys. Fluids **29**, 3107 (1986)

[58] M. A. Gallis, J. R. Torczynski, D. J. Rader, and G. A. Bird, *Convergence behavior of a new DSMC algorithm*, J. Comput. Phys. **228**, 4532 (2009)

[59] H. Yoshida, *Recent Progress in the Theory and Application of Symplectic Integrators*, Celest. Mech. Dyn. Astron. **56**, 27 (1993)

References

[60] D. Guéry-Odelin, J. Söding, P. Desbiolles, and J. Dalibard, *Strong evaporative cooling of a trapped cesium gas*, Opt. Express **2**, 323 (1998)

[61] A. L. Garcia, *Estimating hydrodynamic quantities in the presence of fluctuations*, Comm. App. Math. and Comp. Sci. **1**, 53 (2006)

[62] N. G. Hadjiconstantinou, A. L. Garcia, M. Z. Bazant, and G. He, *Statistical error in particle simulations of hydrodynamic phenomena*, J. Comp. Phys. **187**, 274 (2003)

[63] T. Esslinger, I. Bloch, and T. W. Hänsch, *Bose-Einstein condensation in a quadrupole-Ioffe-configuration trap*, Phys. Rev. A **58**, R2664 (1998)

[64] N. R. Thomas, A. C. Wilson, and C. J. Foot, *Double-well magnetic trap for Bose-Einstein condensates*, Phys. Rev. A **65**, 063406 (2002)

[65] N. R. Thomas, *The Double-TOP trap for ultracold atoms*, Ph.D. thesis, University of Otago, NZ (2004)

[66] A. L. Garcia, "Short course on direct simulation Monte Carlo," (2009), talk given at the DSMC09 meeting, Santa Fe. Available at http://www.algarcia.org/Talks/DSMC_ShortCourse.ppt

[67] Y. B. Band, M. Trippenbach, J. P. Burke, Jr., and P. S. Julienne, *Elastic Scattering Loss of Atoms from Colliding Bose-Einstein Condensate Wave Packets*, Phys. Rev. Lett. **84**, 5462 (2000)

[68] A. P. Chikkatur, A. Görlitz, D. M. Stamper-Kurn, S. Inouye, S. Gupta, and W. Ketterle, *Suppression and Enhancement of Impurity Scattering in a Bose-Einstein Condensate*, Phys. Rev. Lett. **85**, 483 (2000)

[69] P. B. Blakie, E. Toth, and M. J. Davis, *Calorimetry of Bose-Einstein condensates*, J. Phys. B **40**, 3273 (2007)

[70] M. Rigol, V. Dunjko, and M. Olshanii, *Thermalization and its mechanism for generic isolated quantum systems*, Nature **452**, 854 (2008)

[71] M. Rigol, *Breakdown of Thermalization in Finite One-Dimensional Systems*, Phys. Rev. Lett. **103**, 100403 (2009)

[72] A. C. Cassidy, C. W. Clark, and M. Rigol, *Generalized Thermalization in an Integrable Lattice System*, Phys. Rev. Lett. **106**, 140405 (2011)

[73] T. Kinoshita, T. Wenger, and D. S. Weiss, *A quantum Newton's cradle*, Nature **440**, 900 (2006)

[74] M. Anderlini and D. Guéry-Odelin, *Thermalization in mixtures of ultracold gases*, Phys. Rev. A **73** (2006)

[75] Ch. Buggle, J. Léonard, W. von Klitzing, and J. T. M. Walraven, *Interferometric Determination of the* s *and* d*-Wave Scattering Amplitudes in* ^{87}Rb, Phys. Rev. Lett. **93**, 173202 (2004)

[76] A. Marte, T. Volz, J. Schuster, S. Dürr, G. Rempe, E. G. M. van Kempen, and B. J. Verhaar, *Feshbach Resonances in Rubidium 87: Precision Measurement and Analysis*, Phys. Rev. Lett. **89**, 283202 (2002)

[77] C. Strauss, T. Takekoshi, F. Lang, K. Winkler, R. Grimm, J. Hecker Denschlag, and E. Tiemann, *Hyperfine, rotational, and vibrational structure of the* $a^3\Sigma_u^+$ *state of* $^{87}Rb_2$, Phys. Rev. A **82**, 052514 (2010)

[78] R. W. Hockney and J. Eastwood, *Computer Simulation Using Particles* (Taylor & Francis Group, 1988)

[79] W. H. Press, S. A. Teukolsky, W. T. Vetterling, and B. P. Flannery, *Numerical Recipes in C: The Art of Scientific Computing*, 2nd ed. (Cambridge University Press, 1992)

[80] T. Lopez-Arias and A. Smerzi, *Kinetic properties of a Bose-Einstein gas at finite temperature*, Phys. Rev. A **58**, 526 (1998)

[81] A. L. Garcia and W. Wagner, *Direct simulation Monte Carlo method for the Uehling-Uhlenbeck-Boltzmann equation*, Phys. Rev. E **68**, 056703 (2003)

[82] P. B. Blakie, A. S. Bradley, M. J. Davis, R. J. Ballagh, and C. W. Gardiner, *Dynamics and statistical mechanics of ultra-cold Bose gases using c-field techniques*, Adv. Phys. **57**, 363 (2008)

[83] P. B. Blakie and M. J. Davis, *Projected Gross-Pitaevskii equation for harmonically confined Bose gases at finite temperature*, Phys. Rev. A **72**, 063608 (2005)

[84] P. B. Blakie, *Numerical method for evolving the projected Gross-Pitaevskii equation*, Phys. Rev. E **78**, 026704 (2008)